SINGLE-SHOT CHARACTERIZATION OF ULTRAFAST ELECTRON DYNAMICS USING PHOTOELECTRON SPECTROSCOPY

By

SARA SAVIO
BORN IN KARKALA

Dissertation for the Degree of Doctor of Natural Science- Dr. rer. nat.-

Fakultät Physik
Technische Universität Dortmund

March 2026

Promotionsausschuss:

Vorsitzender:	Prof. Dr. Dr. Wolfgang Rhode
Erstgutachter:	Jun.-Prof. Dr. Wolfram Helml
Zweitgutachter:	Prof. Dr. Markus Ilchen

Tag der wissenschaftlichen Aussprache: 26. March 2026

ABSTRACT

Core-level photoionization is a fundamental process in light–matter interaction consisting of absorbing a photon by an atom or molecule, ejecting an electron from one of its inner shells, and creating a core-shell vacancy. This vacancy is then filled through various relaxation processes, which can result in the emission of secondary electrons or energy redistribution within the system. The results presented in this thesis contain technical and methodological advances in characterizing the decay dynamics of double-core holes (DCH) in gaseous neon atoms, which have a very short lifetime, using intense and ultrashort X-ray pulses on the attosecond (10^{-18} s) scale at the European XFEL (Eu-XFEL).

Ultrafast electron dynamics are mapped on a single-shot basis using an angle-resolving electron time-of-flight (e-TOF) spectrometer. A spectrometer was built and commissioned as part of this work and is presented in detail, including technical information and experimentally retrieved performance data. Non-invasive systematic pulse characterization using the angular streaking technique provides spectral and temporal information about the ionizing XFEL pulses with attosecond resolution. This approach enables single-shot DCH probing based on the knowledge of spectro-temporal details about the ionizing pulses.

A comprehensive study was conducted to investigate how the contribution of DCH channels varies with X-ray pulse parameters, including pulse duration, pulse energy, and the photon energy centres of the reconstructed spectra. The results show that the yield of the DCH signal increases in such a way that is compatible with the reconstruction of X-ray pulse durations well below the life time of the single-core hole (SCH) Auger decay in neon, which is on the order of 2.4 femtosecond (10^{-15} s), thus enabling the characterization of such short-lived ionic states in a single shot. Examining the electronic structure of the core-ionized system before relaxation, combined with detailed information about the ionizing pulse, provides the experimental stage for valuable insights into nonlinear X-ray–matter interaction. Thus the ensuing photoabsorption and relaxation channel intensities achievable at high-repetition-rate, attosecond duration XFEL allow to reveal these ultrafast processes on the natural timescale of electron dynamics.

KURZFASSUNG

Die Kern-Photoionisation ist ein grundlegender Prozess in der Licht-Materie-Wechselwirkung, bei dem ein Atom oder Molekül ein Photon absorbiert, ein Elektron aus einer seiner inneren Schalen ausstößt und eine Kern-Schalen-Lücke erzeugt. Diese Lücke wird dann durch verschiedene Relaxationsprozesse gefüllt, was zur Emission von Sekundärelektronen oder zur Energieumverteilung innerhalb des Systems führen kann. Die in dieser Arbeit vorgestellten Ergebnisse enthalten technische und methodische Fortschritte bei der Charakterisierung der Zerfallsdynamik von Doppelkernlöchern (DCH) in gasförmigen Neonatomen, die eine sehr kurze Lebensdauer haben, unter Verwendung intensiver und ultrakurzer Röntgenimpulse im Attosekundenbereich (10^{-18} s) am European XFEL (Eu-XFEL).

Die ultraschnelle Elektronendynamik wird auf Single-Shot-Basis mit einem winkelauflösenden Elektronen-Flugzeit-Spektrometer (e-TOF) abgebildet. Im Rahmen dieser Arbeit wurde ein Spektrometer gebaut und in Betrieb genommen, das hier detailliert vorgestellt wird, einschließlich technischer Informationen und experimentell ermittelter Leistungsdaten. Die nicht-invasive systematische Impulscharakterisierung unter Verwendung der Winkelstrecktechnik liefert spektrale und zeitliche Informationen über die ionisierenden XFEL-Impulse mit Attosekundenauflösung. Dieser Ansatz ermöglicht eine Single-Shot-DCH-Untersuchung auf der Grundlage der Kenntnis spektral-zeitlicher Details über die ionisierenden Impulse.

Es wurde eine umfassende Studie durchgeführt, um zu untersuchen, wie sich der Beitrag der DCH-Kanäle mit den Parametern der Röntgenimpulse, einschließlich Impulsdauer, Impulsenergie und den Photonenenergiezentren der rekonstruierten Spektren, verändert. Die Ergebnisse zeigen, dass die Ausbeute des DCH-Signals in einer Weise zunimmt, die mit der Rekonstruktion von Röntgenimpulsdauern weit unterhalb der Lebensdauer des Single-Core-Hole (SCH)-Auger-Zerfalls in Neon vereinbar ist, die in der Größenordnung von 2,4 Femtosekunden (10^{-15} s) liegt, wodurch die Charakterisierung solcher kurzlebigen Ionenzustände in einem einzigen Schuss ermöglicht wird. Die Untersuchung der elektronischen Struktur des kernionisierten Systems vor der Relaxation in Verbindung mit detaillierten Informationen über den ionisierenden Impuls bietet die experimentelle Grundlage für wertvolle Einblicke in die nichtlineare Wechselwirkung zwischen Röntgenstrahlung und Materie. Somit ermöglichen die sich daraus ergebenden Photoabsorptions- und Relaxationskanalintensitäten, die bei einer hohen Wiederholungsrate und einer Attosekunden-Dauer des XFEL erreichbar sind, die Aufdeckung dieser ultraschnellen Prozesse auf der natürlichen Zeitskala der Elektronendynamik.

Contents

List of Figures

List of Tables

Chapter 1

Introduction

On May 16, 1960, Theodore H. Maiman demonstrated the first working model of a laser [1], a significant achievement at the time and a new hope for accessing the non-linear regime, which had not been explored before. The later developments that happened in the field of optical lasers advanced the exploration of ultrafast processes that occur on the molecular scale. This exploration of events on the atomic and molecular scale opened a new field of physics, known as attosecond science. The primary objective of this field is to explore and probe the attosecond (1 as = 10^{-18} s) regime processes like the electron dynamics inside an atom with a high order of temporal resolution. This allows a fundamental understanding of the chemical reactivity, charge migration, and photoionization processes [2].

When matter is exposed to sufficiently intense light fields, its response becomes nonlinear, resulting in phenomena such as multiphoton absorption, above-threshold ionization, and high-harmonic generation [3]. These nonlinear processes are not only fundamental to understanding light –matter interactions but also serve as diagnostic tools to characterize ultrafast events. Crucially, they highlight the capability of mapping out correlated electron motion in real time by providing access to states and events that are otherwise unavailable in the linear regime.

The advent of short-wavelength (X-ray) sources with attosecond to few-femtosecond pulse durations has enabled the extension of attosecond science into the X-ray domain. This advancement is particularly significant for probing core-level electronic states, which are tightly bound and highly localized around specific atomic sites. Such core-level excitations provide element and site-specific information, making them ideal for studying charge transfer and relaxation dynamics in complex systems, such as molecules, clusters, and solids [4]. Moreover, the high photon energy associated with these X-rays allows access to the more localized and

firmly bound core electrons, which in turn are capable of providing information about their chemical environment. Monitoring their evolution in time after photoexcitation or ionization allows one to disentangle site-specific charge migration pathways and identify intermediate states that mediate ultrafast chemical reactions. These studies are central to developing a clear understanding of processes such as inner-shell ionization, Auger decay etc. [5, 6].

The realization of such studies has been greatly accelerated by the development of X-ray free-electron lasers (XFELs), which deliver ultrashort (few-fs to sub-fs), high-intensity X-ray pulses with high spatial coherence and brilliance. XFELs such as the Linac Coherent Light Source (LCLS) [7], Free Electron Laser in Hamburg (FLASH) [8], and the European XFEL (Eu-XFEL) [9] have revolutionized time-resolved spectroscopy and diffraction techniques, allowing researchers to track atomic-scale structural and electronic changes in real time [10, 11]. In an XFEL, electron bunches are first accelerated to high energies using a linear accelerator, and then passed through undulator segments, where they produce coherent X-ray bursts through the process of self-amplified spontaneous emission (SASE) [12]. The resulting pulses exhibit peak intensities sufficient to drive nonlinear processes even in the X-ray regime [13].

Despite their tremendous potential, the scientific output of XFELs depends on the accurate spectral and temporal characterization of the emitted X-rays. This is essential for interpreting ultrafast pump-probe experiments, especially when the system under study evolves on a faster timescale. One of the most effective techniques for pulse duration measurement is attosecond streaking [14], wherein an ultrashort X-ray pulse ionizes a target atom, and a synchronized near-infrared laser field streaks the ejected photoelectrons. The resulting energy shifts in the photoelectron spectrum encode the temporal structure of the X-ray pulse, allowing for the reconstruction of its temporal and spectral information with attosecond resolution [15, 16].

This characterization of the individual incoming XFEL pulse is very advantageous to sort relevant incoming pulses, which are capable of starting a nonlinear phenomenon. One such process that is initiated by an intense X-ray pulse is the double-core-hole (DCH) Auger decay [17]. The characterization of these ultrafast nonlinear processes on a single-shot basis is very significant. Incorporating temporal and spectral information, along with high peak brilliance at XFELs, opens up a new world of electron dynamics characterization in a single shot.

This work provides insights into the characterization of transient and short-lived states that are generated using the intense X-ray pulses from Eu-XFEL. The capability of photoelectron spectroscopy using an angle-resolved time-of-flight (TOF) spectrometer is used for single-shot characterization. Beyond the pulse characterization, this experimental setup, using the X-ray pulse with the TOF spectrometer, is capable of characterizing the short-lived ionic states

in single-shot spectra. This enables the opportunity of probing events on the sub-femtosecond scale with a non-invasive diagnostic of the ionizing beam. Illustration of a sequential multi-photon ionization process, which has a lifetime of less than a few femtoseconds in a single shot, is only possible with a high-intensity X-ray pulse, which Eu-XFEL is capable of delivering.

Complementing the pulse duration analysis with a physical phenomenon dependent on the intensity of the ionizing pulse, along with the spectral comparison of the reconstructed incoming X-rays to an independent spectral characterization, is crucial while checking the robustness of the reconstruction mechanism.

In the upcoming chapters, the aforementioned non-linear characterization of the short-lived state, along with the pulse characterization, is explained. Chapter 2 gives an idea about the basics of light –matter interaction and the light source that is used for the investigations of the significant part of this work. Chapter 3 provides in-depth information about the angle-resolving TOF spectrometer setup. One of the significant parts of this work was to build and commission a TOF spectrometer setup that can be installed at the Eu-XFEL for pulse characterization. This chapter provides details about the mechanical designs and design adaptations incorporated into the detector electronics. Chapter 4 presents a series of experiments conducted during the initial stages of the research. Chapter 5 gives insights into the DCH characterization in neon using the intense X-ray pulses in a single shot. The pulse duration dependence on the DCH yield, along with a spectral comparison of the incoming pulse using the two individual schemes, is also provided here. The scientific results obtained from this work are concluded in Chapter 6, along with possible future possibilities.

Chapter 2

Theoretical Background

2.1 Atomic Systems

This chapter provides a foundational overview of atomic orbitals, light–matter interactions, and the properties of light source relevant to this study. The research presented herein centers on experimental investigations conducted at an XFEL facility, with particular emphasis on spectroscopic techniques for probing ultrafast phenomena. To ensure a comprehensive understanding of the results and analysis presented in later chapters, this section outlines the necessary theoretical background, introduces the term photoionization and related mechanisms along with the light source employed for this work. Therefore, the theoretical depth of description is limited to those concepts essential for understanding the main mechanisms of atomic-level photoionization and the subsequent electronic relaxation processes, which form the core focus of this thesis.

2.1.1 Atomic orbitals and energy levels

Matter consists of atoms, each comprising a central nucleus surrounded by electrons. The electromagnetic force between the negatively charged electrons and the positively charged nucleus keeps the electrons bound to the atom. The nucleus, which contains nearly all of the atom's mass, consists of positively charged protons and electrically neutral neutrons. Electrons are not free to occupy arbitrary positions around the nucleus; instead, they are described by atomic orbitals, which correspond to probability distributions that determine the likelihood of detecting an electron [18]. This concept was first formalized by the Danish physicist Niels Bohr in 1913, leading to the development of the Bohr model of the atom.

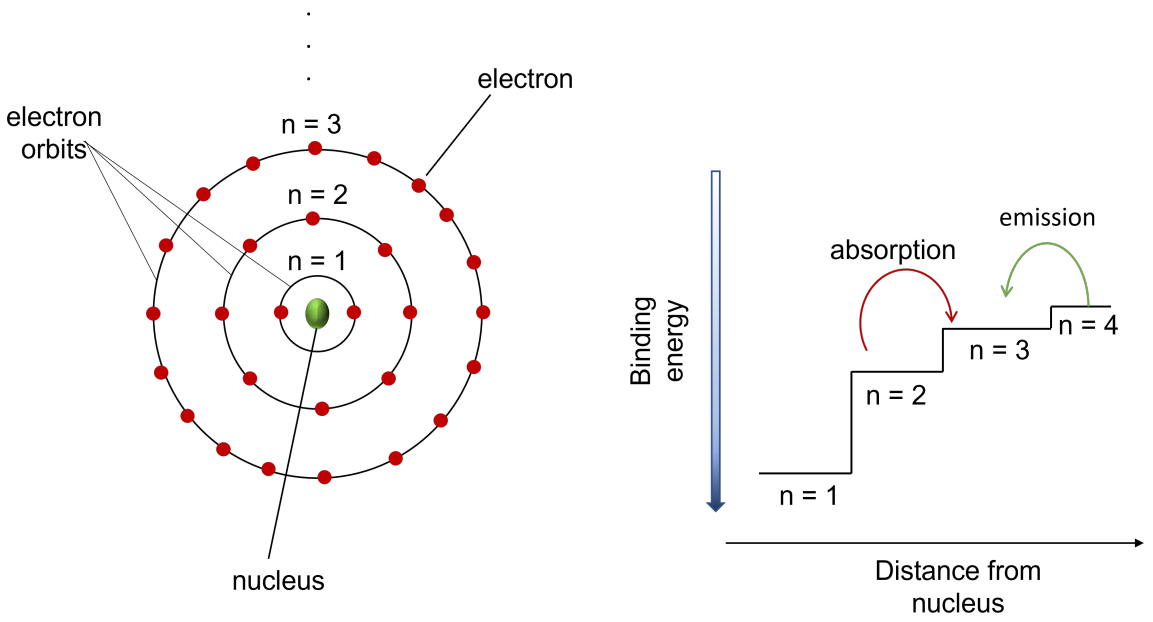

Figure 2.1: Bohr model of atom with energy levels marked from n = 1 to n = 3. The transition of an electron from the n = 2 orbital to the n = 3 orbital shows energy absorption (red arrow), corresponding to the energy gap. Absorption can promote an electron from orbitals near the nucleus to those farther from the nucleus. A transition from a higher energy level (n) to a lower one signifies energy emission (represented with a green arrow). The binding energy axis with a gradient color scale indicates high binding energy for the shells with a lower value of n.

In the Bohr model of the atom, electrons occupy discrete, quantized orbits, each with a specific energy and radius, as illustrated in 2.1. The energy associated with these orbitals increases with the distance from the nucleus. When an electron moves from one orbital to another, it undergoes a discrete change in energy known as a quantum jump, without existing in the intermediate space between the two states [18].

The energy of the electron after such a transition differs from its initial energy, reflecting the energy difference between the two orbitals. When an electron transitions from a higher to a lower energy level (as indicated by the green arrow in 2.1), the excess energy can be released as electromagnetic radiation (radiative decay) or transferred to another electron within the system via non-radiative decay pathways. Conversely, suppose energy is absorbed by the atom that matches the energy gap between the two levels. In that case, an electron can be excited from a lower to a higher energy orbital (as indicated by the red arrow in 2.1).

Each chemical element has a unique set of quantized energy levels, which determines the specific frequencies of light it can resonantly absorb or emit. These frequencies serve

as characteristic spectral fingerprints, enabling the identification and analysis of elements through spectroscopic techniques. This fundamental property underlies atomic spectroscopy, a field that studies the interaction between electromagnetic radiation and matter at the atomic level.

The discrete, fixed-electron-orbit model of the Bohr model inadequately accounts for atomic behavior, which is better explained by the wave-like nature of electrons introduced in quantum mechanics. Erwin Schrödinger developed the wave equation, which supersedes the discrete electron-orbital concept by describing the probability distribution of electron locations around the nucleus. The time-independent Schrödinger equation is crucial in atomic physics, as its solution yields quantized energy levels and wavefunctions that describe the spatial distribution of electrons, known as atomic orbitals. This can be represented as,

$$\hat{H}\Psi = E\Psi \tag{2.1}$$

where $\hat{H}$ is the Hamiltonian operator, E is the energy of the system, and Ψ is the wavefunction of the system that contains information about its physical state [19].

Atomic orbitals are defined by quantum numbers, which describe their size, shape, orientation, and electron energy levels. Each electron in an atom has a unique combination of these quantum numbers; based on Pauli's exclusion principle, no two electrons can have the same set of quantum numbers [20]. Quantum numbers are significant because they determine the electron configuration and probable location of an atom's electrons and help understand other characteristics, such as ionization energy and atomic radius. There are four sets of quantum numbers, namely the principal quantum number n, the angular momentum quantum number l, the magnetic quantum number m, and the electron spin quantum number m_s. The principal quantum number describes an electron's energy and the distance from the nucleus. All orbitals with the same principal quantum number value make up a shell. The angular momentum quantum number, l, describes the number of sub-shells and their shapes. The magnetic quantum number, m, defines the energy levels in a subshell. The spin quantum number characterizes the projection of the electron spin along a chosen axis.

The principal quantum number, denoted by n, identifies the primary electron shell in an atom. It indicates the most probable radius between an electron and the nucleus. As n increases, the electron resides farther from the nucleus, resulting in larger orbitals and an overall increase in atomic size. The value of n can be any positive integer starting from 1, which corresponds to the first and innermost electron shell, also referred to as core-shell. When an electron in the $n = 1$ shell absorbs energy, it can become excited and transition to any higher

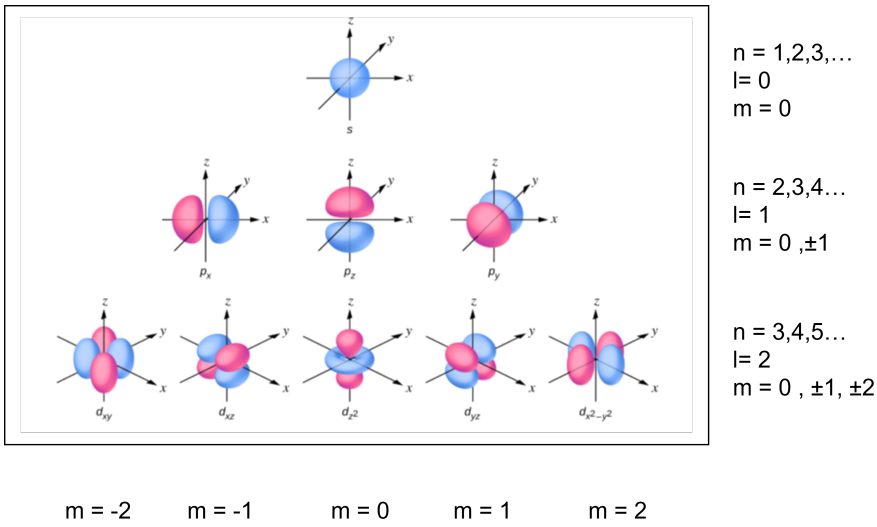

Figure 2.2: Visual representation of atomic orbital shapes for the s, p, d, and f subshells. Each orbital is labelled with its corresponding magnetic quantum number *m*, indicating the spatial orientation of the orbital within a given subshell. The s orbital with $l = 0$ has a single orientation $m = 0$, while the p $l = 1$ and d $l = 2$ orbitals exhibit different orientations. Image modified from [21].

shell, such as $n = 2,3$, etc. Electron shells are traditionally labeled with capital letters: K, L, M, N, and so on, corresponding to $n = 1, 2, 3, 4$, respectively.

The orbital angular momentum quantum number determines the shape of the orbitals in a shell and, therefore, the angular distribution of electrons. Each value of *l* corresponds to a specific orbital- s, p, d, f with a distinct shape. Unlike the principal quantum number, *l* can be zero or a positive integer but cannot exceed *n-1*. This limitation reflects the fact that for a given energy level *n*, there are only *n* possible orbital shapes (subshells), each corresponding to an allowed angular momentum state. The most common atomic orbitals, s, p, and d, are shown in 2.2. The s orbital has a spherical shape and is distributed around the nucleus. The p orbital has a dumbbell shape with three different orientations p_x, p_y, and p_z. The complexity of the orbital shape increases from d onward. The number of orbitals and the orientation inside a subshell are determined by the magnetic quantum number *m*. The values of *m* can range from *-l* to *+l*, meaning this can be a zero, negative, or positive integer. Unlike *n*, *l*, *m*, the electron spin quantum number does not depend on another quantum number. The spin quantum number describes the electron spin direction and can have a value of either $\pm 1/2$. A positive value corresponds to an upward direction, and a negative value represents a downward direction.

The filling of electrons inside atomic orbitals is primarily based on the Aufbau principle

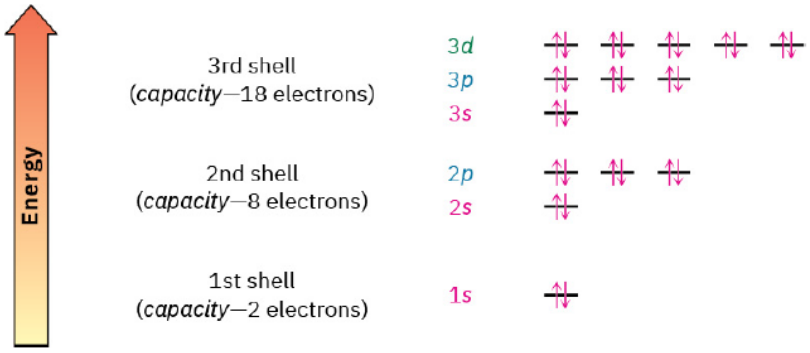

Figure 2.3: Shows the arrangement of electrons inside a shell. The first shell has 2 electrons in the 1s orbital; the second shell contains a maximum of 8 electrons, 2 in the s orbital and 6 in the p orbital, and so on, taken from [21].

[22], Hund's rule of maximum multiplicity [23], and Pauli's exclusion principle [20]. The ground state, or the state with the lowest energy, will be filled first before the higher-energy state. The electron fill pattern will be 1s, 2s, 2p, 3s, 3p, 4s, 3d, 4p, 5s, 4d, and so on, as shown in the direction of the arrow in Figure 2.3. The electron configuration of krypton with atomic number Z= 36, is $1s^2\ 2s^2\ 2p^6\ 3s^2\ 3p^6\ 4s^2\ 3d^{10}4p^6$ and instead of writing the full configuration one can also write this [Ar] $4s^2\ 3d^{10}4p^6$. This is the shorthand representation, where the valence shell is written together with the next smallest noble gas element, representing all the filled lower shells [21].

2.2 Light–Matter Interaction

2.2.1 Photoelectric effect

The discovery of the photoelectric effect played a crucial role in advancing quantum mechanics by demonstrating the particle nature of light, which was not explainable by classical mechanics. In 1905, Albert Einstein mathematically explained that electrons are ejected from the surface of metals when electromagnetic radiation with sufficient energy is incident on them [24]. This is possible only when the incident photon has a minimum energy greater than the electron's binding energy. This concept was closely linked to Max Planck's quantum hypothesis. It introduced the idea that light is composed of discrete energy packets, known as photons, rather than a continuous spectrum [25].

This PhD work primarily discusses photoelectron effects at fourth-generation light sources,

such as XFELs. These sources provide tunable radiation over a wide range of wavelengths, allowing access to variable energy levels (a more detailed discussion of the light sources is in Section 2.3). The interaction between photon and electron can be described in such a way that, when electromagnetic radiation with energy $E = h\nu$ incident on an atom, where h is Planck's constant and ν is the frequency, an electron is ejected from the atom if the incident photon energy is higher than the binding energy of the electron [24]. This can be represented as follows.

$$E_{KE} = h\nu - E_{Binding} \tag{2.2}$$

The kinetic energy of the ejected electron is represented as E_{KE} and the photon energy of incident light is hν. The binding energy ($E_{Binding}$) of electrons in a shell is available from literature [26]. This process, known as photoionization, provides experimental evidence that supports the theory and is also significant for understanding the behavior of electrons when interacting with radiation, which is essential for interpreting the observations discussed in this work.

2.2.2 Photoionization in atoms

The photon-electron interaction can initiate different processes depending on the photon energy of the exciting radiation and the sample with which it interacts. The fundamental photon-electron interaction, known as photoionization, is explained in the preceding section. The other exciting, spectroscopically measurable schemes of photoionization and subsequent radiative and non-radiative relaxation pathways are discussed in this section. Photoionization of valence shell electrons requires only a few tens of electron volts (eV) of photon energy. This is due to the comparatively greater distance between the nucleus and the outer electrons, as well as the screening effect of inner-shell electrons. In comparison, the inner-shell electrons require hundreds to thousands of eV [27] for ionization. The framework of this work is to spectroscopically map out inner-shell ionization and related ultrafast electron dynamics, which is enabled by a soft X-ray beam with a tunable photon energy available at Eu-XFEL [28].

Since we are dealing with a higher range of photon energies and the corresponding photoionization process, discussing the different types of photon-electron interaction will help elaborate on the importance and scope of this work. This section mainly compares three light-atom interactions: photoionization, the Auger decay (also sometimes referred as Auger–Meitner decay, acknowledging the significant contribution of Lise Meitner to its discovery

[29,30], however, for consistency with the terminology commonly used in the literature forming the basis of this thesis, the nomenclature 'Auger decay' is adopted throughout), and fluorescence.

Photoionization is a single-step process that involves only a single photon and an electron. This can happen to either the valence electron or the inner-shell electrons. The relation between the energy of the emitted electron, the photon energy, and the binding energy of the affected shell is the same as equation (2.1). The photoionization of outer shell electrons tells the valence shell's binding energy; similarly, the inner shell's photoionization gives the core-electron binding energies. The two different schemes are shown in Figure 2.4. The higher energy photon with energy $E = h\nu$ (blue-coloured incoming light) can eject electrons from the core-shell. In contrast, the comparatively lower energy $E = h\nu'$ can only ionize the electrons that are far away from the nucleus.

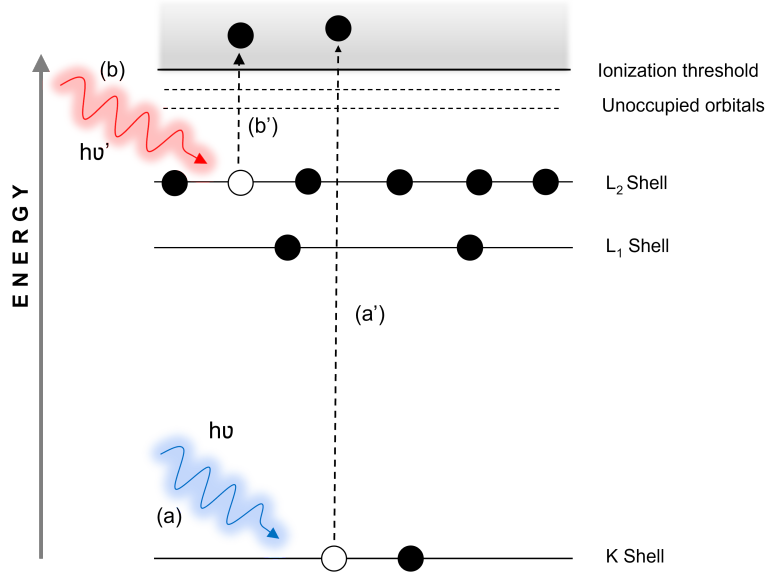

Figure 2.4: Schematic representation of photoionization. (a) and (a') are the absorption and corresponding inner-shell electron ionization with photon energy $h\nu$, whereas (b) and (b') represent the valence electron photoionization with $h\nu'$, where $h\nu > h\nu'$.

Fluorescence and the Auger process are essentially two-step processes, where the first step is the ejection of an electron by a photon, which is the photoionization mentioned earlier, and the second step is the filling of this hole either radiatively or non-radiatively. The radiative decay of an inner-shell vacancy by emitting a photon is called **fluorescence**. The first photon marked (1) in Figure 2.5. will create a hole in the core-shell (2), by emitting an electron, and one of the valence electrons fills this hole, marked as a transition (3), and the excess energy is

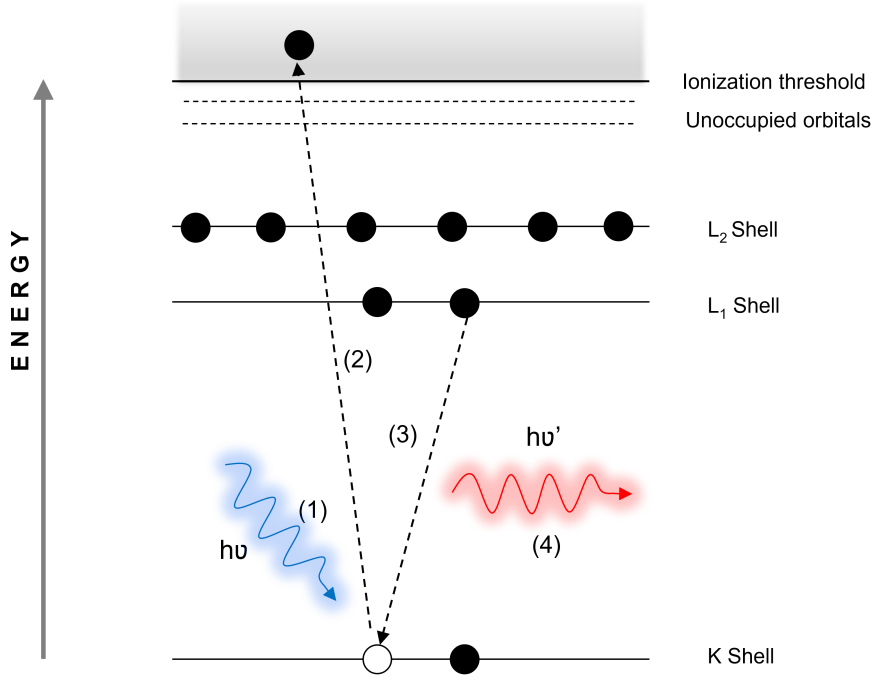

Figure 2.5: Schematic representation of the radiative decay (fluorescence) following core-shell photoionization.

emitted as a photon (4). The frequency or the energy of the emitted photon will be less than that of the incident one.

The nonradiative readjustment of the inner-shell vacancy occurs when an electron from a less tightly bound shell replaces the vacancy formed by photoionization, accompanied by the ejection of a second electron into the continuum, representing the **Auger decay** process [30]. Figure 2.6 shows an example of this Auger relaxation. The incident photon with energy to overcome the binding energy can generate a vacancy in the K shell (marked (1) and (2)). This hole is filled by the transition of an electron from the L shell (marked (3)) along with the release of an electron (process 4 in the example). The ejected electron from an L shell is called the Auger electron, and the kinetic energy of the electron will be,

$$E_A = E_K - E_L - E_L^{'} \tag{2.3}$$

E_A and E_L are the binding energies of the K and L shells of the neutral atom $E_L^{'}$ is the binding energy of an electron in the L shell with a vacancy in the L shell . The process explained here is called KLL Auger, named after the shells involved. The K shell electron undergoes photoionization, thus creating a core-shell vacancy, and the L shell electron fills this hole, and

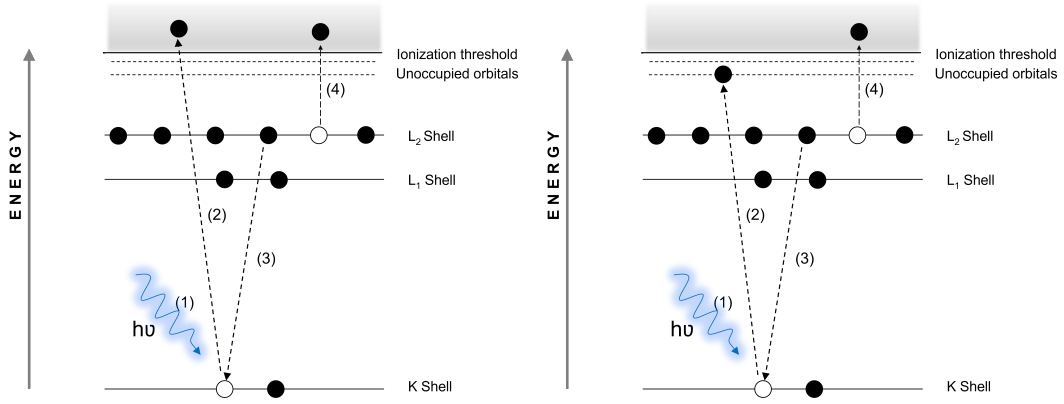

Figure 2.6: Non-radiative decay mechanisms after core-hole generation. (a) Auger decay after ionization of one core-shell electron; (b) shows one relaxation pathway for the resonant Auger decay after excitation of the inner-shell electron to one of the unoccupied excited states.

a second electron from the L shell is ejected, and this is called an Auger electron.

Suppose the initial photon interacting with the neutral atom is not sufficient to ionize but capable of promoting an electron from the core-shell to an excited state. In that case, it can initiate a resonant Auger decay, as shown in 2.6. In this case, the incoming photon resonantly excites one of the K shell electrons, and the following charge rearrangement is the same as in the KLL Auger process.

Auger decay and fluorescence are two competing processes. Figure 2.7 shows their yield comparison with the photoionized shell and atomic number (Z) [31] [32]. The fluorescence yield increases with an increase of Z, with Z >30, radiative decay dominant after the K shell ionization. The Auger process is dominant for L-shell electrons of atomic number $Z \leq 9$.

In addition to single-photon ionization, further processes may occur for photon energies below the ionization threshold, which are generated from intense pulsed laser sources, such as tabletop optical or FELs. In this case, the atom interacts with multiple photons simultaneously, resulting in the sequential absorption of many photons, a phenomenon known as multi-photon ionization (MPI). Above-threshold ionization represents an extension of MPI and occurs when an electron absorbs more photons than are necessary to overcome the ionization threshold [34]. The atom that has been ionized via one of the previously mentioned processes subsequently decays via a secondary mechanism, as mentioned before. Furthermore, a double vacancy in the inner-shell may also be generated, which can undergo a non-radiative decay known as double-core-hole (DCH) Auger decay. Fourth-generation light sources, such as FELs, can generate short pulses with high repetition rates and significant pulse energy. These photon pulses can create an additional hole in the inner-shell before the initially mentioned Auger

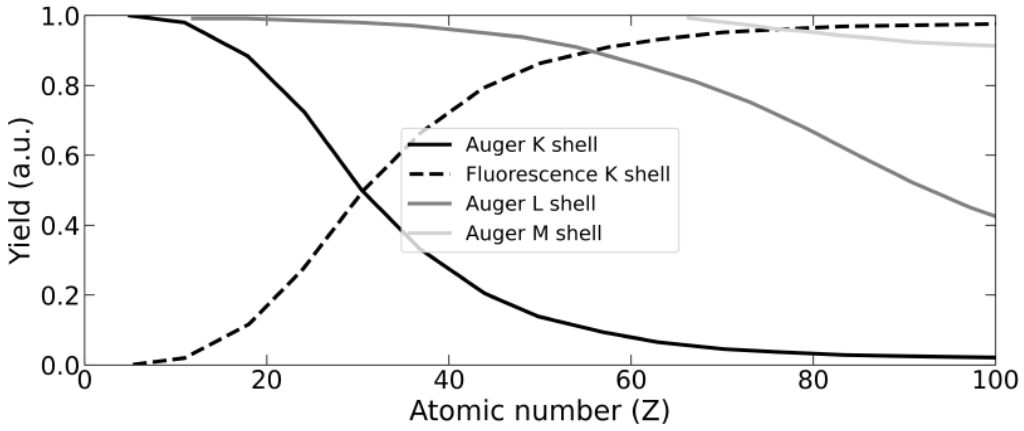

Figure 2.7: Yield comparison of Auger decay and fluorescence as a function of atomic number. Auger decay curves of K, L, and M shells, black with subsequent lighter shading for K, L, and M, respectively, and the fluorescence yield is represented with a dashed line. Image generated from [31–33].

process occurs. A detailed discussion of this process is in Chapter 5.

Creating an inner-shell vacancy in an atom may result in the subsequent excitation or ionization of the outer-shell electrons. The additional excitation of an outer shell electron to a bound state is called shake-up. In contrast, in the shake-off process, an electron is promoted to the continuum [35]. This shake process happens due to the sudden change in the potential of the atomic system. The potential seen by the outer electron will be different with the ionization of one of the screening electrons, meaning all the processes mentioned earlier, such as photoionization of the core-shell, fluorescence, and Auger process, can initiate this shake-up or shake-off process [36].

The three previously mentioned photon-electron interactions can be characterized spectroscopically and are independent spectroscopic fields. Photoelectron, Auger, and fluorescence spectroscopy provide information about the binding energies. Photoelectron spectroscopy provides the most straightforward insight into the binding energy of an orbital. Fluorescence emission depends on the energy difference between two energy levels. The connected dynamics of three electronic orbitals—the initial core hole, the relaxing electron, and the expelled Auger electron—make interpreting Auger spectra quite challenging. Auger spectroscopy provides critical new insights on electron–electron interactions and local electronic structure that direct photoemission cannot reveal, despite this complexity. [37].

2.3 Cross Section and Angular Distribution

2.3.1 Total and partial cross sections

The probability of a photon-electron interaction, particularly in the context of photoionization processes discussed in the previous section, is defined by the measurable quantity called cross-section, which provides insight into the likelihood of such interactions occurring [38]. In a classical approach, the cross-section is the ratio of the absorbing area in the target to the total area of the target [39]. In contrast, the cross-section of the interaction of electromagnetic radiation with a quantum mechanical system is explained by the transition probabilities obtained from Fermi's Golden rule [40] [38].

$$T_{i\to f} = \frac{2\pi}{\hbar}|\langle\Psi_f|\hat{H}_{ph}|\Psi_i\rangle|^2\delta(E_f - E_i - h\nu) \tag{2.4}$$

Equation 2.4 shows the transition probability $T_{i\to f}$ from the initial state with wave function Ψ_i and eigenvalue E_i to the final state with Ψ_f and E_f. $\hat{H}_{ph}$ represents the Hamiltonian corresponding to the interacting photon and the $h\nu$ is the photon energy. During the initial phase, the term "photoionization cross-section" represented the total cross-section, encompassing all ionization probabilities by the target. A partial cross-section represents the probability of ionization of a particular orbital in the target and is represented by [41],

$$\sigma_{if}(h\nu) = \frac{4\pi\alpha a_0^2}{3}h\nu|\langle\Psi_f|\sum_{\mu} r_\mu|\Psi_i\rangle|^2 \tag{2.5}$$

where α is the fine-structure constant and a_0 the bohr radius. $|\langle\Psi_f|\sum_{\mu} r_\mu|\Psi_i\rangle|^2$ represents the transition matrix element, in the dipole approximation, from state i towards f [41]. The total cross section can be represented as the sum of the partial cross sections as a function of photon energy [38].

$$\sigma_T(h\nu) = \sum_{i,f}\sigma_{if}(h\nu) \tag{2.6}$$

This description of the partial cross-section explains the energetically discrete photo lines due to the different subshells. In the past, the excitation energy dependence on the partial cross-section was less explored due to the unavailability of vacuum ultraviolet (VUV) and X-ray sources. The advent of monochromatized synchrotron/FEL radiation with a wide range of tunability in photon energy addresses this issue. Even though the total photoionization cross

section is not sub-shell sensitive, it is still interesting and can be experimentally measured by photo-absorption spectroscopy and the electron-energy-loss-spectroscopy [42] [43].

2.3.2 Differential cross section and angular distribution

The partial photoionization cross-section does not provide any information about the angular momentum quantum number of the ejected photoelectron [38]. The derivative of a partial cross-section with a solid angle is called the differential cross-section. The differential cross section for photoionization of an unpolarized target with the linearly polarized incident photon in the electric dipole approximation can be written as [44] [45],

$$\frac{d\sigma_T}{d\Omega} = \frac{\sigma_T}{4\pi}[1+\beta P_2(cos\theta)] \tag{2.7}$$

and

$$P_2 cos\theta = \frac{3cos^2\theta - 1}{2} \tag{2.8}$$

Where Ω is the solid angle, $P_2(cos\theta)$ is the second-order Legendre polynomial, and θ is the angle between the photoelectron and the polarization of the incident photon. [41]. The asymmetry parameter β is the determining factor of angular distribution in equation 2.7, which contains the relevant dynamical information about the distribution of photoelectrons.

Equation 2.7 will be changed if the incident photon is circularly polarized. One can assume the circularly polarized light as the linear sum of two coherent linearly polarized beams with the same intensity vibrating 90° out of phase along the orthogonal axes of the beam propagation. Thus, the differential cross section due to a circularly polarized incident photon will be,

$$\frac{d\sigma_T}{d\Omega} = \frac{\sigma_T}{4\pi}[1-\frac{1}{2}\beta P_2(cos\Theta)] \tag{2.9}$$

σ_T is the total cross-section, and Θ represents the polar angle between the incident light propagation direction and the emitted photoelectron momentum direction. The detailed mathematical derivation of equations 2.7 and 2.9 can be found in [45]. There is a requirement for the $\frac{d\sigma_T}{d\Omega}$ to be positive for all values of θ, thus implying the possible value of β in the range $-1 \leq \beta \leq 2$. For a detailed understanding of the mathematical expression of β, one can read the publication of Cooper and Zare [44]. Figure 2.8 shows the angular distribution corresponding to the different values of the asymmetric parameter. $\beta = 0$ represents an isotropic angular distribution. In contrast, at $\theta = 54.7°$ with the linearly polarized photon, the Legendre polyno-

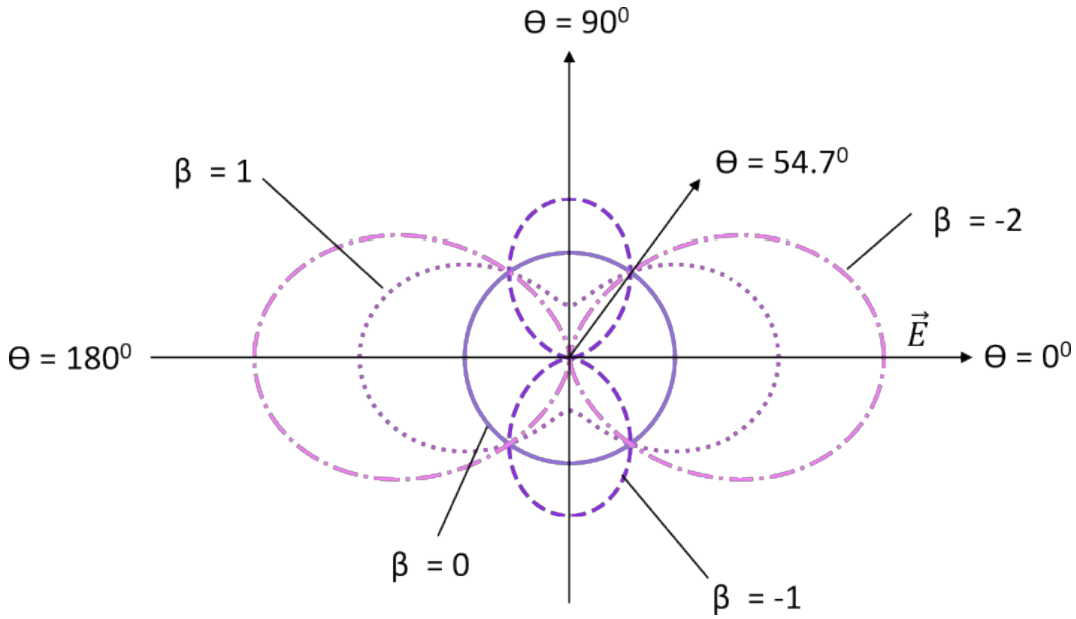

Figure 2.8: Two-dimensional representation of anisotropic parameter β with values $-1 \leq \beta \leq 2$. The horizontal axis represents the direction of the electric field, and the vertical axis represents the direction of the photon beam. Magic angle is marked at $\theta = 54.7°$.

mial of the second degree becomes zero. At this angle, there will be no additional information available regarding the angular distribution, and this angle is called ”magic angle” [41].

With advancements in the spectroscopy field, differential partial cross sections measured using angle-resolving photoelectron spectroscopy (ARPES) and other measurement schemes, such as ion yield measurement [46] and fluorescence detection [47] [48], have been reported in the literature. The asymmetry parameter can characterize the angular distribution from the different atomic orbitals of the ionized target. These differential cross-section measurements can provide data about the magnitude of the particular transition and its relative phase information [45].

All the explanations and equations mentioned above are discussed, assuming the electric dipole approximation is valid. In the electric dipole approximation, the atom or molecule is treated as a point-like object with an electric dipole moment. This is valid when the photon wavelength is much larger than the size of the target [45]. Until early 2000, it was believed that the non-dipole effects in photoionization were dominant for a few keV photon energies and were negligible for lower photon energies [49] [50]. However, studies have been published where the non-dipole effect is observed for a few tens of eV of photon energy for the Xenon 5*s* photoionization studies [50].

2.4 Free-Electron Lasers

To characterize and perform the photoionization and structural analysis of atomic and molecular targets, it is essential to have an electromagnetic radiation source that can be tuned over a wide range of photon energies. FELs [51] [52] are a revolutionary advance in the field of photonics, offering a cutting-edge light source for investigating a range of fundamental physical phenomena, such as capturing atomic-scale motion pictures of a chemical process, studying the structure of complex proteins [12], and other exciting areas of research [53, 54]. The high pulse energy and short pulse duration (ranging from femtoseconds to attoseconds) offered by FELs over a wide wavelength range make them unique tools for studying the photoionization process and the subsequent ultrafast relaxations. The present work investigates DCH Auger decay in gaseous neon using intense X-ray pulses available exclusively at free-electron laser (FEL) facilities. Hence, understanding the basic operating principles of FELs is crucial for the context of this thesis.

Following the development of the optical laser system in the visible and near-infrared regimes [55], scientists have perpetually desired to extend this effort to generate sources with shorter wavelengths. One of the major limiting factors for this effort was the difficulties in developing the population inversion [56] conditions for the X-ray wavelengths because of the very short lifetime of the energy states. Additionally, a substantial amount of energy is required to excite the core atomic levels [52]. Building low-loss cavities for the X-ray wavelength was difficult, so alternative attempts were made to develop high-intensity (peak power) short-pulse coherent sources [57] [52]. A review of the experimental efforts from the initial era of X-ray wavelength source generation can be found in [52, 58, 59].

A breakthrough came with the development of accelerator-based light sources, which exploit the radiation emitted by relativistic electrons, as they travel through magnetic fields. The evolution from bending magnets to wigglers, undulators, and ultimately to free-electron lasers (FELs) represents successive generations of X-ray sources, each with steadily improving spectral brightness, coherence, and tunability. Bending magnets produce broad, continuous spectra with low coherence, and the intensity is proportional to the number of circulating electrons. Wigglers, incorporating multiple alternating magnetic poles, enhance the overall radiation power but still yield a broad, incoherent spectrum. Undulators, with finely tuned periodic magnetic fields, enable partial constructive interference of the emitted radiation, resulting in narrower spectral features and increased brightness. In contrast, FELs exploit coherent amplification of the emitted light within the undulator, yielding discrete, narrowband spectra

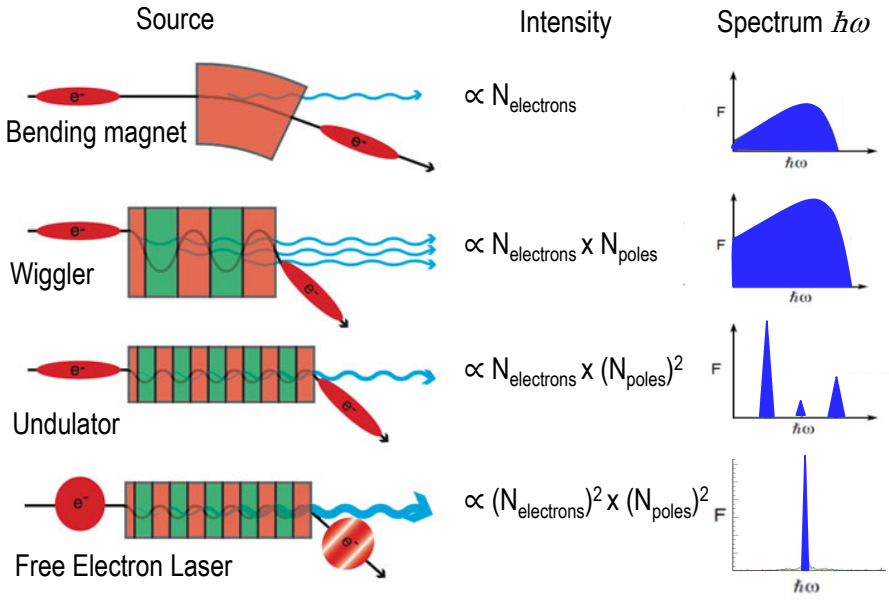

Figure 2.9: Schematic representation of radiation sources: bending magnet, wiggler, undulator, and free-electron laser, comparing their emission mechanisms, intensity scaling, and spectral output. The intensity increases with the number of electrons and magnetic poles. At the same time, the spectrum evolves from broad and incoherent (bending magnet and wiggler) to narrow and highly coherent (undulator and FEL). Image taken from [60].

with orders-of-magnitude higher brilliance, as illustrated in Figure 2.9.

A significant step beyond the spontaneous emission of these sources was the development of the self-amplified spontaneous emission (SASE) mechanism [61–63], which eliminated the need for population inversion. In this process, a relativistic electron generates X-ray radiation in a periodically changing magnetic field, known as an undulator. In 1970, Madey introduced the theory of FEL [64]. In 2000, the first observation of SASE in a FEL was demonstrated at Free Electron Laser in Hamburg, Germany (FLASH) in the ultraviolet regime, with a wavelength of 109 nm [8] [65] [66]. Subsequently, in 2009, the Linac Coherent Light Source (LCLS)at the SLAC National Accelerator Laboratory in the USA, recorded a short wavelength of 22 to 1.2 Å [7]. There are many other FEL facilities available around the world; some of them are SACLA in Japan [67], FERMI in Italy [68], Eu-XFEL [9] in Germany, SwissFEL in Switzerland [69], and Pohang Accelerator Laboratory X-ray Free-Electron Laser (PAL-XFEL) in Korea [70].

FELs generate photons with an exceptionally high brightness [52]. Where brightness/brilliance is the measure of the intensity of the radiation, or the number of photons produced per second. This can be represented as the photon flux ϕ divided by the divergence σ, size θ, and energy

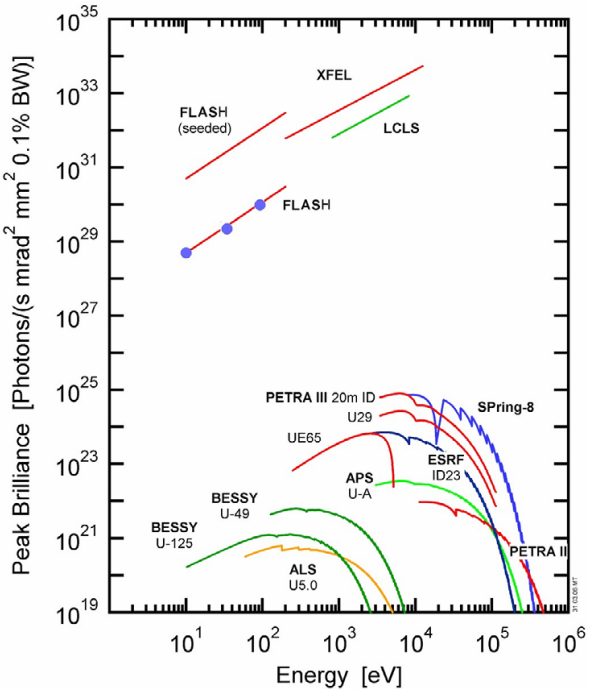

Figure 2.10: Comparison of X-ray facilities in terms of peak brilliance over photon energies, image taken from [71].

bandwidth ΔE [33].

$$B = \frac{\phi}{\sigma\theta\Delta E} \tag{2.10}$$

Figure 2.10 compares the leading X-ray FELs and other storage rings based on the peak brilliance [71]. The European XFEL can produce up to 10^{33} photons per second, providing the extreme photon flux required to induce nonlinear light–matter interactions such as DCH formation. This exceptionally high intensity is essential for achieving multi-photon ionization probabilities within the femtosecond timescale, where most of the experimental work in this study was conducted.

In simple words, FEL consists of an electron accelerator and an undulator magnet, as shown in Figure 2.11 (a). The photoelectrons generated by photoemission from a cathode are accelerated using linear accelerators (LINAC) from a few MeV up to 10 GeV. These accelerators operate either at room temperature or at superconducting temperatures [28] with an electron energy of 1-15 GeV, which is used in X-ray FELs [52].

The planar undulators have a sinusoidal magnetic field with a λ_u period and a magnitude of B_u typically around 1 Tesla. In this field, an electron travels in a sinusoidal, oscillating trajectory in a plane perpendicular to the magnets, generating electromagnetic wave trains.

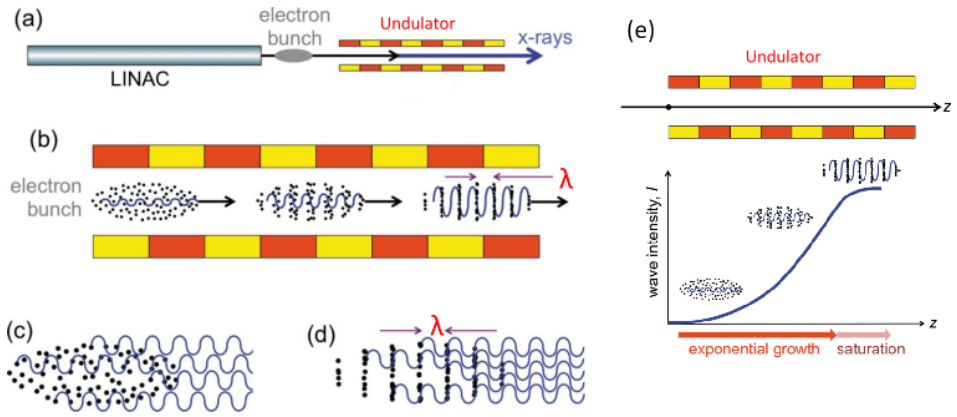

Figure 2.11: Schematic of the working of SASE FELs. (a) shows the overall schematic of the FEL, including the linear accelerator and undulator. (b), (c) and (d) represent the energy and density modulation that happens when the relativistic electron travels through the undulator field. (e) Gain curve of the SASE process. Image modified from [73].

These have a number of periods, the same as the undulator period N_u. The wavelength of the radiation emitted on axis is proportional to the undulator period reduced by the relativistic factor and the energy of the electron, and can be represented by,

$$\lambda \simeq \frac{\lambda_u}{2\gamma^2}(1+\frac{K^2}{2}) \tag{2.11}$$

where γ is the energy of the electron, and K is the undulator parameter or deflection parameter,

$$K = \frac{eB_u\lambda_u}{2\pi mc} \tag{2.12}$$

m is the electron rest mass, c is the speed of light, and e is the elementary charge [72]. The quadratic dependence of the electron energy makes it easy to generate shorter wavelengths with an electron beam with GeV energy. Higher-energy electrons can generate shorter-wavelength radiation, as they are inversely proportional to each other.

The electrons travelling through the undulator field interact with the radiation generated by other electrons, creating a change in the electron energy (energy modulation). Due to this energy modulation, The length of the electron trajectory changes, and the electrons within one radiation wavelength tend to get nearer to each other. This causes the microbunching of the electrons in the longitudinal direction with a separation equal to the wavelength of the emitted radiation. Since the electrons in a wavelength are closely spaced, they can create a total field by superimposing the individual electromagnetic fields in phase. The X-ray radiation is faster

than the electrons, and the electrons will ”slip” back by one wavelength per undulator period. So, the radiation from the preceding electron bunch stimulates further emission, and thus, the SASE starts [12]. These processes are shown in Figure 2.11 b-d. The amplification saturates once the micro-bunching is complete [72]. Figure 2.11 (e) shows the schematic representation of the microbunching process along the undulator distance, modified from [73]. For high-gain FELs, the undulator sections are longer, typically a few hundred meters.

The radiation emitted from the FELs exhibits stochastic behaviour due to its origin from the random emissions of the undulator radiation. The individual FEL pulse, sometimes referred to as a shot or pulse, differs in intensity, temporal, and spectral distribution. This feature of starting from noise and amplifying to saturation in a single undulator pass makes it unique and distinct from the standard laser, which operates based on population inversion [12].

The generated X-ray is transported through the photon beamlines under ultra-high vacuum conditions and served to the users. Meanwhile, the electron beam is dumped into an electron beam block. Multiple non-invasive diagnostic schemes are available along the beamline. Some of them include the gas monitor detectors (GMD), which provide pulse energy of the individual pulses [74]. The beam arrival monitor (BAM) [75] provides the pulse arrival time, which is crucial for experiments that require synchronization with an external optical laser. The photoelectron spectrometer (PES) installed at the beginning of the beamline provides information about the polarization of the beam [76].

2.4.1 FEL-Based Time-Resolved Studies

The fundamental working principles and unique properties of free-electron laser (FEL) pulses, particularly in comparison to other VUV and X-ray sources, have already been discussed in Section 2.4. FELs offer exceptionally high peak brilliance combined with ultrashort pulse durations on the femtosecond to attosecond scale. These characteristics make them uniquely suited for investigating ultrafast phenomena such as electron dynamics in atoms and molecules, charge migration, and photodissociation processes, all of which occur on femtosecond to attosecond timescales [77]. This section highlights selected time-resolved experimental schemes that utilize FELs to probe these fundamental processes.

Pump-probe measurements

Pump-probe experiments are powerful tools for studying the dynamics of materials and molecules on extremely short timescales, typically in the femtosecond range. In these experiments, two laser pulses are employed. The first is the pump pulse, which excites, ionizes, or manipulates

the target, effectively making the system unstable and triggering a process that changes its properties [33]. Meanwhile, the probe pulse arrives after a controlled delay and measures the system's transient response, providing a time-resolved picture of its evolution. The delay between the pump and probe pulses can be controlled externally or internally (if the same laser source is used for both). By varying the time delay between these, one can obtain time-resolved information about the initiated process over time, which helps to understand the evolution of a complex chemical process or study the transient states of matter.

Pump–probe studies with FEL pulses represent a cutting-edge approach for investigating ultrafast dynamics, combining femtosecond temporal resolution with the ability to probe core-level transitions using intense, tunable X-ray pulses, a capability beyond the reach of tabletop laser sources. There are multiple ways to include FELs in these schemes, primarily the FEL-pump optical laser-probe, optical laser-pump, and FEL-probe, as well as the FEL-pump FEL-probe. The FEL-pump and optical laser-probe scheme utilizes the intense and short X-ray pulse from the FEL for excitation, ionization, or dissociation. The optical laser pulse is used for probing the response of the target at various time scales. In optical laser-pump FEL-probe experiments, an external optical laser is used in conjunction with the FEL. Time-resolved spectroscopy after optical excitation can provide insights into the charge transfer following fragmentation [78] [79] [80]. The timing reference provides a common clock for both pulses, ensuring precise synchronization in pump–probe experiments. The synchronization and control of the time delay between these two pulses is a complex task. It is essential to calibrate and optimize the timing tools to ensure stable synchronization [81] [82] [83].

A different class of pump-probe studies is the FEL-pump FEL-probe scheme, where both the pump and probe are X-rays from the same train of pulses. This setup is particularly useful for site-specific excitation of core electrons [84], nanocrystallography [85], and the study of radiation-induced rearrangements in protein structures [86]. Since both pulses originate from the same pulse train, they are internally synchronized. However, unlike setups involving an external laser probe, it is not possible to scan a variable time delay between the pulses.

One promising alternative in this context is pump-probe ghost imaging (PPGI) [87], which falls under the category of FEL-pump FEL-probe. This technique is inspired by conventional ghost imaging (GI), where a beam is split into two arms: the object arm, which interacts with the sample and is recorded by a low-resolution detector, and the reference arm, detected by a high-resolution detector without sample interaction. Due to the inherent shot-to-shot fluctuations of SASE FEL pulses, many such measurements are collected, and the correlation between the two arms is computed. In contrast to traditional pump-probe experiments, which rely on two separate pulses delayed by a time τ, PPGI uses a single FEL pulse whose internal

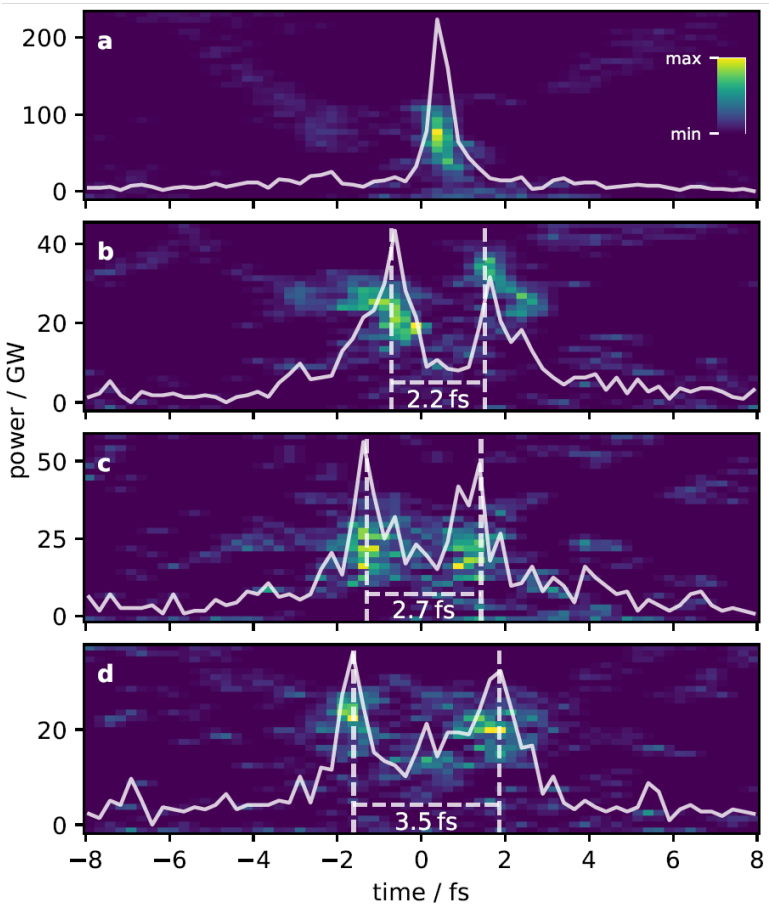

Figure 2.12: Representation of different FEL pulses. (a) Shows an example of a single spike pulse where (b),(c), and (d) represent two spike pulses with different delays between the two spikes. Image taken from [88].

intensity fluctuations effectively act as many overlapping pump–probe events with a distribution of time delays. Figure 2.12 illustrates such intensity variation within a single pulse with different delays between the individual spikes in an FEL pulse. Additionally, FEL-pump FEL-probe experiments can be implemented in one-colour or two-colour schemes, where the two photons have identical or distinct photon energies, respectively. This domain is broad and evolving rapidly. While it is beyond the scope of this thesis to provide a comprehensive coverage, interested readers are referred to the relevant literature [89] [90] [91] [92].

2.4.2 Investigation of ultrafast nonlinear phenomena

In addition to classical pump-probe studies, ultra-short FEL pulses with high peak power are a valuable tool for accessing nonlinear phenomena in the gas phase that regular optical

laser pulses cannot initiate. FEL pulses are handy tools for gas-phase studies, offering high repetition rates, short-duration pulses, and focusing possibilities of a few micrometres. A detailed review of the possibilities of gas phase studies with undulator-based polarization control at different FELs can be found in the work of M. Ilchen et al. [54].

Among the many advanced spectroscopic techniques in FEL science, ultrafast Auger spectroscopy holds particular importance. These are considered to be a unique tool for mapping electron dynamics due to the charge rearrangements that follow the ionization of a core-shell. These site-specific Auger electron yields resemble the ultrafast electron dynamics on the few-femtosecond scale. Mapping such short-lived neon DCH using high-repetition-rate and highly focused pulses is characterized at Eu-XFEL. Tunability of the FEL pulses allows access to multiple Rydberg state excitations following core ionization [17]. The availability of such intense pulses opens a field of opportunity to investigate the highly ionized neutral gas target by multi-photon absorption [93]. Multiple interesting studies have been conducted on the light–matter interaction at exceptionally high intensities [53, 94, 95].

Moreover, FELs facilitate investigations into high-harmonic generation (HHG), multiphoton ionization, and a range of other nonlinear optical processes that occur in the X-ray and extreme ultraviolet (XUV) spectral regions. Traditionally, non-linear optics has been limited to the infrared and visible domains due to the insufficient photon flux in higher-energy ranges. FELs overcome this limitation by delivering ultrashort pulses with peak intensities exceeding 10^{16} W/cm^2, enabling non-linear phenomena to be driven at X-ray wavelengths for the first time.

In the context of HHG, FELs enable the exploration of the interaction between intense X-ray fields and atoms and molecules, resulting in the emission of photons at integer multiples of the driving field frequency. This process, analogous to HHG in the optical domain, provides a powerful probe of ultrafast electron dynamics and offers potential routes toward attosecond X-ray pulse generation. FEL-driven HHG also opens new opportunities for developing compact, tabletop coherent X-ray sources [96].

Multiphoton ionization in the X-ray regime, where multiple photons are absorbed simultaneously to eject one or more electrons, provides a window into highly nonlinear regimes of light-matter interaction. FELs enable these processes to be studied with element specificity and site selectivity, offering insights into correlated electron motion, inner-shell dynamics, and Auger decay cascades. These mechanisms are essential for understanding radiation damage in biological systems and for advancing ultrafast imaging techniques [93]. These nonlinear X-ray interactions push the frontiers of fundamental atomic and molecular physics, and have far-reaching implications for materials science, photochemistry, and quantum technolo-

gies [97].

2.4.3 Inner-shell ionization and electron dynamics

The advent of FELs, particularly those operating in the XUV and soft to hard X-ray regimes, has opened new frontiers in studying site-specific ionization and ultrafast charge migration in atomic and polyatomic systems. By tuning the photon energy to match a specific core-level binding energy, FELs allow for the initiation of inner-shell ionization processes with element and site selectivity. This capability is essential for complex molecular systems, where different atomic sites contribute uniquely to the electronic structure and chemical reactivity [98].

Upon absorption of an X-ray photon with energy greater than the binding energy of a core electron, it ionizes one of the core electrons, leaving behind a highly localized core hole. An Auger relaxation process follows this initial ionization event. As a result, two or more vacancies are created in the valence shell, generating a multiply charged intermediate state. The newly formed positive charge is initially localized near the ionized site, but rapidly delocalizes throughout the molecule via ultrafast charge transfer processes, driven by Coulombic repulsion and the electronic coupling between molecular orbitals. This intramolecular charge migration can occur on the sub-femtosecond to few-femtosecond timescale.

Molecular dynamics followed by the photoexcitation is the basis of many processes in nature, from light harvesting, photochemistry, and radiation protection [53]. Ultrashort soft and hard X-rays help to understand the interplay between initial motion and the final chemical changes in the excited species [99]. If a second photon with sufficient energy subsequently ionizes or resonantly excites the remaining inner-shell electron, before the Auger decay happens, a DCH state is produced. This DCH state also undergoes Auger decay, and its formation and decay dynamics in the gas phase have been characterized with neon [17] and argon [100].

FEL-based time-resolved pump-probe experiments are uniquely suited for real-time tracking of these electronic rearrangements. The ability to generate isolated core holes with high temporal precision enables the investigation of non-equilibrium electronic states and the mechanisms by which charge propagates through covalent frameworks or functional groups. A study in this field was presented by B. Erk et al., where inner-shell ionization of the iodine 3d orbital in methyl iodide (CH_3I) was used to initiate charge migration. Following ionization, an NIR laser pulse probed the ensuing charge transfer between the iodine atom and the methyl group. The dynamics were monitored as a function of the interatomic separation, effectively mapping the interplay between electronic and nuclear degrees of freedom. The study

demonstrated that the timing of electron transfer is strongly dependent on molecular geometry and can be modulated by controlling the delay between the X-ray and optical pulses [101]. M. Richter et al. demonstrated two-photon inner-shell ionization in xenon using extreme UV (XUV) photons from FLASH [102], showing the capability of characterizing these inner-shell ionization pathways at a FEL facility. Similarly, L. Young et al. showed multiphoton inner-shell ionization and the resultant Auger cascades in neon and other rare gas atoms. This work emphasized the importance of sequential versus direct ionization pathways and provided insights into how core-excited states decay via multi-step electron ejection. In molecular systems, such cascades lead to ultrafast charge redistribution, which in turn influences fragmentation channels [93]. Excited-state isomerization of acetylene using XUV photons from FLASH was examined using the coincidence method [103].

Another approach is the use of Coulomb Explosion Imaging (CEI), where the positions of molecular fragments after core ionization are recorded to reconstruct the evolution of the charge cloud before dissociation [104]. F. Légaré et al. showed that laser-induced CEI could capture femtosecond-resolved bond-breaking events and intramolecular rearrangements, highlighting its utility in visualizing real-time chemical dynamics [105]. More recently, F. Allum et al. applied CEI to CH_3I and CH_2ClI, uncovering the dissociation pathways and molecular frame charge dynamics that occur during photoionization [106]. A significant advancement in this field was presented by R. Boll et al., utilizing the potential of X-ray multiphoton-induced CEI to image complex polyatomic molecules using intense FEL pulses [107].

All of these studies show the capability of FELs to probe inner-shell ionization and subsequent charge transfer with site-specificity and temporal resolution. These studies have significantly advanced our understanding of electronic dynamics. Continued development in FEL pulse shaping, short-pulse generation, and detection techniques will further elucidate the fundamental processes that govern photoinduced chemistry, charge migration, and energy redistribution at the most fundamental level.

Chapter 3

The Angle-Resolving Electron-Time-of-Flight Spectrometer

3.1 Photoelectron Time-of-Flight Spectroscopy

Photoelectron spectroscopy is a promising technique for understanding the light–matter interactions, with implementations across a wide range of photon energies, including ultraviolet, visible, X-ray, and infrared. This can provide information about the orbitals and electronic configurations of valence and inner-shell electrons in different types of samples, including atoms, molecules, clusters, and solids [108]. The underlying principle behind the photoelectron spectroscopy is the photoelectric effect (explained in detail in section 2.2). The photo-ejected electron kinetic energy is mapped by measuring the travel time from the interaction region (point of origin) to the final detector (flight time) [109]. In the angle-resolved mode, the electrons are distinguished by their kinetic energy and the emission direction. Angle-resolving photoemission spectroscopy (ARPES) is used for characterizing the fundamental light-matter interactions that are phase-sensitive [110].

ARPES can be explained as a photon-in, electron-out process. Electromagnetic radiation with a photon energy of hν, where h is Planck's constant and ν is the frequency, can eject an electron from an atom if its energy is greater than the binding energy ($E_{Binding}$) of the electronic state, resulting in an emitted electron with kinetic energy (E_{KE}). The relationship between the incident photon and the outgoing electron is given in equation 2.2, which is based solely on energy conservation. An angle-resolving spectrometer records the intensity distribution of the photoelectron as a function of flight time (later converted into kinetic energy) and emission angle [110].

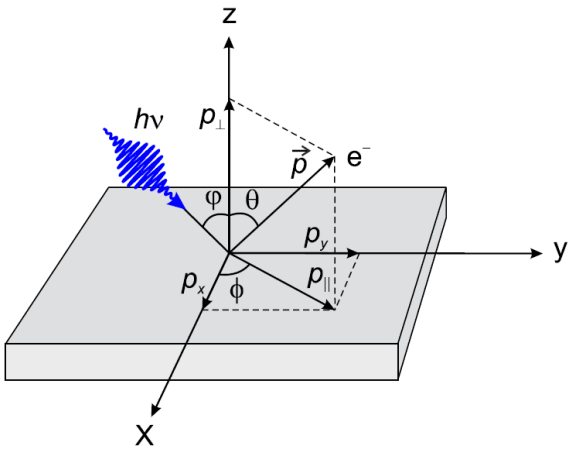

Figure 3.1: Schematic of the experimental geometry showing the different parameters of the photoemission process. Where $h\nu$ is the photon energy of the incoming photon beam at an angle of incidence of ψ. θ and ϕ are the polar and azimuthal angles of photoemission, respectively. The momentum of the photoelectron p is shown with its in-plane and out-of-plane components $p_{\parallel}$ and $p_{\perp}$. Image taken from [109].

The technique of time-of-flight (TOF) photoelectron spectroscopy has advanced significantly with the advent of state-of-the-art fourth-generation light sources, which provide intense, ultrashort, and tunable pulses, enabling time-resolved measurements, improved signal-to-noise ratio, and access to non-linear photoionization processes. This chapter mainly discusses the building and characterization of such a spectrometer. This chapter is structured as follows: the basics of TOF spectroscopy will be addressed first, and the following electron-TOF apparatus built during this thesis work will be explained in detail.

3.1.1 Working principle of time-of-flight detectors

The photoelectron emission from a surface is shown in Figure 3.1. The XY surface represents the sample surface with the normal oriented in the Z direction. Photons with energy of hν hit the surface at an angle of ψ to the normal, and the photoelectrons are emitted with a momentum of P. The photoemission angle θ is defined relative to the surface normal, while the azimuthal emission angle ϕ is defined relative to a crystal axis. The experimentally measured parameters are the angle of emission and the TOF of electrons. The kinetic energies of the photoelectrons are determined from the flight times between the interaction point and the detector. Every emitted electron corresponding to a particular event is captured simultaneously, with multiple individual peaks representing the different photoelectrons generated by the same incident beam. The incident photon generates the photoelectrons, and the TOF spectrometer

collects these electrons, which travel inside the spectrometer and are finally detected by the detectors. The detectors give information about the arrival time; for high-energy electrons, the flight time will be shorter and vice versa. Different trajectories within the spectrometer also result in TOF differences despite having the same kinetic energy.

The kinetic energy E_{kin} is calculated for a finite drift length d with a time-of-flight t.

$$E_{kin} = \frac{m_e}{2}\left(\frac{d}{t}\right)^2 \tag{3.1}$$

where m_e is the electron mass. The achievable energy resolution with overall experimental accuracy in TOF (Δt) can be represented as

$$dE_{kin} = \frac{\partial E_{kin}}{\partial t}dt = -m_e d^2 t^{-3} dt \tag{3.2}$$

$$\Delta E_{kin} \approx \frac{m_e d^2 \Delta t}{t^3} \tag{3.3}$$

from equation 3.1

$$t = d\sqrt{\frac{m_e}{2E_{kin}}} \tag{3.4}$$

$$t^3 = d^3 \frac{(m_e)^{3/2}}{(2E_{kin})^{3/2}} = \frac{d^3 (m_e)^{3/2}}{\sqrt{8}E_{kin}^{3/2}} \tag{3.5}$$

Substituting 3.5 to 3.3

$$\Delta E_{kin} = \sqrt{\frac{8E_{kin}^3}{m_e}}\frac{\Delta t}{d} \tag{3.6}$$

Shorter FEL pulses and high brightness improve signal quality by enhancing the signal-to-noise ratio; however, careful optimization is required to preserve energy resolution in TOF spectroscopy. The energy resolution mainly depends on the spread of the transit times of the electrons with the same energy. Although the electrons are generated simultaneously with the same energy, their arrival times at the detector after traveling through the flight can be different if they take different trajectories. Different trajectories result in different path lengths, and if the time difference is significant, then the intensity distribution of these electrons will be separated in the TOF spectrum. The energy resolution can be improved by providing additional deceleration of electrons in the flight path using retardation sections. The retardation section is connected to the external negative bias, which causes the trajectory electrons to

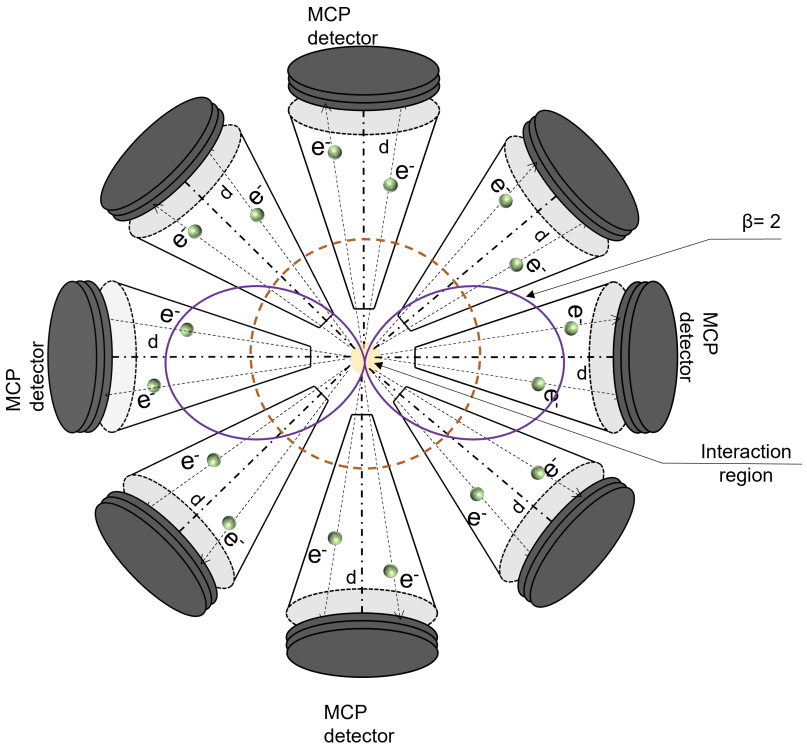

Figure 3.2: Schematic of the angle-resolving TOF spectrometer setup. The diagram illustrates eight TOF spectrometers symmetrically arranged around the interaction region (highlighted in yellow). Two example angular distributions are shown: one with an anisotropy parameter of $\beta = 2$ (purple) and another with $\beta = 0$ (orange), representing distinct photoelectron emission patterns.

become more focused and slower, depending on the amount of voltage applied.

In e-TOF spectroscopy, electron detection is commonly achieved using a microchannel plate (MCP) detector, which converts incoming electrons into electrical signals. These signals can be acquired in either analogue or digital operation modes. In the analogue mode, the MCP output is recorded as a continuous voltage trace, preserving detailed peak shapes and allowing high dynamic range analysis. In contrast, the digital mode captures discrete electron arrival times using time-to-digital converters (TDC), offering high time resolution and faster data acquisition, particularly suitable for low count rates. The choice between analogue and digital acquisition depends on the experimental requirements, such as signal intensity, resolution, and data throughput.

The spectrometer setup discussed in the following section has an angular resolution with a large opening angle and is an interesting apparatus for characterizing angle-resolved studies. One such application is the temporal characterization of the stochastic X-ray pulses from FELs

by angular streaking (detailed description in Section 4.1) [111]. The inherent polarization of the incoming beam can also be measured using the photoelectron angular distribution [112]. Figure 3.2 shows the schematic representation of an angle-resolving TOF spectrometer with two different angular distribution patterns. Multiple other spectroscopic characterizations are possible with this setup, but they are beyond the scope of this work.

3.2 Vacuum System Setup

A key focus of this thesis is the adaptation of detector design, construction, and commissioning of an angle-resolving electron-TOF (e-TOF) spectrometer intended for use as an end station at Eu-XFEL for X-ray beam diagnostics. The spectrometer was initially designed and developed for beam characterization at the variable polarization VUV beamline P04 at PETRA III [113]. The mechanical design is maintained as the original version, but the electronic outcoupling of the signal from the spectrometer is further developed during this work.

The angular distribution of the photoelectrons generated by the gaseous target's ionization can provide information about the beam. The arrangement of 16 individual e-TOF spectrometers in a plane perpendicular to the X-ray beam propagation enables angle-resolved studies of photoelectrons using X-rays. While the setup is versatile and can accommodate a variety of targets, the commissioning and experiments conducted in this work primarily focused on gaseous noble gases. The target gas is selected based on the X-ray beam properties, such as photon energy and the photoionization cross-section of the gas at a specific photon energy.

This apparatus was mainly built to characterize the stochastic X-ray pulses of Eu-XFEL using the angular streaking technique (details in section 4.1). The setup offers valuable insights into the duration and polarization of the incoming X-ray beam, thus enabling more robust and non-invasive diagnostics.

All the individual e-TOF spectrometers are housed within a vacuum chamber, a cylindrical structure featuring two CF250 side flanges and 16 CF40 hexagonal flanges, as depicted in Figure 3.3. The side flanges are equipped with additional flanges to accommodate essential components of the experimental setup. These components include the vacuum peripherals, pressure gauge, residual gas analyzer (RGA), and gas delivery system. Ultra-high vacuum conditions, on the order of 10^{-8} mbar, are achieved using a scroll pump and two oil-free, non-magnetic turbo molecular pumps (TwissTor 84 FS) with a capacity of 80 litres each. These turbo pumps' oil-free and non-magnetic properties make them highly suitable for studies involving low kinetic energy electrons, as an external magnetic field can substantially affect the

low energy electron trajectories.

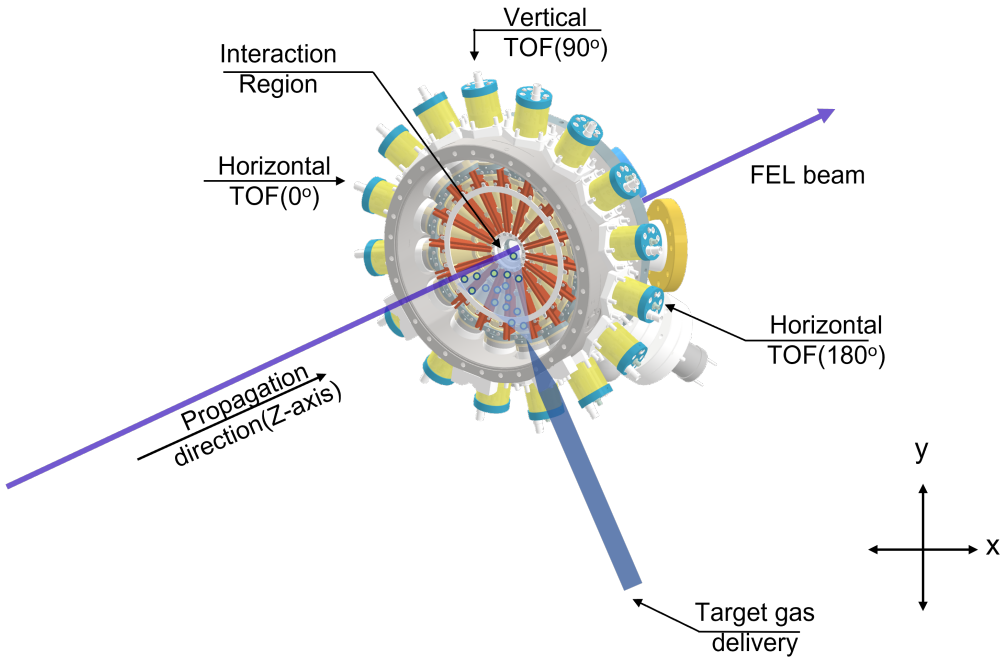

Figure 3.3: Schematic of the vacuum chamber with 16 e-TOF spectrometers. The e-TOF spectrometers are aligned perpendicular to the X-ray beam propagation. The interaction region is the area where the focused FEL beam ionizes the target gas. A schematic of the diffusive gas delivery is shown. Figure created from the CAD drawing provided by Frank Scholz of PO4 at PETRA III.

The gas delivery system consists of a minican of target gas connected to the long gas needle with an opening of a few hundreds of micrometres in diameter. The gas needle is mounted onto the chamber using a motorized XYZ manipulator. These encoder-based manipulators provide precise information about the motor position, which is a significant aid during needle alignment and final setup. Gas flow into the needle is regulated using a needle valve that can be operated in either flow or pressure mode. These valves precisely set the target gas flow into the chamber without disturbing the vacuum inside. The pressure inside the chamber is measured using Pirani gauges (FRG 730). 16 individual e-TOF spectrometers are connected to the main chamber through the CF 40 flange. X-ray beam enters and exits the chamber via the centre CF40 flange.

One of the CF40 flanges on the CF 250 side flange (not visible in Figure 3.3, as it is cut open for better visibility) is connected to an RGA to check for any residual gases inside the chamber. The RGA spectrum gives information about the particles and other gases inside the

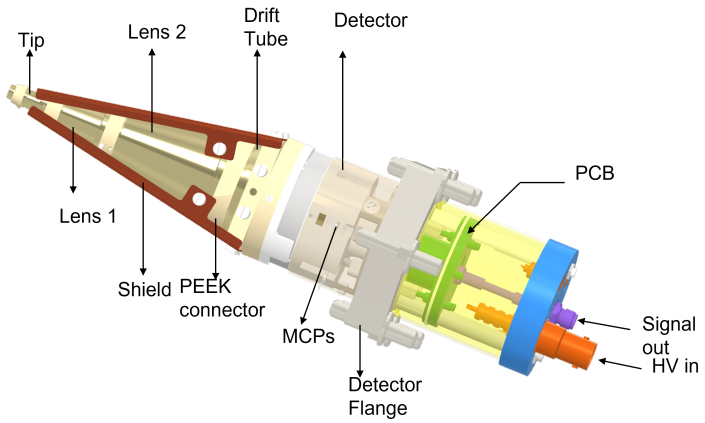

Figure 3.4: CAD model of the individual e-TOF Spectrometer. Electrons enter the spectrometer through the tip at ground potential and pass through the various lens sections and the drift tube. The detector marked in this figure is MCP-based and assembled inside a PEEK cage. HV_{in} gives the voltage supply to the voltage divider circuit of the MCP detector. The signal output is typically the SMA signal cable, which is usually connected to the digitizer channel.

chamber. Any residual gas or particle other than the target gas can affect the quality of the signal. Additional care is taken while preparing and assembling individual parts to reach the desired vacuum level. Additional baking is performed to remove residual gases, especially the water vapor, from the internal surface, thus improving the vacuum level. The chamber is heated to 60 °centigrade, as the MCPs have a certain temperature threshold that they can withstand.

3.3 Spectrometer Design and Performance

The CAD drawing of the e-TOF spectrometer is shown in Figure 3.4. An individual e-TOF spectrometer comprises a flight tube section, an MCP-based detector section, and a peripheral electronic circuit that powers these sections. The flight tube section can be further subdivided into a tip, focusing lens sections, and a drift tube. Positioned closest to the interaction region, the tip serves as the initial entry point of the spectrometer. The geometrical acceptance of the spectrometer is primarily determined by the opening diameter of the tip, which measures 4.2 mm, resulting in an acceptance angle of 0.28% of 4π.

The lens sections, positioned after the tip, are capable of focusing the electron trajectories when external bias voltages are applied. These voltages are supplied via RC circuits located

outside the vacuum chamber. The final cylindrical section of the spectrometer with the maximum voltage applied is called the drift tube. All sections are constructed from aluminium and coated with gold to minimize unwanted charge accumulation caused by interactions with primary electrons. Each section is securely positioned and electrically insulated from the others using polyether ether ketone (PEEK) rings (grey ring-like structures labelled as 'PEEK connectors' in Figure 3.4). By carefully selecting different sets of voltages, typically negative, the electron trajectories inside the flight tube can be focused and decelerated (for a more detailed explanation, refer to Section 3.4). This process of reshaping and deceleration enhances the spectrometer's energy resolution and transmission efficiency.

The detector section comprises three MCP plates arranged in a Z-stack configuration. The individual MCP plates have an active diameter of 26 mm, a channel diameter of 10μm, and a temporal resolution of $\leq$ 1 ns full width at half maximum (FWHM). A factor of $\approx$2500 amplification of electrons that hit the individual MCP plate. The Z-stack configuration creates an electron avalanche; these electrons are capacitively outcoupled. Additionally, a mesh with 85% transmission is used between the flight section and the MCP stacks to prevent any field penetration. Appropriate bias voltages are provided to the MCP stack's front and back using the newly developed PCB-based electronic circuit (details in section 3.12).

3.4 SIMION Simulation of the Spectrometer Performance

The electron-optic simulation of photo-ionized electrons helps to understand the overall performance of a newly built spectrometer, particularly its energy-resolving capability and total transmission at specific settings. SIMION [114] is an interactive, PC-based simulation program that utilizes the potential arrays that define the spectrometer's geometry and the potentials of each electrode. The different sections of the spectrometer model are considered as the electrodes. The potentials of all points outside the electrodes are determined by solving the Laplace equation, by a process known as "refining". The trajectories of electrons/ions will be changed based on the electric or magnetic fields created by the electrodes. The program enables the creation of various sets of particles that resemble actual photoelectrons or ions. These particles are subjected to "fly" in the fields created by the potential arrays, Figure 3.5 shows the trajectory of electrons that fly from the interaction point (0,0) to the MCP plates with two different sets of voltages applied across the lens sections. The tool offers data recording options, facilitating a deeper understanding of the electrons generated.

With different settings for lensing voltage, the overall transmission changes. Figure 3.5 shows the electron trajectory inside the spectrometer without any applied voltage to the lens (top panel), with a positive voltage applied to the front plates of the MCP, and the bottom panel illustrates the focusing effect of the trajectory with the applied voltage. Electrons with an initial kinetic energy of 150 eV are used to simulate their trajectories, since this value represents a typical energy within the range anticipated during the experiments, which may vary above or below this value. The cone distribution of electrons has a half-angle of 5.7 degrees. The distribution angle of the source is selected to match the geometrical acceptance angle of the MCP plate from the IP. One can choose multiple types of electron sources, like point source, circular and line source, from the SIMION, and the one used for Figure 3.5 is a point source. The focusing effect is energy-dependent; therefore, one must carefully select the retardation voltage for low and high kinetic energy settings. The optimal settings of this bias voltage give a large energy transmission window. The positive voltage applied to the MCP plate creates a significant potential difference between the MCP front and the drift tube, thereby generating an acceleration that enhances the collection efficiency of electrons.

However, a fixed voltage setting on the lenses doesn't work for the expected energy range, which spans several hundred eV. The empirical setting of voltage used here is the linear increase of voltage from the lens 1 section to the drift tube from 66 % to 100 % of the total retardation applied. These values were taken from past studies and experimental validations.

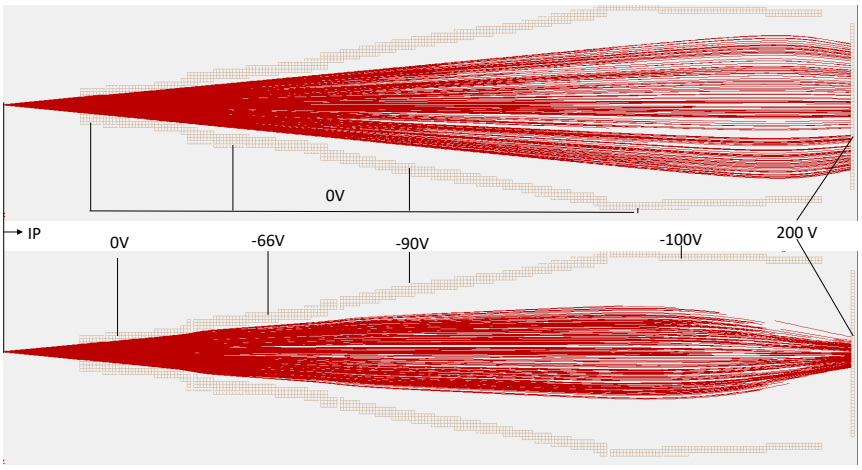

Figure 3.5: Electron trajectories simulated using SIMION. Electrons with a kinetic energy of 150 eV are used to fly through the spectrometers with two different sets of applied voltage on the retardation sections. The top electron trajectory results from no applied voltage; the bottom trajectory is the focused one with a voltage of -100 V. The MCP front is connected to a positive 200 V in both cases.

The electron trajectory becomes more focused with the applied voltage, thus enabling higher transmission.

3.4.1 Transmission characterization with the FEL beam pointing

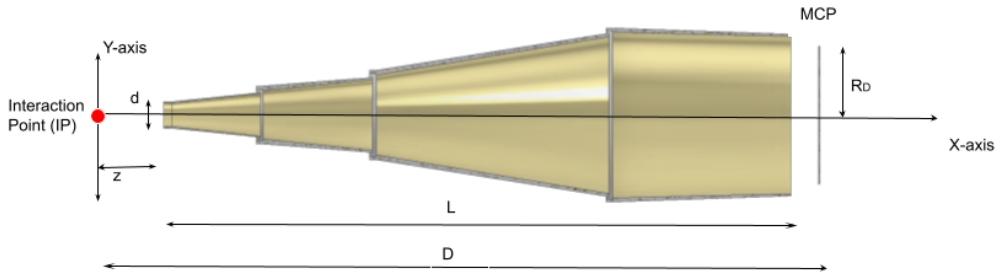

Figure 3.6: Schematic of the dimensions of the TOF spectrometer. Detailed descriptions of each dimension can be provided in the table below.

One of the critical performance parameters influencing the TOF spectroscopy is transmission. Several experimental conditions impact the overall transmission efficiency of the spectrometer. Among these, the two fundamental factors are the applied voltage in the retardation sections and the solid acceptance angle of the spectrometer. This section primarily examines how transmission varies under different beam propagation conditions. Even minor misalignments in the experimental setup can significantly affect the transmission efficiency.

The experimental setup discussed here is designed explicitly for angular streaking to characterize FEL pulses. In this configuration, the focus points of the FEL and the streaking laser play an important role. Both the FEL and the streaking laser pulses must be precisely focused at the interaction region. Any misalignment of the two beams can degrade signal quality in streaking and other photoelectron studies. In the case of streaking, such misalignments can result in a non-overlapping condition, effectively preventing streaking from occurring. This spatial shift in the interaction point can further reduce the overall transmission along the spectrometer.

This study investigates and tests four alignment scenarios to assess the degree of precision required during the experimental campaign to optimize performance.

The analysis is done with the SIMION software. The CAD model of the spectrometer is imported into SIMION, where a set of electrons is generated with properties similar to the targeted photoelectron from the experiment. The model used in the SIMION simulation is shown in Figure 3.6. The dimensions of the spectrometer model can be demonstrated as follows,

Schematic Dimension	**Value in mm**
Distance between the Interaction point (IP) and Tip of the spectrometer	z = 12
Diameter of the tip of the spectrometer	d = 4.2
Total length of spectrometer	L = 119
Distance from IP to MCP	D = 130
The radius of the active area of MCP	R_D = 13

This analysis primarily aimed to investigate the total collection efficiency of photoelectrons as a function of the FEL beam shift, which is achieved in SIMION by adjusting the position of the photoelectron source. In SIMION, the earlier cases were studied with an electrode resolution of 0.5 mm per grid unit (finer grid size demands more computational time). Electrons with a kinetic energy of 100 eV are generated and used to fly along the e-TOF spectrometer. A representation with an area similar to that of the MCP plate is also included in the simulation, positioned 5 mm away from the final drift tube section. A point source at (0, 0, 0) with a cone direction distribution and a half-angle of 5.7° is used for the systematic analysis. The geometrical acceptance of the detector with a radius of R_D at a distance D away from the source point is,

$$\theta = tan^{-}1(R_D/D) = 5.7^{\circ} \tag{3.7}$$

The electron distribution's cone angle exactly matches the detector's geometrical acceptance. The transmission characterization for each of the following cases was studied systematically, assuming that the photon beam is propagating in the Z direction.

- Positive transverse pointing in Y-axis
- Negative transverse pointing in Y-axis
- Positive transverse pointing in X-axis
- Negative transverse pointing in X-axis

The software enables control over the point of generation of the electron bunches in terms of both electron energy and position. For simplicity of analysis, all simulations are performed with no voltage applied to the retardation section, but with 200 V applied to the MCP front, thereby providing a more accurate comparison in terms of overall collection efficiency. The transmission is calculated using a self-written Lua code in SIMION. The software enables the integration of codes to define discrete conditions, which include the dimensions of the spectrometer model. From Figure 3.6, the dimensional constraints of the TOF spectrometer are illustrated, highlighting its role in the accurate detection of photoelectrons. Electrons that complete the whole flight path and reach the active diameter of the MCP plate are considered detected. Based on the specified dimensions of each component, trajectories that terminate before the total flight length (130 mm) or are detected outside the active MCP diameter (26 mm) are excluded from the analysis. Only electrons that satisfy these criteria are counted as valid detections.

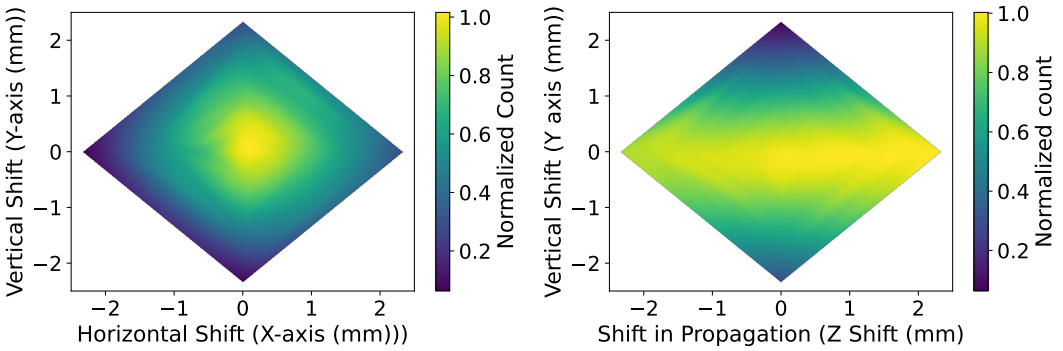

(a) (b)

Figure 3.7: Heat-map representation of the photoelectron collection efficiency as a function of beam shift. (a) Interpolated intensity map showing the total number of collected photoelectrons as the photon beam is displaced in the horizontal (X) and vertical (Y) directions perpendicular to the propagation axis. (b) Corresponding transmission map showing the collection efficiency as a function of vertical (Y-axis) and longitudinal (Z-axis) shifts relative to the propagation direction. The simulation was performed using 1000 electrons with a kinetic energy of 100 eV.

Figure 3.7 (a) displays the heatmap representation of the overall transmission with different sets of shifts in the source point of electrons, along with interpolated transmission for all other intermediate combinations of the beam drift. A clear decrease in the overall transmission is observed as the beam is shifted along both the X and Y axes. The collection efficiency was also evaluated by shifting the beam along the propagation (Z) direction while applying a

vertical displacement. This configuration shows no significant reduction in the total number of collected electrons in the propagation axis up to $\approx \pm 2$ mm. Since the behaviour is similar to 3.7 (b) when combining a longitudinal (Z-axis) shift with a horizontal (X-axis) shift, the corresponding figure is not included here.

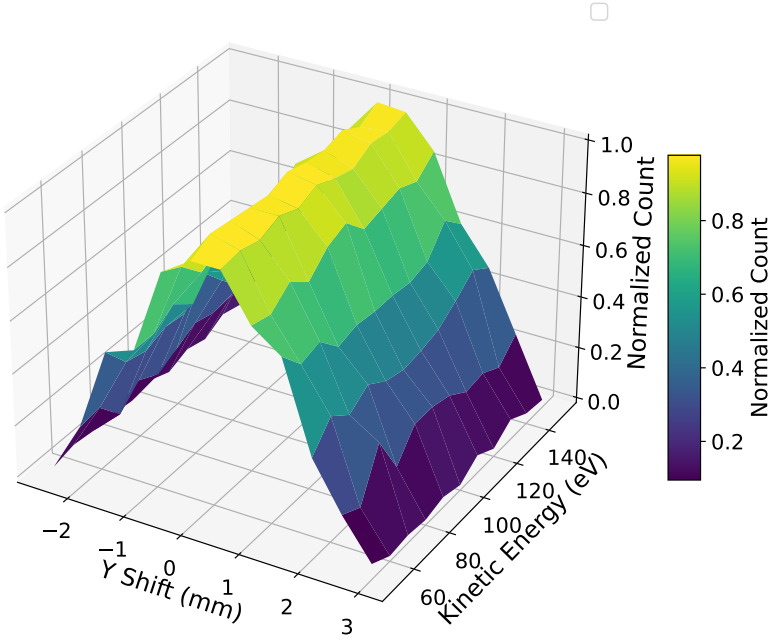

Figure 3.8: Kinetic energy dependent yield for beam shift in Y-axis. Electrons with a kinetic energy of 50 eV - 150 eV are used for the simulation.

This study emphasizes that the maximum beam shifting in the transverse direction to beam propagation that can yield a comparable signal strength is $\approx \pm 2$ mm.

For simplicity, the first set of simulations used constant kinetic energy. Since the transmission is energy-dependent, a set of simulations is performed over a kinetic energy range of 50–150 eV, reflecting the realistic spread of photoelectron energies produced in experiments due to ionization from different atomic shells, using the same source parameters with a shift in the transverse Y direction. This is selected as shifting in the transverse direction creates significant effects on total transmission. Figure 3.8 shows the transmission characteristics of a set of kinetic energies with the beam shifting in the Y direction. Notably, different transmissions are observed for various energies with the same source setting.

3.5 Voltage Divider Design for Detector

Figure 3.9 presents a schematic diagram of the detector section, illustrating the internal arrangement of components within the custom-built detector. The detector includes three MCPs arranged in a Z-stack configuration, housed within a PEEK cage. Signal readout is achieved through capacitive coupling using a circular anode connected to the outer CF-40 flange.

In this configuration, charge accumulation in the MCPs induces a current in the metallic anode, located at the base of the detector assembly. This current is then capacitively coupled to the anode, generating a signal referenced to ground [115]. The output signal is transmitted via an SMA connector, which links the anode to the digitizer. High voltage is supplied to the front and back of the MCPs through an external voltage divider circuit. A flat sheet resistor facilitates the connection between the HV_{in} pin and the MCP plates via the divider. An additional mesh is placed in front of the MCPs to shield against electrostatic field penetration.

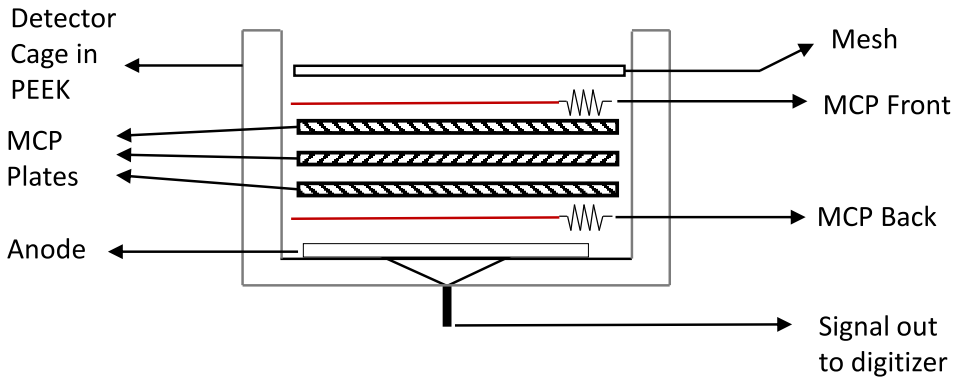

Figure 3.9: Cross-section view of the MCP-based detector. Individual MCP plates with a Z-stack configuration, followed by the metallic anode. The MCP front and back are connected to the external voltage divider.

The high-voltage supply is provided to the MCPs through a voltage-dividing scheme [116]. The voltage-dividing circuit is placed outside of a vacuum and connected electrically via the push-pull sub-d pin configuration. The voltage is divided into two parts, one connected to the MCP front and the other to the back of the MCP Plates. The voltage division is based on the MCP amplification scale from the data sheet of the individual MCP plates. The voltage is divided by a ratio of 20:80 between the front and back of the MCP, respectively. The new design was developed to incorporate surface-mounted device (SMD) components. This reduced the complexity of the PCB board, making the detector design more compatible and less crowded, which enabled easy inspection and exchange if necessary. The design was created to make replacing the electronic out-coupling very convenient, without affecting other detector parts in

the vacuum. The compact size of SMD components compared to conventional through-hole electrical components reduces component density and facilitates automated assembly options. These SMD components allow the individual elements to be distributed on both sides of the PCB, reducing crowding without compromising quality.

PCB design is developed using Eagle, a commercially available software program that allows users to select the footprints of the resistors and capacitors. Eagle offers a wide range of components in its online library, enabling users to choose different elements based on size and performance. Some of the significant constraints while designing the PCB are listed as follows;

- Fixed outer diameter of the PCB
- Providing the additional space for SMA and the out-of-vacuum periphery, including the M4 threaded pillar
- Positioning the output pins exactly matching the feedthrough flange pin orientation and spacing.
- Incorporating four retardation sections and one voltage divider within the available space

Apart from these, the trace line (the conducting connection lines between the components) should not have sharp edges, and a minimum distance should be maintained between them to avoid the arching effect when HV is applied. Proper trace spacing is crucial to prevent electromagnetic interference. The output of the sections in the PCB layout is connected to pins with a push-pull configuration, enabling the final connection between the PCB and the vacuum detector section.

Voltage division requires a combination of high and low values of resistors for R1 and R2 [116]. The output voltage across the R2 is;

$$V_{out} = \frac{R_2}{R_1 + R_2} \cdot V_{in} \tag{3.8}$$

The schematic diagrams of the electric circuits used for voltage division and the lens section are shown in Figures 3.10 and 3.11. A single PCB board contains one voltage divider and four sets of retardation sections. The value of resistors and capacitors was chosen from the previous design. The MCP front is at a lower voltage than the MCP back to enhance the avalanche effect. In Figure 3.10, V1 represents the voltage across the front, and V2 represents

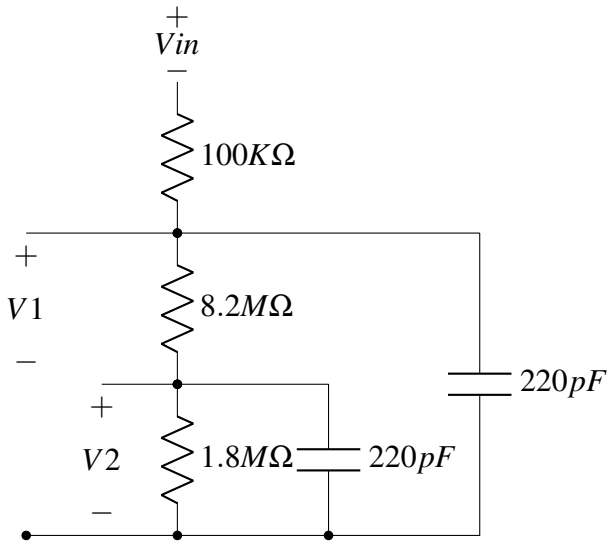

Figure 3.10: Schematic of voltage divider circuit for the MCP detector. V1 is the voltage applied to the MCP back, and V2 is the voltage applied to the MCP front. Vin is the high-voltage supply. The resistor value selection enables the voltage division in 20:80 across MCP front and back.

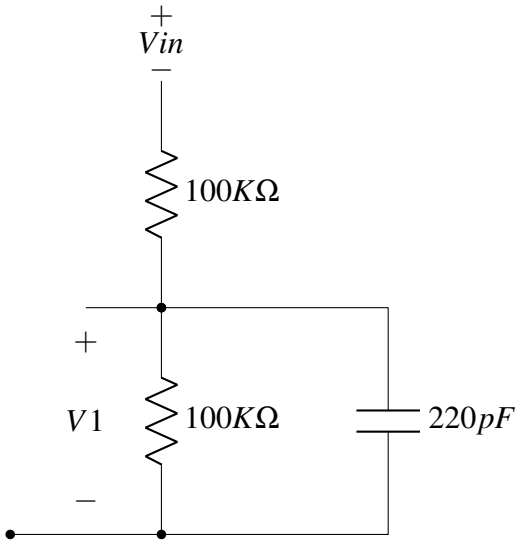

Figure 3.11: Schematic of an electrical circuit for the individual retardation section. All four sections have the same resistor and capacitor combination, but the Vin is different for each section.

the voltage across the back, where a single HV is divided between the resistor sections and connected to the corresponding detector sections.

As mentioned earlier, the solution to the constraints is to opt for a double-layer design where the resistors and the input and output pins are incorporated into the top side of the PCB. In contrast, capacitors with a comparatively large footprint are placed on the bottom side of the PCB. This design enables the selection of the right capacitor and resistor combination without any problem regarding space distribution and electrical connection. Proper care is taken while designing to avoid sharp trace edges and maintain the trace spacing. The software provides a tool to facilitate checking all the errors. Figure 3.12 shows the PCB board design created in Eagle software, which includes one voltage divider and four independent retardation sections.

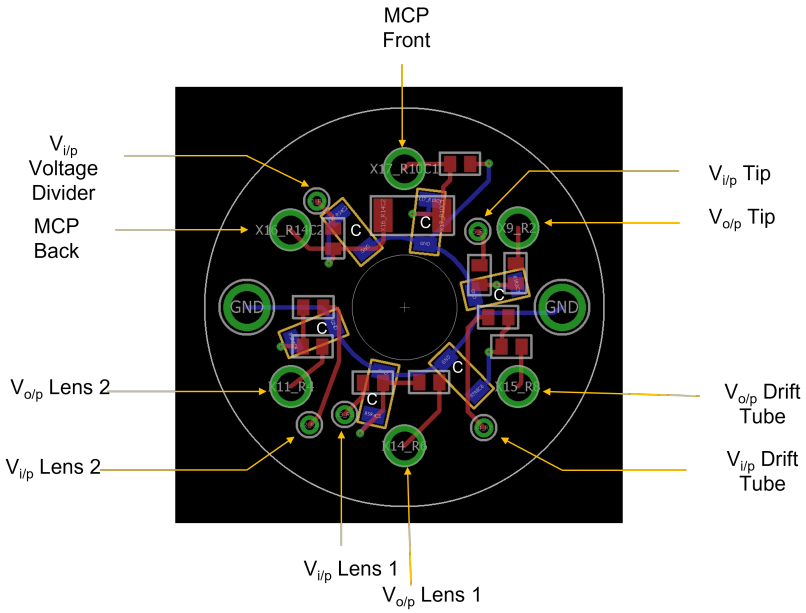

Figure 3.12: PCB board diagram with the voltage divider and the four independent retardation section RC circuits.

3.6 Spectrometer Commissioning

The complete experimental setup, including all the 16 e-TOFs and a dedicated target gas delivery system, is being tested at the Free Electron Laser in Hamburg (FLASH) [65]. The facility has two undulator lines, FLASH 1 and FLASH 2. The commissioning was carried out at the FL21 beamline of FLASH 2 [66], which provides photon energies ranging from 14 eV to 376 eV and pulse durations between 10 fs and 200 fs, conditions suitable for characterizing of the e-TOF spectrometers. The commissioning was conducted with a chamber pressure of 1.5×10^{-7} mbar with regulated neon gas flow. Before initiating the experiment with the FEL beam, each e-TOF spectrometer was tested and verified by monitoring the MCP dark counts.

The beam, with a photon energy of 45.8 eV, was used to generate photoelectrons from neon. Neon was selected as the target gas due to its high photoionization cross-section at the available photon energy range of the beamline; it will also serve as the gas of interest in future experiments with this setup. Figure 3.13 compares the cross-sections of argon 3p (in green), argon 3s (in red), and neon 2p (in blue) for a photon energy range from 20 eV to 200 eV. The photoionization cross-section of the neon 2p state is 8.606 Megabarns, whereas the cross-sections of other potential target gases at this photon energy are below 1 Megabarn. Their significantly lower cross-sections at the available photon energy ruled out these alternatives as viable targets. The photon energy was limited because the commissioning had to be performed non-invasively in parallel with another experiment.

3.6.1 Photoelectron spectra of the neon valence electrons

Some of the primary goals of the commissioning were to characterize the transmission, find the optimal voltage setting for the detectors, and also check the feasibility of the retardation sections. The photon energy was good enough to ionize the neon 2p shell with a kinetic energy of ≈ 24 eV.

Figure 3.14 shows the photoelectron spectra of 16 e-TOFs with individually selected operating voltages for the detectors. The detector current is fed to an analog-to-digital converter (ADC) to create the analog traces, which are separated in time. The detector time response is verified to 1 ns FWHM for all the individual detectors, enabling the energy resolution for the fast electrons. Since the photon energy range available at the FL21 beamline during commissioning only enabled single ionization, only a single peak corresponding to the neon 2p is observed in the trace.

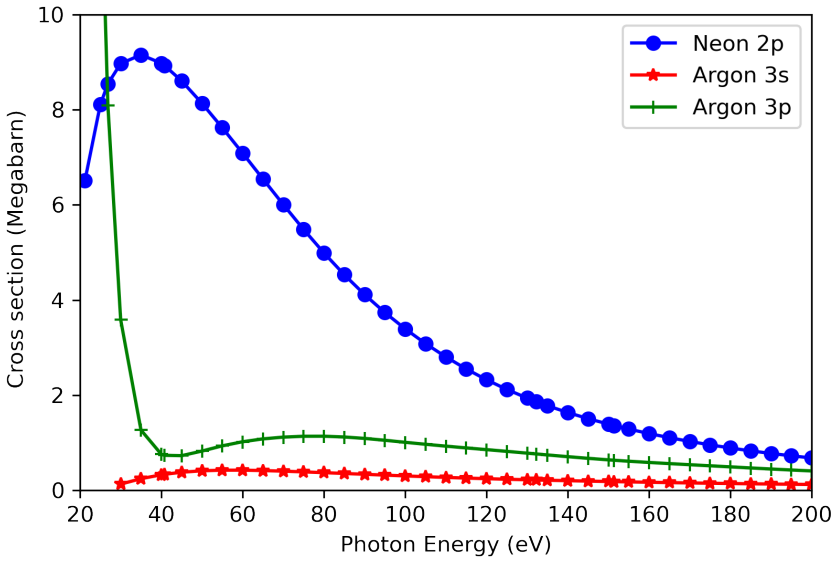

Figure 3.13: Photoionization cross-section of neon and argon valence electrons for a 20 eV to 200 eV photon energy range. Data taken from [117].

3.6.2 Photon energy scan

Accurate transmission calibration of each TOF spectrometer is crucial, as even spectrometers with identical mechanical design and construction can exhibit subtle variations in overall performance. Such calibration is essential for characterizing the kinetic energy–dependent transmission, which is particularly important for experiments requiring access to electrons with very low kinetic energy. Ensuring proper transmission calibration directly impacts the quality and reliability of angle-resolved measurements.

In addition, conversion from TOF to kinetic energy is fundamental for interpreting the acquired spectra. This is typically achieved through photon energy scans, where the TOF response is compared with known kinetic energy values from the literature for a range of incident photon energies. From this comparison, a time-to-energy calibration function is derived, enabling accurate mapping of TOF spectra into the corresponding kinetic energy domain. Figure 3.15 shows the photoelectron spectra of neon measured at five different photon energies, with 5 eV intervals spanning the range of 30 eV to 50 eV. Each spectrum is an average of 1000 single-shot spectra acquired under identical conditions. No retardation was applied in the flight tube sections. The spectra exhibit a single prominent peak, corresponding to the ne 2p photoline.

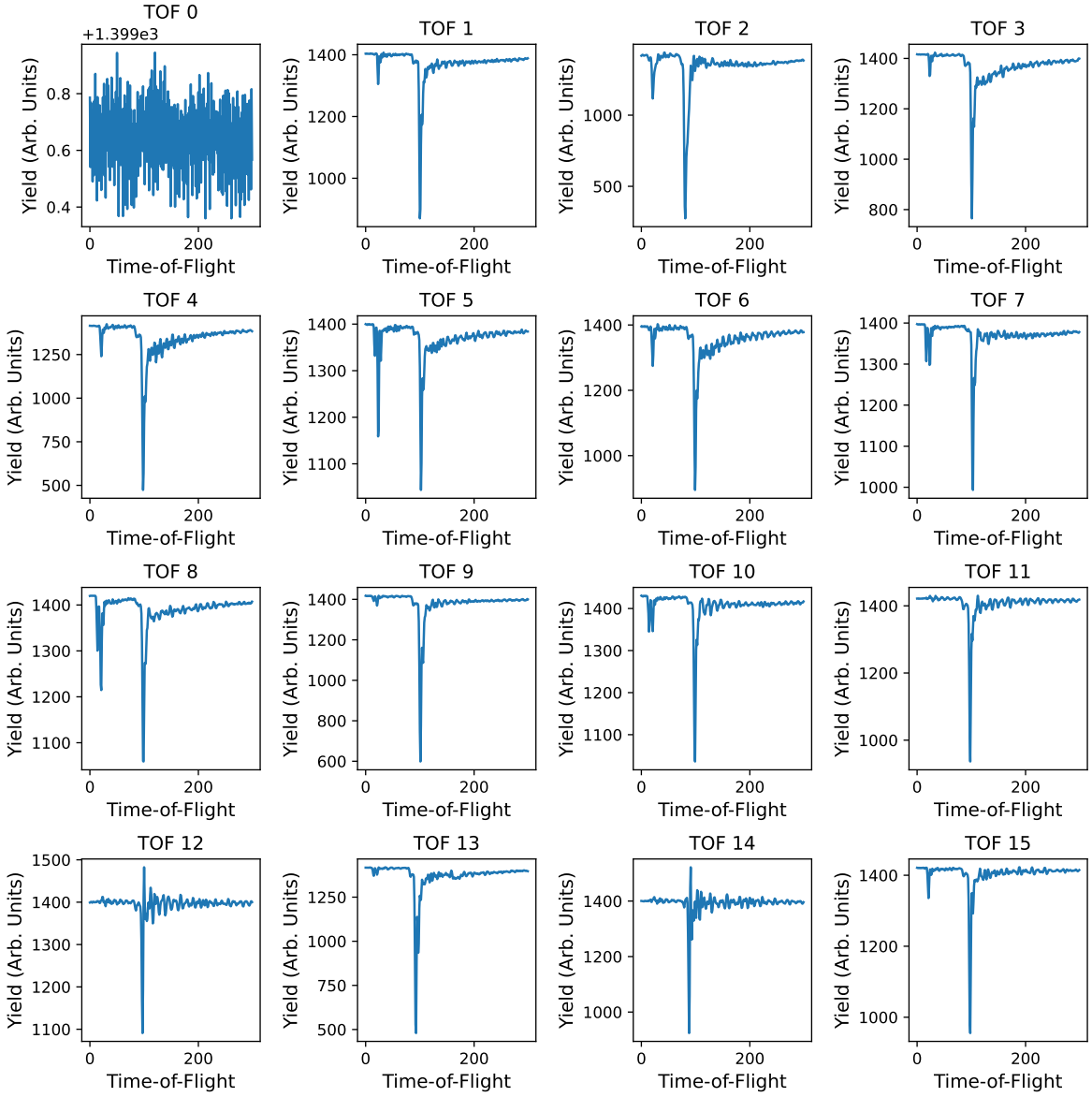

Figure 3.14: Time-of-flight spectra recorded from the 16 individual TOF spectrometers. The yield of the photoelectron signal from the neon 2p line is plotted as a function of TOF at a photon energy of 45.8 eV, with no retardation voltage applied. One of the spectrometers, labeled TOF 0, was not connected to the data acquisition due to the limitations at the experimental station; this detector was oriented vertically downward and is shown for completeness.

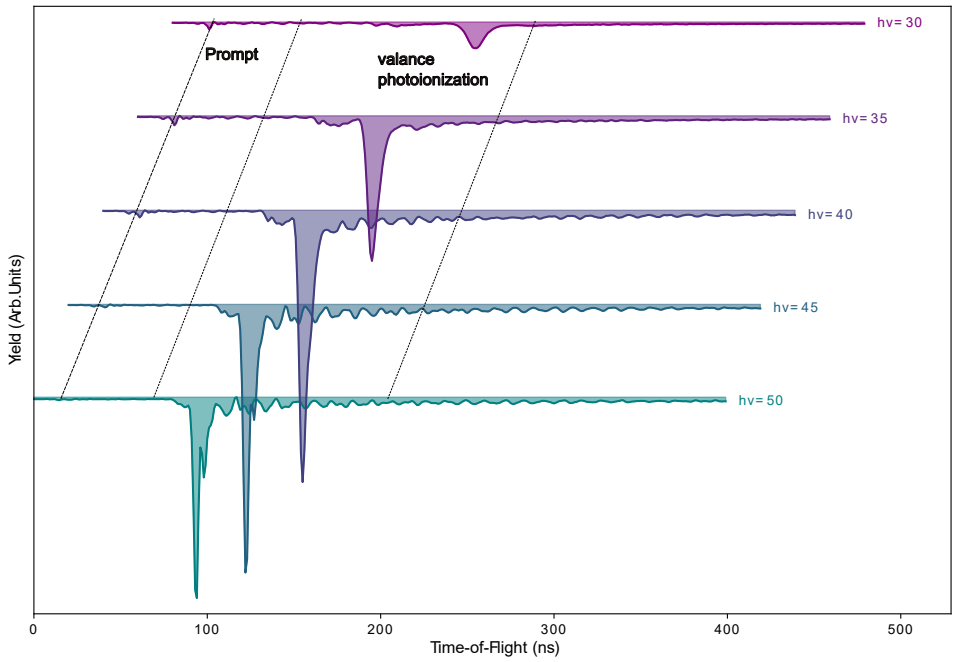

Figure 3.15: Photoelectron spectra of neon obtained at 5 different photon energies (5 eV intervals) from 30 eV - 50 eV. Each spectrum is an average of 1000 single-shot spectra. No applied retardation voltage is provided to the lens sections.

As expected, the peak position on the TOF axis shifts with photon energy due to changes in the photoelectron kinetic energy. Additionally, the peak intensity varies with photon energy. Notably, the signal corresponding to the lowest photon energy (30 eV) is significantly weaker. This is primarily attributed to the reduced transmission efficiency for low-energy electrons.

At lower kinetic energies (e.g.,$\approx$ 8 eV for the 30 eV photon energy), electrons are more susceptible to any residual magnetic fields and may have larger angular spreads in their trajectories [118]. The deflection or the spread of the electron trajectory with an energy of E after travelling a distance of L in a magnetic field component B perpendicular to the trajectory is,

$$deflection = \frac{eB}{2} \times \frac{L^2}{\sqrt{2Em}} \tag{3.9}$$

According to the deflection relation deflection $\propto 1/\sqrt{E}$ given in Equation 3.9, electrons with lower kinetic energy experience a greater deviation in the magnetic field compared to those with higher kinetic energy [118]. In the absence of magnetic or electrostatic field compensation, these low-energy electrons are more likely to deviate from the spectrometer axis and miss the detector. This collectively leads to a suppression of the detected intensity at lower photon energies, despite similar ionization cross-sections.

3.6.3 Transmission characterization with multiple retardation settings

To test the proper functioning of the retarding lenses, measurements were recorded with different voltage settings on the lens sections. The photon energy was set to 45.8 eV with a pulse energy of 6 μJ, and the beamline settings were kept constant during the measurements. The expected photoline is the 2p photoionization of neon at 24 eV. Figure 3.16 shows the stacked TOF spectra on top of each other corresponding to the different voltages applied to the retarding sections. A significant delay of the TOF corresponding to the applied voltage is visible in the spectrum. All the individual plots correspond to the average of 1000 shot spectra. The voltage division to the multiple sections is provided in constant proportions, as shown in the following table.

Section	set 1(V)	set 2 (V)	Set 3(V)	Set 4 (V)	Set 5 (V)
Tip	0	0	0	0	0
Lens 1	-3.3	-6.6	-9.9	-13.2	-16.5
Lens 2	-4.5	-9	-13.5	-18	-22.5
Drift Tube	-5	-10	-15	-20	-25
MCP Front	+200	+200	+200	+200	+200

Table 3.1: Comparison of the different retardation values applied to the multiple sections of e-TOF spectrometer.

The tip of the spectrometer and the MCP front are kept constant at 0 and +200 V, respectively, throughout the measurements. The voltage ratio for a particular final retardation follows the format 0%, 66%,90%, and finally 100% from tip to drift tube. A resolved peak of neon 2p is observable up to maximum retardation of -20V. Kinetic energies below 5 eV are not captured in this case due to the lack of proper magnetic field shielding. The application of different retardation voltages in the TOF spectrometer directly influences the resolution and the shape of the photolines by decelerating the electrons in the drift section (E' = E-V), with a retardation voltage of V, the flight time increases nonlinearly because of the quadratic relationship between time and energy. This can create a better separation of the spectral features in the temporal axis for low kinetic energy electrons. The longer flight time, in turn, increases the energy resolution. However, higher retardation also introduce broadening of the feature due to the reduced transmission due to the high sensitivity to the inhomogeneous field. It is clear in Figure 3.16 that the low energy electron peak is more stretched compared to the faster electrons and weaker structures such as the second peak coming after dominant peak in fast

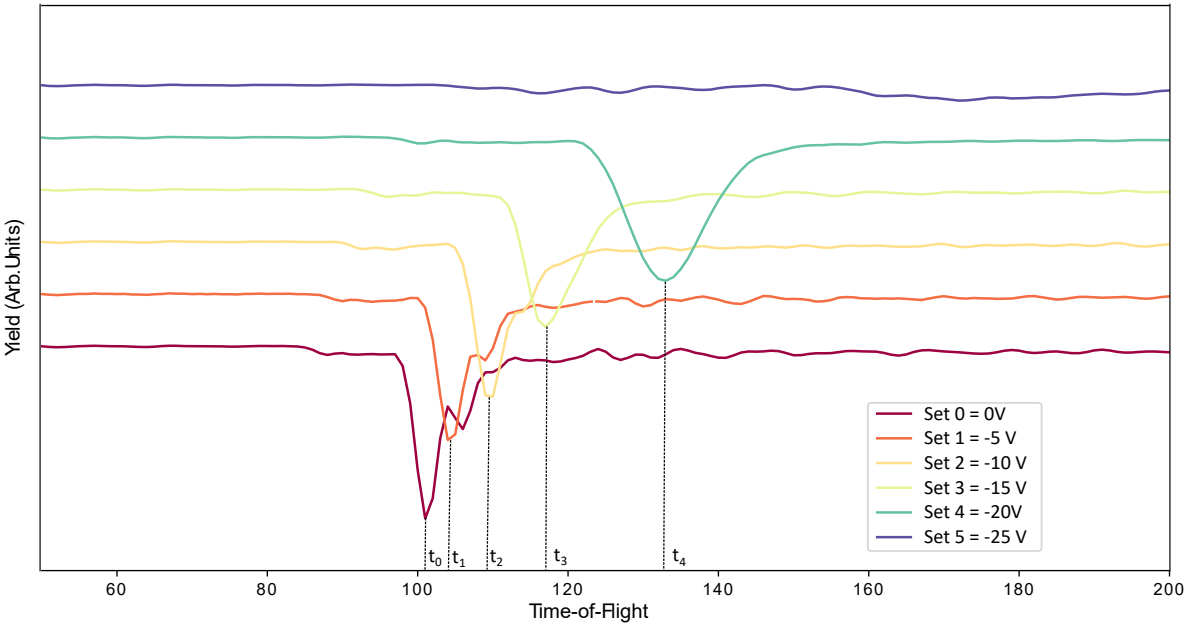

Figure 3.16: Time-of-flight spectrum of neon 2p peaks with different applied retardation. Each spectrum is an average of 1000 single-shot spectra. The different flight times for the same feature with the external voltage are marked as t_0,t_1,t_2,t_3 and t_4, where the arrival time corresponds to no applied voltage.

electrons are lost at high retardation. Although the baseline may appear to shift between the traces, this is not a physical change in the signal. A vertical offset was intentionally applied in the plotting for visual clarity, in order to separate the spectra and avoid overlap. The original baseline remains unchanged, and this offset does not affect the analysis or extraction of the peak positions or widths.

The spectrometer was successfully commissioned at the FLASH facility. Functionalities such as gas delivery to the chamber, working of individual e-TOFs, and data recording were appropriately checked. No scientific study has been conducted out at this stage other than the basic functionality checks. However, the chamber is entirely occupied, tested, and installed for the pulse characterization at XFEL. Figure 3.17 shows the image of the spectrometer with all the individual spectrometers installed around the central interaction point.

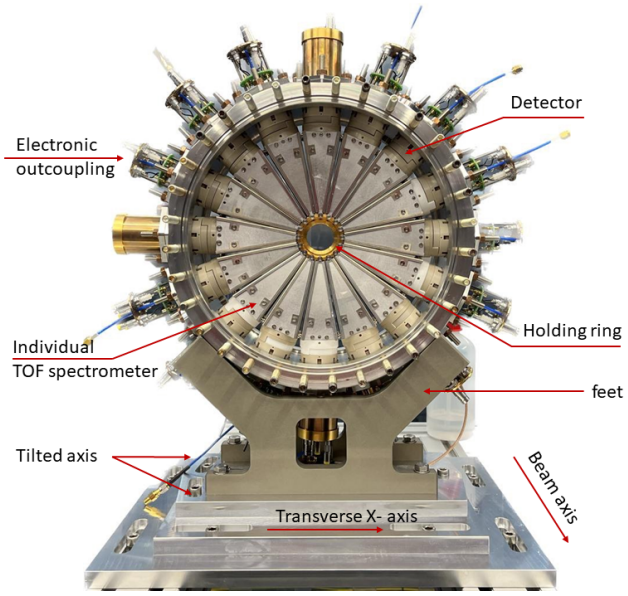

Figure 3.17: The angle-resolved spectrometer setup. An image with the side flange open enables the view of the 16 TOF spectrometer arrangement. All of the TOFs are held in place using the centre holding ring. The chamber has feet placed on the flat base, allowing movement in both X and Y directions for alignment (marked with arrows).

Chapter 4

Experiments at Free-Electron Lasers

4.1 FEL Pulse Characterization Using Angular Streaking

Attosecond science based on high-harmonic generation (HHG) from optical lasers has revolutionized our understanding of fundamental quantum-mechanical dynamics [119], unlocking previously inaccessible insights into electron and nuclear motion. This approach has enabled control and measurement of phenomena such as atomic electron tunneling [120], photoemission delays [121], and proton dynamics in molecules [122]. Furthermore, it has provided new ways to explore the charge migration in atoms and molecules [123] and even light-field-controlled reversible phase transitions in dielectrics [124].

In parallel, the development of ultrabright XFEL facilities has opened a new era of high-intensity X-ray experiments, advancing research in the physical, chemical, and material sciences [111]. XFEL sources generate X-rays through the SASE process of relativistic electrons in an undulator's magnetic field. This process generates intense, ultrashort bursts of X-rays, with energies up to tens of millijoules, wavelengths down to the Ångstrom level, and photon counts reaching around 10^{33} photons per second within the 0.5 keV to 8 keV energy range. XFELs, therefore, extend the capabilities of ultrafast science into the X-ray regime, complementing the advancements made by HHG sources [125]. The study of ultrafast electron dynamics in atoms and molecules, charge transfer mechanisms and the site-specific X-ray pump-probe studies require very short and intense pulses with femtosecond or sub-femtosecond resolution. Many XFELs are capable of generating sub-femtosecond to attosecond pulses, which meet this criterion [126–131]. The photon flux generated by the XFEL is typically higher than that of HHG sources.

Although XFEL pulses are highly intense and tunable, enabling access to the nonlinear

regime, SASE pulses in particular exhibit a stochastic pulse nature, unlike seeded pulses, which are more stable. Despite being generated with the same settings, each SASE pulse differs in both the spectral and temporal domains. This variability makes it essential to diagnose these pulses in a single-shot scheme. Several methods are available to characterize the duration of X-ray pulses, such as measuring the electron bunch length and using time-resolved electron beam energy and energy spread measurements with a transverse radio-frequency deflector after the undulator [132]. However, these techniques probe the electron phase space after lasing and thus provide only indirect information about the X-ray pulse duration.

4.1.1 Photoelectron streaking methodology for FEL pulse characterization

The FEL pulse duration can be diagnosed using the near-infrared (NIR) streaking technique, which enables temporal characterisation [133–135]. In this method, the FEL pulse is spatially and temporally overlapped with an NIR optical laser pulse. When the FEL pulse ionizes a target gas inside a vacuum chamber, the emitted photoelectrons interact with the overlapped NIR laser pulse, which shifts their energy. The streaked photoelectrons are then detected using an angle-resolved spectrometer. By analyzing the temporal structure of the photoelectrons, valuable insights into the FEL pulse duration can be obtained. This is a non-invasive approach for diagnosing ultrafast FEL pulses with easily adjustable temporal resolution based on the wavelength of the streaking laser.

Figure 4.1 shows the concept and working principle of streaking. Photoelectron spectra generated in the presence of the streaking laser field are referred to as dressed spectra. The characteristics of these spectra vary depending on the period of the streaking laser field (t) and the FEL pulse duration (τ) being diagnosed. Based on this relationship, two distinct cases of dressed spectra can be identified: one where $t > \tau$ and another where $t < \tau$.

When the period of the streaking field (t) is shorter than the FEL pulse duration (τ), the resulting interaction gives rise to sidebands, leading to what is known as the sideband regime. In this regime, two sidebands appear symmetrically around the original undressed spectra. This shift or spread in energy corresponds to the optical frequency of the streaking laser field. In this case, the photoelectrons are subjected to interact with multiple dressing fields [14, 133, 134, 136].

When the period of the streaking field (t) is longer than the FEL pulse duration (τ), the photoelectron distribution exhibits a redistribution or shift of the spectrum compared to the unstreaked original spectrum. Measurements in this interaction defines the streaking regime,

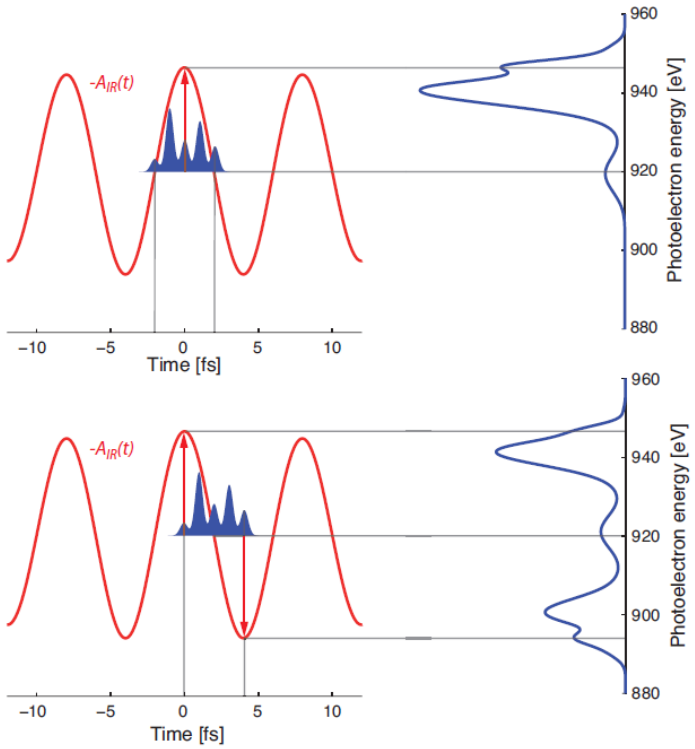

Figure 4.1: Concept of photoelectron streaking. Ilustration of the interaction between the FEL pulse (blue filled shape) and the vector potential of the streaking field (A_{IR}, red oscillating curve). The top panel shows the scenario where the FEL pulse overlaps with the maximum or minimum of the vector potential, resulting in a shift of the photoelectron spectrum to higher or lower energies relative to the unstreaked central energy. The bottom panel illustrates the case when the FEL pulse overlaps with the zero-crossing of A_{IR}, causing the photoelectron spectrum to broaden symmetrically around the central energy. Image taken from [14].

where the FEL pulse is relatively short in duration and, therefore, experiences varying magnitudes of the dressing pulse's electric field depending on the time of interaction. The extent of the photoelectron energy spread (Δe) depends on this interaction. The overall shift $\Delta\varepsilon_t$ in the photoelectron spectra can be described by the following equation [14, 134, 137].

$$\Delta\varepsilon_t \approx -p_c A_{IR}(t) \tag{4.1}$$

where $A_{IR}(t)$ is the vector potential of the dressing field at the time of the electron generation and p_c is the momentum corresponding to unstreaked original spectrum with a central energy of e_c. The estimated upper limit of the pulse length will be,

$$\tau_{X-ray} = \frac{\delta_s}{\Delta\varepsilon} * \frac{t}{4} \tag{4.2}$$

where δ_s is the width of the streaked spectrum and Δe is the maximum energy shift of the streaked spectrum from the central unstreaked photoline [14, 133].

4.1.2 Angular streaking

Precise characterization of pulse duration is crucial for experiments in which peak intensity plays a significant role. With the advancement of attosecond X-ray pulse generation, the field of attosecond nonlinear physics is rapidly emerging. These developments demand temporal reconstruction of XFEL pulses with high temporal resolution and accuracy. An equally important requirement is single-shot characterization, which allows retrieval of the stochastic intensity distribution of XFEL pulses without the need for averaging over multiple shots. Achieving both sub-femtosecond temporal resolution and arrival-time jitter measurement in a single diagnostic scheme remains highly ambitious, particularly when using linear streaking techniques.

A promising solution to this challenge is angular streaking, where photoelectrons are streaked using a circularly polarized laser field. While conceptually similar to linear streaking, angular streaking introduces an energy modulation that depends on the emission angle. This is accomplished through the combination of a circularly polarized optical laser and an angle-resolving TOF spectrometer setup, enabling simultaneous access to energy (via TOF) and directional information of the photoelectrons [111]. The vector potential of the streaking laser field rotates like the hand of a clock, and this periodic motion imprints the temporal structure of the X-ray pulse onto the angle-resolved photoelectron spectrum. Figure 4.2 shows a schematic representation of angular streaking. Every other X-ray pulse is overlapped with

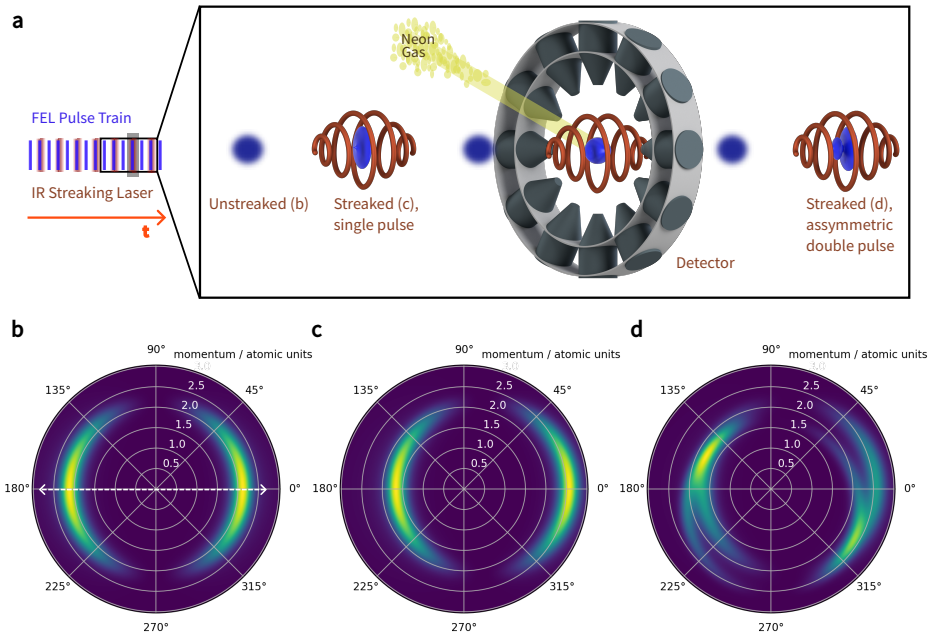

Figure 4.2: a) Schematic overview of the angular streaking experiment. Every other shot in a train is overlapped with the streaking laser; the FEL pulse is shown as the blue dot, and the red spherical envelope indicates the streaking laser field. (b)-(d) Shows the three simulated neon 1s spectra in the polarization plane, (b) unstreaked shot (no momentum shift), the white dotted line shows the polarization direction of the incoming X-ray pulse, (c) streaked shot with a momentum shift towards the right, (d) streaked spectrum of a double pulse. Image taken from [88].

the circularly polarized streaking laser, and the angle-resolved spectra are captured using a TOF setup as shown in figure 4.2 (a), (b),(c), and (d) show the simulated neon 1s spectra in the polarization plane corresponding to unstreaked, streaked, and streaked spectra of a double spike pulse respectively. By adjusting the wavelength of the streaking laser, the period of the streaking field can be varied, thereby tuning the temporal resolution of the measurement. This technique is capable of characterizing ultrashort pulses with a temporal resolution of few femtosecond, as demonstrated by P. Hartmann et al. at LCLS [111]. Isolated attosecond pulses with a FWHM of less than 300 as were characterized using a velocity map imaging (VMI) spectrometer in combination with a 1300 nm circularly polarized optical laser at LCLS [138]. Furthermore, with appropriate selection of the streaking field period, angular streaking can also be used to characterize longer pulses.

In ultrafast spectroscopy, particularly for attosecond or femtosecond pulse characterization, both linear and angular streaking techniques are used to extract temporal information from photoelectron emission. However, in linear streaking, the final electron energy depends on both the emission time and the streaking field amplitude, which, in the absence of phase stability between the fields, makes time-to-energy mapping non-unique and necessitates precise calibration of the streaking field. In contrast, angular streaking uses a circularly polarized streaking field, resulting in an angle-dependent energy modulation that provides a one-to-one mapping between ionization time and energy modulation. Moreover, angular streaking enables single-shot measurements, as different emission angles naturally map to different ionization times, whereas linear streaking often requires averaging over many pulses. With its rotating electric field acting like a clock hand, angular streaking offers sub-cycle resolution, making it especially effective for capturing the full temporal profile of complex ultrashort pulses. For these reasons, angular streaking is generally preferred for the measurements of pulse duration and structure at XFELs [133, 139].

4.1.3 Attosecond-resolution temporal diagnostics at the European XFEL

The angle-resolving TOF spectrometer assembly, consisting of 16 individual TOFs, as shown in Figure 4.3, is deployed at the SASE3 beamline of the Eu-XFEL for the measurements. The detector array is arranged in a plane perpendicular to the direction of propagation of the X-ray beam. A circularly polarized mid-infrared (MIR) optical laser with a wavelength of 4.75 μm is used as the streaking field. Both the X-ray and MIR laser beams are spatially and temporally overlapped and focused into the interaction region inside the vacuum chamber.

This overlap is achieved using a sample paddle, a flat surface with multiple sample-

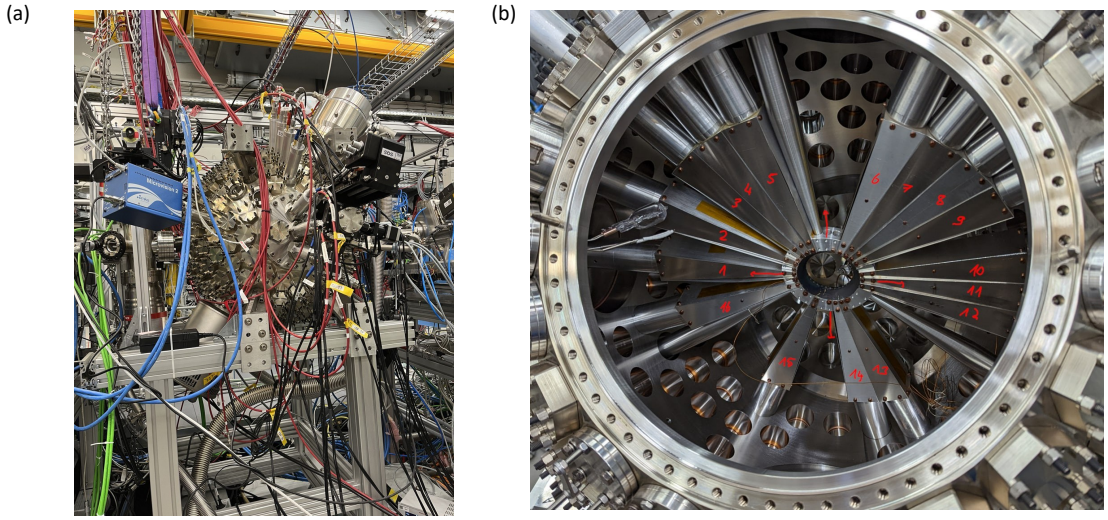

Figure 4.3: (a) Photograph of the angle-resolving TOF spectrometer assembly installed at the SASE3 beamline. (b) View of the detector array mounted inside the vacuum chamber, showing the arrangement of the individual TOF spectrometers.

holding sections, which is introduced perpendicular to the beam path. The paddle serves as a tool for aligning the X-ray and streaking beams with high precision. Additional details on the instrumentation and alignment procedures are provided in Section 5.3. The experimental chamber used is shown in Figure 4.3 where the fully installed spectrometer in the beam line is shown in (a), and the side flange opened view of the spectrometer with detectors marked is shown in (b).

Neon gas is used as the target and is ionized by the linearly polarized X-ray beam. X-ray pulses with a photon energy of 990 eV ionize the core-shell electrons, producing photoelectrons with an initial kinetic energy of approximately 120 eV. All resulting photoelectrons are streaked in both energy and momentum by the circularly polarized laser field, with the analysis focusing on those emitted from the 1s core level. Further reduction of the kinetic energy can be achieved by applying an external retardation voltage, allowing for enhanced energy resolution and more accurate spectral reconstruction.

In this method for reconstructing the temporal profile of SASE X-ray pulses using streaking, a simulated basis is created by modeling how electrons would be streaked under different time delays and streaking field strengths (kicks). Each basis entry represents an angle-resolved electron spectrum generated by an X-ray pulse interacting with a streaking laser at

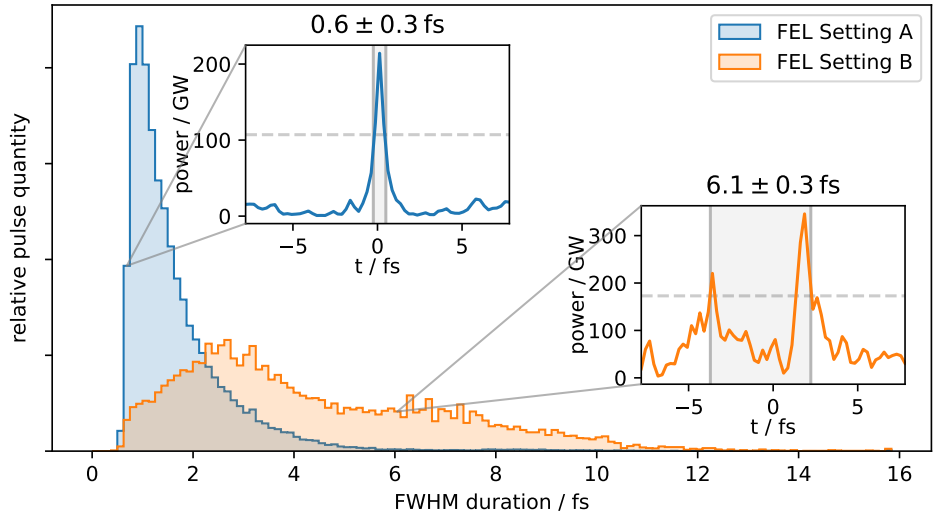

Figure 4.4: Reconstructed XFEL pulse duration (FWHM) for two different machine operation modes. Image taken from [88].

a specific phase. The measured photoelectron spectrum is then compared to these simulated entries, and an iterative algorithm selects and combines the best-matching components. The kick value is fixed early on to reduce complexity, and the final result is a spectro-temporal vector that, after convolution with a Gaussian filter (to account for time – energy uncertainty), reveals the time-dependent intensity or spectrogram of the X-ray pulse [88].

This scheme provides the temporal duration of the X-ray beam on a single-shot scale. Figure 5.6 shows the distribution of the pulse duration estimated from the reconstruction method for two different machine operation settings. The histogram distribution in setting A shows a significant number of shots with a duration of less than 1 fs. The comparatively longer pulse mode (setting B) is used for comparison. Ongoing developments aim to incorporate machine learning algorithms into the reconstruction workflow, allowing for real-time, single-shot pulse duration diagnostics. Such capabilities will significantly enhance user operations at XFEL facilities by providing online feedback on pulse properties for precise experimental control and optimization [140].

4.2 Polarization Diagnostics at FLASH

Polarization, a fundamental property of electromagnetic radiation, describes the orientation of the electric field vector as the wave propagates. In the context of FELs, the ability to control polarization is critical for a wide range of applications, including magnetic dichroism studies [141], chiral spectroscopy [54, 142], and ultrafast dynamics in anisotropic systems [143]. Despite the significant advancements in FEL facilities worldwide, there remains a strong interest in enhancing their capabilities, particularly in generating ultrashort pulses and achieving precise polarization control [144]. Standard undulator configurations, as discussed in Section 2.4, typically produce linearly polarized light. However, modifying the orientation or sequencing of linear undulators enables the generation of diverse polarization states.

One widely adopted approach involves the use of an afterburner undulator a second undulator stage with a different polarization orientation than the first, which can tailor the output polarization [145] [146]. Various polarization control schemes have been implemented at major FEL facilities. For example, the Delta undulator at LCLS achieves strong polarization control by preconditioning the electron beam for efficient afterburner operation [147]. The APPLE-II undulator, capable of producing linear, elliptical, or circular polarization, is used both as a main radiator and an afterburner at multiple sites [148] [149]. Notably, FERMI is the only seeded FEL that offers variable polarization using APPLE-II undulators [112]. APPLE-X undulators are being commissioned at the European XFEL, while FLASH 2 employs APPLE-III undulators to generate polarization-controlled photons [150] [151]. A comprehensive overview of APPLE-type undulators can be found in [152].

This section presents the first polarization measurements conducted during the commissioning of the afterburner undulator at FLASH 2, offering valuable insight into the beam's polarization characteristics under experimental conditions.

4.2.1 Beamline and experimental setup

The experimental setup used for the characterization of the polarization of incoming X-ray beams is explained in this section. An angle-resolving e-TOF spectrometer is used for the diagnostics. The spectrometer consists of similar but independently working 16 individual e-TOFs. Each e-TOF is 310 mm long with three independent retardation sections. These sections decelerate and focus the fast-moving electrons, thus enabling better energy resolution.

The e-TOFs are arranged in a plane perpendicular to the plane of X-ray beam propagation. This setup can measure the angular distribution of the photoelectrons when ionized by the

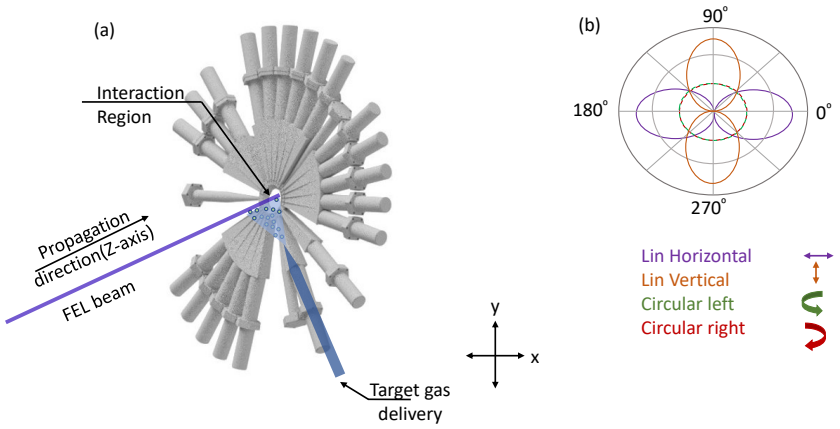

Figure 4.5: (a) Schematic illustration of the experimental setup showing the incoming X-ray beam and the arrangement of the angle-resolving TOF spectrometers. The spectrometers record the TOF spectra resulting from photoionization events induced by X-ray pulses with varying polarization states. (b) Schematic of polar plot of the photoelectron signal intensities recorded by TOF spectrometers, illustrating the angular distribution patterns corresponding to different polarization settings of the X-ray beam.

photon beam. An effusive gas inlet system is provided with the setup to successfully introduce the target gases into the centre of the chamber or to the interaction point where the FEL beam ionises the target gas. The angular distribution retrieved by the spectrometers of a particular atomic orbital can provide information about the polarization state of the ionizing beam [112].

Figure 4.5 shows the schematic of the experimental setup used for the measurements. The experimental setup is realised at the FL21 beamline at FLASH 2. The spherical vacuum chamber can include 22 e-TOFs in the dipole plane. However, due to the limited digitizer channels, only 16 were used at a time [153]. The target gas is selected based on the experimental conditions, such as photon energy and the photoionization cross sections. The FEL beam ionizes the gas target in the interaction region, and the photoelectron travels through the flight sections of the spectrometer. It is finally detected using the MCP detector at the end of the flight tube. Each of these detectors is connected to the data acquisition system.

4.2.2 Results and discussion

Each e-TOF detector records traces that capture the time-of-flight of the photoelectrons at the MCPs. In a typical experimental run, thousands of such traces, each corresponding to an individual FEL shot, are collected across multiple FEL trains. Figure 4.6 presents a representative photoelectron TOF spectrum of neon, recorded at a photon energy of 75 eV using linearly polarized light. Each peak in the figure represents the averaged spectrum over 1000 single-shot measurements for a given e-TOF angle. The dominant 2p photoelectron peak is clearly observed, with its intensity varying across detection angles. Notably, the 2p electron yield is highest in the horizontally aligned detectors, reflecting the expected angular distribution corresponding to the linearly polarized ionizing beam.

To enable accurate polarization diagnostics, it is essential to calibrate the relative response of each of the 16 e-TOF detectors. This is achieved by referencing the measured angular distribution of the neon 2p photoelectrons to established literature values. The theoretical angular distribution is used as a benchmark for scaling each detector's response, ensuring uniformity across the array.

Each detector's signal is scaled to fit the distribution using the following equation :

$$f(\theta) = C \times (1 + \frac{\beta_{calib}}{2}(3cos\theta^2 - 1)) \tag{4.3}$$

Here, β_{calib} is the anisotropy parameter, which is 1.3 at this photon energy, θ is the observation angle of the detector relative to the polarization axis, C is the scaling factor and $(3\cos^2\theta - 1)$ is the second-order Legendre polynomial that describes dipole emission. The value of β_{calib} is taken from prior experimental and theoretical studies of neon 2p photoionization at the given photon energy [117]. By fitting the observed photoelectron yield from each e-TOF to this function, a unique scaling factor (C) is obtained for each detector. This set of 16 calibration factors ensures that differences in signal intensity across detectors are normalized, allowing for accurate reconstruction of angular distributions in subsequent polarization analyses.

This calibration step represents a critical part of the data preparation pipeline for polarization diagnostics. It ensures that the angle-resolved measurements reflect the physical emission pattern, rather than detector-specific variations, laying the foundation for accurate interpretation of polarization-dependent phenomena.

These well-calibrated spectrometers form the basis for determining the polarization state of the incident FEL pulses. Under the dipole approximation, the angular distribution of pho-

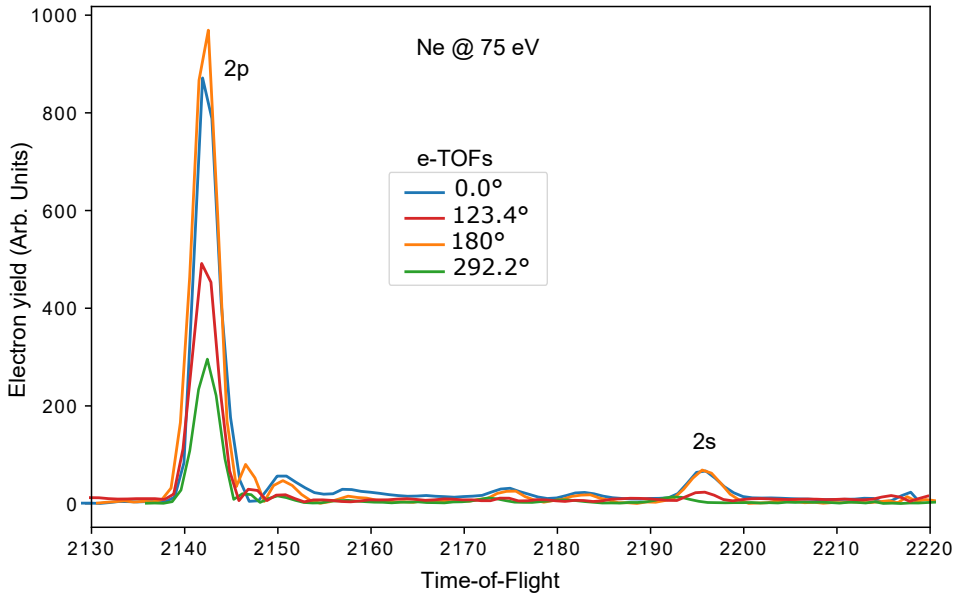

Figure 4.6: Time-of-flight spectra of neon recorded at a photon energy of 75 eV, showing the angular dependence of photoelectron intensity in the dipole plane. The spectra correspond to different spectrometer angles (0.0°, 123.4°, 180°, and 292.2°) relative to the polarization direction. The intensity variation of the 2p and 2s photolines reflects the angular distribution of emitted electrons, consistent with dipole emission patterns.

toelectrons can be used to extract the polarization properties of the ionizing radiation. The photoelectron intensity distribution as a function of the detector angle θ is modeled using the following equation [112],

$$p(\theta) = 1 + \frac{\beta_2}{4}[1 + 3P_{lin}[cos(2(\theta - \psi))]] \tag{4.4}$$

Here, P_{lin} denotes the degree of linear polarization, β_2 is the anisotropy parameter related to the photoionization process, and ψ defines the angle of the polarization axis with respect to the detector geometry. This model assumes that the incoming FEL radiation is fully polarized, with no contribution from unpolarized light. Under this assumption, the degree of circular polarization can be inferred as the complement of the linear component using [112],

$$P_{circ} = \sqrt{1 - P_{lin}^2} \tag{4.5}$$

This methodology has been successfully demonstrated in previous studies, including polarization diagnostics at FERMI by E. Allaria et al. [112] and similar implementations at LCLS [154]. Alternative techniques such as optical and fluorescence-based polarimeters have also

been employed to cross-validate these results [112]. The advantage of the e-TOF-based polarimeter lies in its ability to provide single-shot, angle-resolved information on the FEL polarization, making it an effective candidate for online beam diagnostics.

A set of undulator configurations was characterized using the polarization diagnostic scheme described earlier. The configurations include linear horizontal, linear vertical, and two circular polarization settings labeled ”plus” and ”minus”. It should be noted that the exact handedness (left or right) of the circular polarization is not directly inferable from the setup and requires additional phase information for definitive assignment. The characterization process was particularly challenging due to the limited available pulse energies during the measurement campaign.

For the polarization diagnostics, the 3d photoelectron line of krypton at a photon energy of 313.8 eV was used. The degree of polarization was determined for each undulator setting by analyzing the angular distribution of the photoelectrons. The calculated polarization degrees are:

- $P_{\text{lin}}(\text{horizontal}) = 0.96 \pm 0.02$
- $P_{\text{lin}}(\text{vertical}) = 0.98 \pm 0.02$
- $P_{\text{circ}} = 99.7^{+0.3}_{-0.4}\%$

These results confirm the presence of a circular polarized beam at FLASH 2. Multiple schemes for intensity extraction (including the raw peak value, gaussian fitted intensity etc) from the TOF spectra were applied to cross-check the consistency of the results. These are represented by different colored data points in Figure 4.7, corresponding to each analysis approach.

The presented measurements demonstrate the feasibility and robustness of polarization characterization using an angle-resolved e-TOF spectrometer array, even under the constraint of low pulse energy. While the current implementation relies on averaging multiple shots to extract polarization parameters with sufficient statistical confidence, the consistency of the retrieved linear and circular polarization degrees validates the diagnostic method. Notably, this work marks the first successful realization and characterization of circularly polarized FEL radiation at FLASH, representing a significant milestone for the facility and a major advancement in user capabilities. The ability to reliably distinguish between different polarization states — linear horizontal, linear vertical, and circular — confirms the system’s sensitivity to angular photoelectron distributions and its potential for precise polarization monitoring.

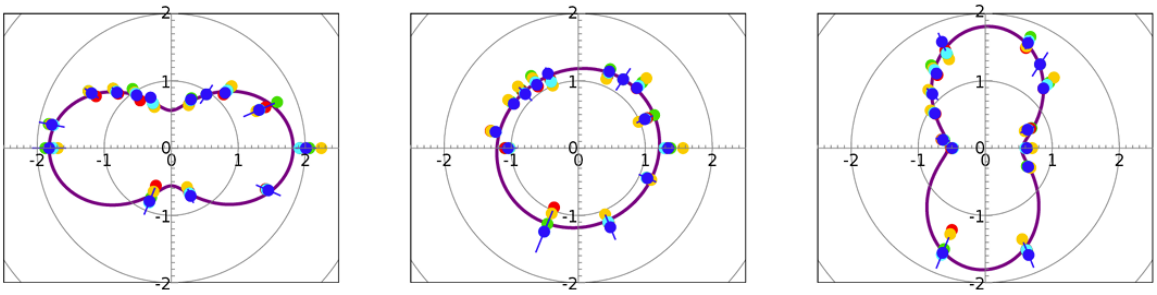

Figure 4.7: Angular distribution of the krypton 3d photoelectron line recorded at a photon energy of 313.8 eV under different polarization conditions: linear horizontal (left), circular (center), and linear vertical (right). The data points represent the intensity of the Kr 3d photoline as measured by each time-of-flight spectrometer positioned in the dipole plane. Different colors correspond to different intensity extraction methods. The purple line indicates a fitted function applied to the measured intensities to describe the angular distribution. Image taken from [155].

These findings highlight the diagnostic scheme as a promising tool for online, non-invasive beam characterization at FELs. With future improvements in data processing, particularly through the integration of machine learning algorithms, the technique could be extended to enable real-time, single-shot recovery of polarization parameters, providing rapid feedback to users during experiments. Such capabilities will be highly valuable for polarization-sensitive investigations.

4.3 High-Resolution Electron Time-of-Flight Spectrometer for FEL Pulse Characterization

The previous sections explored the principles of angle-resolved photoelectron and time-of-flight spectroscopy, which help characterize FEL pulses. This section introduces the development of an advanced, high-resolution e-TOF detector, primarily designed for precisely characterizing FEL pulses. This new spectrometer offers high transmission with improved energy resolution, enabling more accurate and precise diagnostics. These enhancements push the FEL beam diagnostics to new limits, thus providing deeper insights into the ultrafast process on the scale of electron dynamics. Multiple sets of TOF spectrometers have been developed in the past few decades to achieve various characterizations of the photon-matter interaction.

The spectrometer setup discussed in Section 3.1 is one of the initial experimental setups designed for pulse characterization of the variable polarization VUV beamline P04 at PETRA III, also known as the 'cookiebox'. Later, the same setup is used at LCLS for the time-energy characterization of incoming FEL pulses [111]. One of the shortcomings of this spectrometer is its low energy resolution, which is attributed to the small free-flight section. Numerous initiatives at various FEL facilities have focused on developing e-TOF spectrometers with high energy resolution explicitly designed for angle-resolved studies and photon diagnostics. Prominent works in this regard are the 'Ball chamber' TOFs [153], multi-resolution electron spectrometer (MRCO) at LCLS [156], and the high-resolution electron spectrometer for angle-resolved studies at atomic quantum systems (AQS) in Eu-XFEL [118]. Significant design differences exist even though they are all designed for angle-resolved photoelectron studies. Table 4.1. compares the mechanical design parameters of these TOF spectrometers. Building upon the lessons learned from previous developments, this section presents a novel mechanical design to address identified limitations and enhance performance.

The new time-resolving angular spectroscopy applied to the liquid phase (TRANSALP) high-resolution spectrometer is designed for FEL pulse characterization and for capturing the photoelectron in a wide energy window from a few eV to a few hundred eV. The key design parameters, including the length of each retardation section and the total spectrometer length, were determined through the electro-optic simulations to optimize the transmission efficiency and resolution. The spectrometers will be arranged in a vacuum chamber with two independent interaction regions. One is dedicated to gas-phase diagnostics and studies, while the other focuses on liquid-phase studies. Both sections of the interaction are separated using

Spectrometer Version	Total Length (mm)	No. of Retardation Sections
Cookie Box	130	3
Ball Chamber	309	3
MRCO	371.3	25
AQS TOF	420	3
TRANSALP	430	6

Table 4.1: Comparison of mechanical design parameters of different TOF spectrometer versions.

a thin metal plate. With these two interaction regions, a parallel beam diagnostic at the first interaction point, along with the liquid jet experiments in the second interaction region, is possible.

Each TOF spectrometer consists of six independent retardation sections, followed by an extended field-free flight section and a commercially manufactured MCP-based detector. Three copper wire meshes with a transmission of 85% are placed in the main entrance of the spectrometer, at the entrance of the drift tube, and at the end of the drift tube; this helps reduce field penetration between the sections. Figure 4.8 shows the CAD drawing of one of the individual TOF. The detailed mechanical design parameters and constraints will be presented in the dissertation of L. Wülfing. The author of this thesis contributed significantly during the initial phase of the development through simulation work and active participation in design discussions.

In conclusion, the newly developed high-resolution TOF spectrometer represents a significant advancement in the capabilities of FEL diagnostics and angle-resolved photoelectron spectroscopy. Designed with enhanced transmission and energy resolution, the spectrometer is ideally suited for detailed studies of ultrafast electron dynamics and precision beam monitoring. It is planned for installation at the upcoming FL28 beamline at FLASH, where it will serve as a dedicated tool for online beam diagnostics. Beyond diagnostics, the flexible geometry and high-resolution performance make the spectrometer well-suited for a broad range of scientific applications, including angle-resolved studies of gas-phase and liquid-phase targets. While full characterization of the complete system is ongoing, preliminary tests with a single spectrometer have shown promising results, validating the design and its potential. Once fully deployed and calibrated, the setup is expected to play a central role in enabling high-precision, time-resolved experiments at FLASH and contribute significantly to the facility's user program.

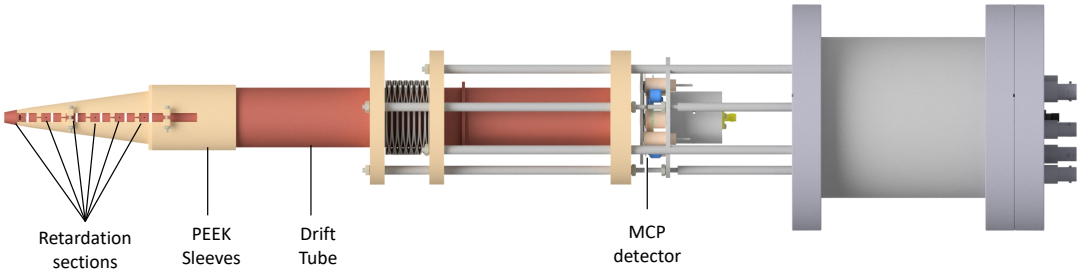

Figure 4.8: CAD model of the newly developed high-resolution TOF spectrometer. Each spectrometer consists of six individual retardation sections and a long drift tube, externally connected to voltage supplies to enable precise electron deceleration and focusing. A commercially available MCP detector is integrated at the end of the drift tube for electron detection. Image generated from [157].

Chapter 5

Single-Shot Spectroscopy of Transient States in Matter

5.1 Introduction

This study investigates core-level photoionization processes in gaseous neon, where inner-shell electrons are ejected upon interaction with high-intensity, ultrashort X-ray pulses. The resulting core vacancies are subsequently filled through relaxation pathways such as Auger relaxation, in which an electron from an outer shell fills the inner-shell hole, releasing energy that ejects another electron. These processes lead to the emission of secondary electrons and charge redistribution within the system. The formation of double-core-hole (DCH) states is particularly interesting via sequential ionization, enabled by attosecond-scale pulses.

We focus on mapping ultrafast electron dynamics associated with DCH formation using an angle-resolving e-TOF spectrometer operated in single-shot mode. The experiment is complemented by non-invasive pulse characterization through angular streaking, which provides attosecond-resolved spectral and temporal information about the ionizing XFEL pulses. A comprehensive analysis is conducted to understand how the DCH yield depends on beam parameters, including pulse duration, pulse energy, and central photon energy. By correlating the ionizing-pulse characteristics with the electronic structure of the transient core-ionized system, we gain valuable insights into nonlinear photoabsorption processes and electron dynamics under high-intensity conditions. The pulse energy and intensity directly influence the probability of multiphoton absorption and the subsequent relaxation pathways [94, 95, 158].

The results discussed in this section are based on the experimental data acquired during the X-ray pulse characterization campaign at the SASE3 beamline of the Eu-XFEL. An e-

TOF spectrometer array comprising 16 detectors was divided into two groups: one with four spectrometers and the other with twelve. Each group operated at distinct retardation voltage settings, enabling simultaneous detection of fast-electron emission from DCH states and complete characterization of the driving FEL pulse. A detailed overview of the experimental setup is provided in Section 5.3.

This experimental approach allows the study of core-relaxation dynamics initiated by intense, attosecond-duration X-ray pulses. The broad photon energy range, high repetition rate, and precise control over pulse parameters at the Eu-XFEL enable the exploration of resonant DCH formation in neon. DCH Auger spectroscopy, in particular, offers powerful insights into transient electron correlation and inter-electronic interactions within highly excited systems. This is because the creation of two core holes amplifies electron–electron interactions, thereby enhancing the sensitivity of Auger decay channels to the local electronic environment [159].

5.2 Double-Core-Hole Ionization in Neon

A DCH state can be produced either through direct photoionization by a single high-energy photon or via sequential absorption of multiple X-ray photons. This section primarily focuses on the latter process, ie, the sequential two-photon absorption mechanism. When an X-ray photon with sufficient energy interacts with a neon atom, whose ground-state electronic configuration is $1s^2\ 2s^2\ 2p^6$, it can eject a core (1s) electron, resulting in the formation of a single-core-hole (SCH) state. The binding energy of the 1s electron in neon is approximately 870.2 eV [26], representing the minimum photon energy required to promote one core electron to the continuum and thus create a SCH state. The resulting singly ionized neon atom (Ne^+) then adopts to the electronic configuration $1s^1\ 2s^2\ 2p^6$. The vacancy created in the core-shell is typically filled by a non-radiative Auger decay process, in which an electron from a higher shell (such as the 2s or 2p level) fills the 1s hole, simultaneously ejecting another electron from the valence shell, commonly referred to as the Auger electron. This relaxation occurs on an ultrafast timescale of approximately 2.4 fs [17]. A schematic representation of the SCH formation and followed Auger decay is shown in Figure 5.1 (a) and (b) respectively. This can be represented as,

$$1s^2\,2s^2\,2p^6 + h\nu_1 \rightarrow 1s^1\,2s^2\,2p^6$$

$$1s^1\,2s^2\,2p^6 \rightarrow 1s^2\,2s^2\,2p^4$$

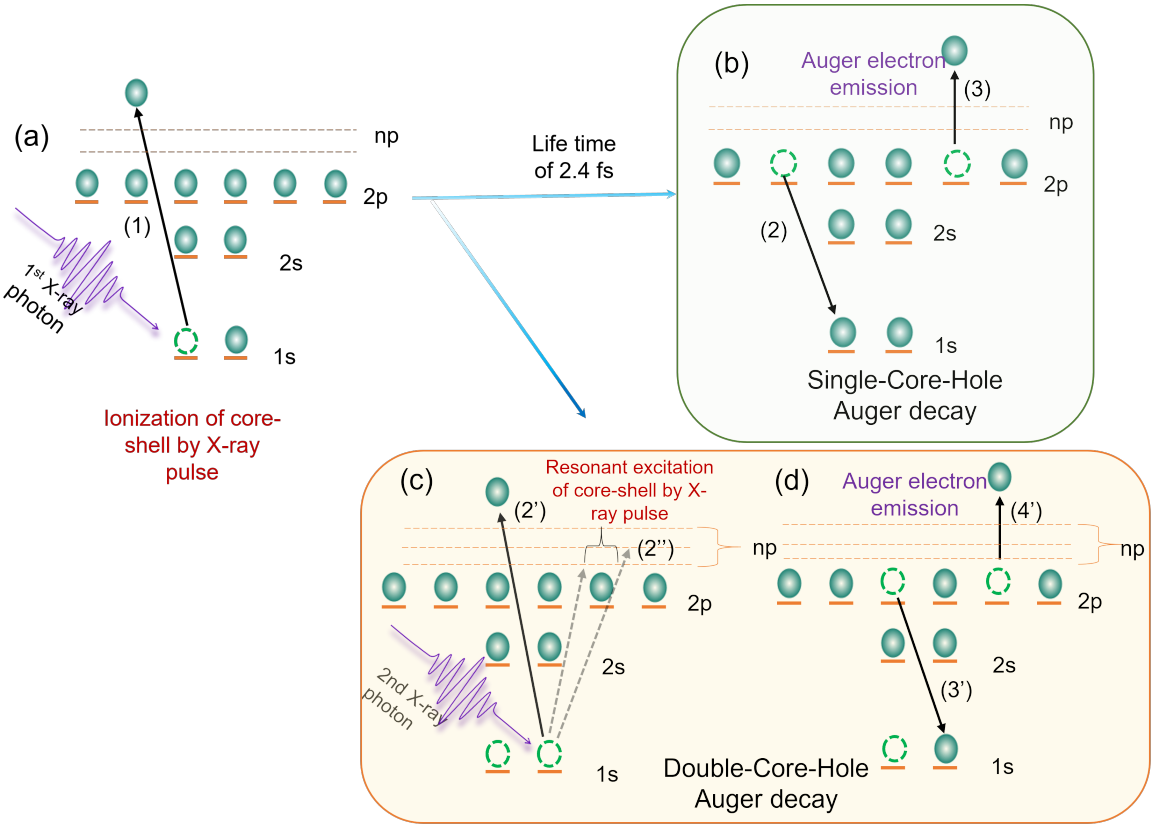

Figure 5.1: Schematic representation of the Auger decay process. (a) Shows the inner-shell ionization by a strong X-ray photon, and thus creates the SCH state (1). In (b) (Ne^{+}), will undergo a relaxation by filling the core hole with a valence electron (2) and ejecting a third electron called the Auger electron (3). (c) If a second photon with sufficient energy to promote the remaining electron in the 1s state comes before the lifetime of the SCH decay, the second electron can be either promoted to the continuum (2') or to a resonantly excited state (transitions shown with a dotted line (2")), creating a DCH state. (d) Shows the relaxation process of the DCH state (3',4').

Following the ionization of the first 1s electron, the remaining core electron becomes more tightly bound, with its binding energy increasing by about 125 eV. The formation of a DCH state is a nonlinear process that occurs only if a second X-ray photon arrives and ionizes this remaining 1s electron before the SCH state relaxes via Auger decay. This requires either a high photon flux or ultrashort pulse durations, both achievable at facilities like the Eu-XFEL. A second photon within the lifetime of the SCH with sufficient energy can create an empty core-shell, described as,

$$1s^1\,2s^2\,2p^6 + h\nu_2 \rightarrow 1s^0\,2s^2\,2p^6\,np^*$$

The non-radiative Auger decay can relax this doubly ionized state.

$$1s^0\,2s^2\,2p^6\,np \rightarrow 1s^1\,2s^2\,2p^4\,np^*$$

Figure 5.1 (c) illustrates the schematic of DCH formation and its subsequent decay in (d). The second photon can either ionize the remaining core electron directly into the continuum or resonantly excite it into a Rydberg state (np^*), as described in [160]. This sequential photoionization of the transient SCH state (Ne^+) to form the DCH state (Ne^{2+} with $1s^0\,2s^2\,2p^6$) is fundamental to probing inner-shell electron correlations and the ultrafast dynamics of highly excited atomic systems.

5.3 Experimental Setup

The experiment was conducted at Eu-XFEL in Schenefeld, one of the brightest X-ray sources. Eu-XFEL is driven by a superconducting linear accelerator with three active beam lines: SASE1, SASE2, and SASE3. This experiment was carried out at the SASE3 beamline, which delivers soft X-rays with photon energies ranging from 0.26 keV to 3 keV at MHz-level repetition rates. The availability of ultrashort pulse durations (<2 fs) in the low-charge mode (20 pC) makes this configuration particularly suitable for time-resolved studies. Conversely, operating at a high bunch charge (1 nC) allows pulse energies of up to 10 mJ. When these high-energy (400 μJ) pulses are focused to a beam diameter of 2 μm, peak intensities exceeding 10^{18} W/cm^2 can be reached, providing favourable conditions for investigating nonlinear X-ray–matter interactions. The X-ray pulses are generated in bunch trains with a repetition rate of 10 Hz. Each train is 600 μs long with 2700 individual pulses in it. Pulses are separated by 220 ns within the bunch train. Figure 5.2 shows the schematic of the pulse structure of the

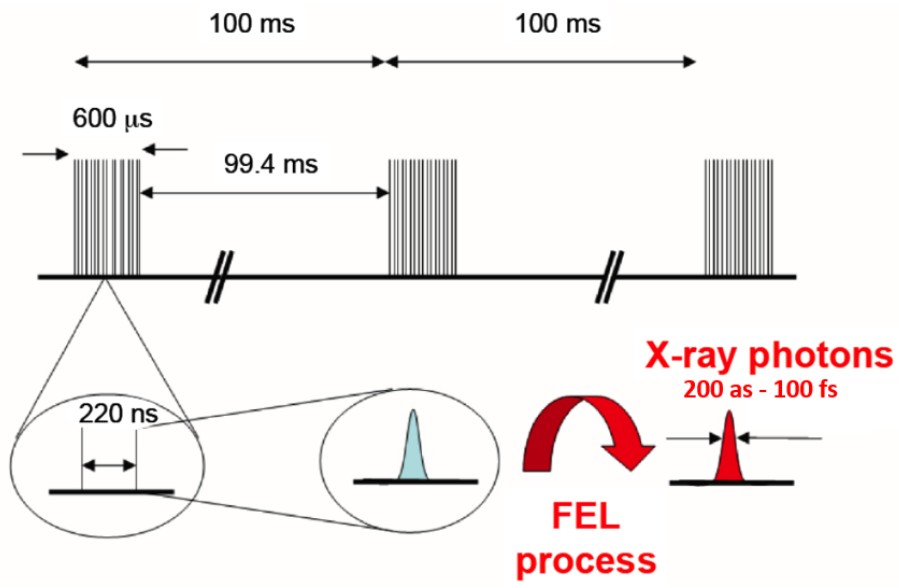

Figure 5.2: Schematic illustration of the pulse structure of the European XFEL. The machine operates with bunch trains at a repetition rate of 10 Hz; each train is 600 μs long. Within each train, there are up to 2700 individual X-ray pulses, separated by 220 ns. The special mode operation provides pulse durations of less than 1 fs (requiring coordinated scheduling with other beamlines). Image taken from [161].

Eu-XFEL [161].

The experimental station offers the possibility of including three sets of focal points along the beam propagation direction. The focusing optics, utilizing Kirkpatrick-Baez (KB) mirrors, enable the selective selection of individual focal points [161, 162]. The experimental setup described in this section is positioned at the F1' focus in the SASE3 beamline.

The schematic of the experimental setup is shown in Figure 4.2 (a). A detector assembly with 16 individual e-TOFs is arranged perpendicular to the plane of X-ray propagation. The individual e-TOF has four retarding sections followed by an MCP-based detector. The retarding sections serve to decelerate and focus the photoelectrons. Each retarding section of the e-TOF is externally connected to a voltage supply, allowing the selection of an operational voltage for each section. The spectrometers were situated within a vacuum chamber, and experiments were performed at a background pressure of 10^{-8} mbar inside the chamber. A fully equipped experimental setup is shown in Figure 4.3.

A dedicated gas-jet system supplies the target gas to the detector chamber. The controlled inflow of neon gas into the detector chamber is achieved using the combination of a needle

valve and a micron-sized gas needle mounted on an XYZ manipulator. A circularly polarized mid-infrared (MIR) optical laser with a wavelength of 4.75 μm is used to streak the photoelectrons generated by X-ray photons. The MIR laser and X-ray pulses overlap in both space and time and are focused on a small radius (< 2μm) inside the detector chamber under high vacuum, known as the interaction region. The FEL pulse is focused to a few micrometres using the KB mirror setup further upstream. A special laser in-coupling scheme, featuring a gold-coated mirror with a central hole, brings the streaking laser beam into the beamline. The linearly polarized X-ray pulses from the Eu-XFEL generate the photoelectron, which is then streaked in space and momentum by the circularly polarized MIR Laser. The streaking laser wavelength determines the upper margin of measurable pulse duration. The spatial and temporal overlap of the X-ray and MIR optical laser is ensured using a sample paddle setup. This includes multiple samples arranged on a tiny placeholder mounted on an XYZ manipulator, which facilitates monitoring the spatial profile of both the X-ray and the laser. A beam probe from Macken Instruments and a YAG crystal are used to detect the spatial profiles of the optical and X-ray beams, respectively. The temporal overlap is achieved using a coaxial cable that serves as an antenna to monitor pulse arrival times.

Two different measurement schemes were conducted during the experimental campaign. The first is the only streaking setup in which all 16 e-TOF spectrometers are set for streaking measurements. All of the spectrometers were in the same retardation set, which is relatively low (80 V). The second scheme is the dual measurement setup, in which 12 e-TOFs are initially set to the same retardation as in the streaking-only mode, and the remaining 4 are set to a different retardation to measure the relaxation dynamics of the transient Ne^{++}. This section primarily focuses on the results obtained from the dual measurement mode.

5.4 Data Correlation and Calibration

5.4.1 Time-to-energy calibration

The extracted ADC traces from the MCP detector are shown in Figure 5.3. Only the ADC traces of 200 trains are plotted here to simplify analysis and improve visual appearance. Each train contains 15 ADC traces corresponding to the FEL's adjacent shots or pulses. Among them, the odd shots are unstreaked and the even shots are streaked. The full range of channels in the ADC trace is not utilized, as the most relevant information lies in channels 150–350, which are highlighted and used for further analysis of the region of interest. Plot (a) shows an unstreaked single-shot spectrum of the DCH decay, (b) shows the average spectrum of all

shots of the first 200 trains in a run, (c) shows the average spectrum of all non-streaked shots, and (d) shows the average spectrum of all streaked shots.

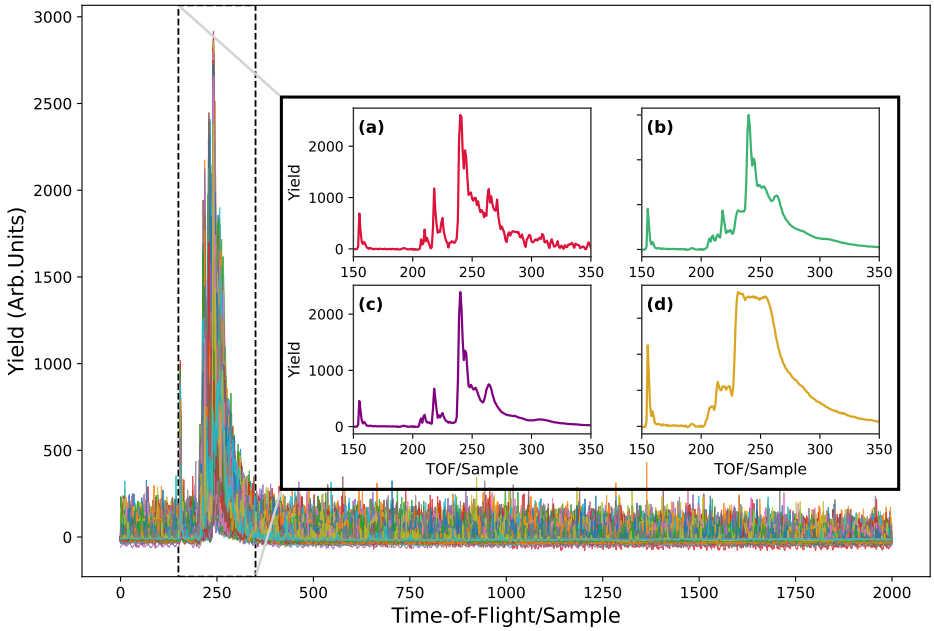

Figure 5.3: Different ADC traces plotted from a single run recorded at 990 eV photon energy and -740 V retardation. The multicoloured background indicates that all ADC traces are loaded, and that only the sample channels from 150 to 350 contain useful data, as marked by the dotted lines. (a) shows a single unstreaked ADC trace, (b) Average of all traces in 200 trains in a run, (c) an average of all unstreaked traces, (d) an average of all streaked traces.

A single run consists of two different data sets: streaked and unstreaked shots. All even shots in the train are streaked (overlapped with the MIR laser field), while the rest are unstreaked. This set of data was recorded at a photon energy of 990 eV with a maximum retardation of -740 V.

The average spectrum of non-streaked shots is shown in Figure 5.4, where distinct spectral features corresponding to SCH and DCH Auger decays are visible at $h\nu = 990$ eV. A time-to-energy calibration is essential to interpret these spectra in terms of electron kinetic energy. Figure 5.6 illustrates the calibration process of converting time-of-flight samples into corresponding kinetic energy values, based on known peak assignments from the literature [17, 163, 164]. The calibration is performed by identifying several well-known Auger features in the non-streaked average spectrum and assigning them to specific core-level transitions. For instance, the peak with the shortest TOF corresponds to the highest kinetic energy electron and is assigned to the 2p photoionization. The next fastest peak is attributed to the 2s

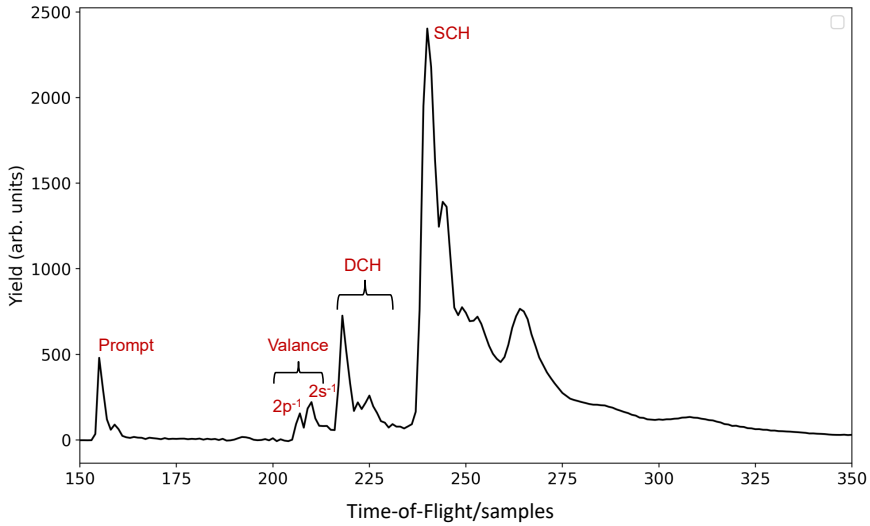

Figure 5.4: The average time-of-flight spectrum of the DCH state of the non-streaked shots. The important spectral features used are marked.

ionization. The kinetic energies for these transitions are estimated using Equation (3.3) and verified against literature values. Additional peaks from DCH and SCH decay processes are also matched to reported Auger electron energies [17, 163, 165, 166]. These reference points are then used to construct a calibration function that maps TOF values to kinetic energies with high precision.

A calibration function is applied to convert the measured TOF values into corresponding electron kinetic energies. This calibration is performed by assuming known kinetic energy values for distinct spectral peaks and fitting them against their respective TOF positions [163]. Once the calibration function is established, it interpolates energy values for all data points between the assigned peaks, resulting in a continuous energy scale. The mathematical relation between the arrival time (t) and the kinetic energy (KE) after travelling a distance (d) could be,

$$t = d\sqrt{\frac{m_e}{2KE}} \tag{5.1}$$

where m_e is the electron mass ($\approx 9.109 \times 10^{-31}$ kg).

In some cases, a polynomial fit function can provide satisfactory results when used for the time to energy conversion, particularly when the energy range is limited or when a polynomial

trend better approximates specific peak positions. Although polynomial calibration, most often quadratic, is standard for time-to-energy mapping, second- and third-degree polynomials were evaluated for the current data set. Figure 5.5 compares the second and third-order polynomial fits applied to the current data set, along with the residual (observed - fit value), which shows the deviation of the prediction from the expected kinetic energy values.

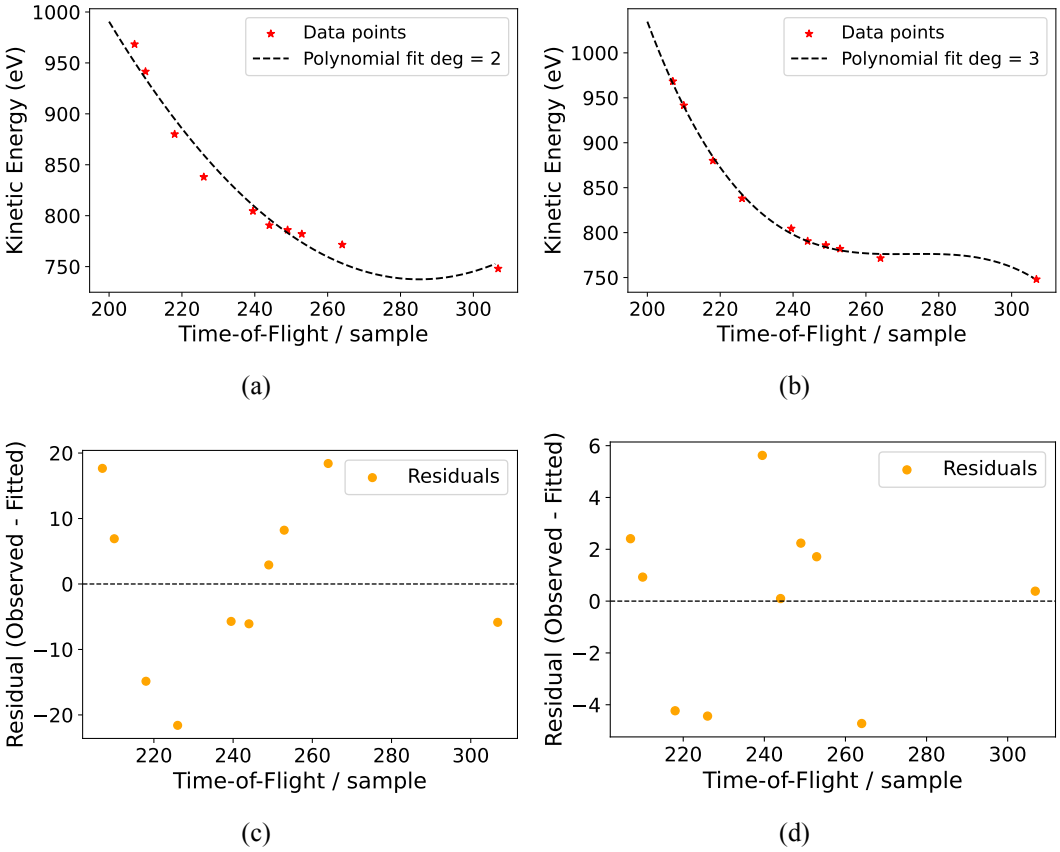

Figure 5.5: Quadratic (a) and cubic (b) polynomial calibrations fitted to the time-to-energy dataset; panels (c) and (d) show the corresponding residuals (estimated − fit). The larger, structured residuals for the polynomial models indicate poorer calibration fidelity for this dataset.

Since the residual from the polynomial fit is large, a negative exponential function is used for this fitting, as it effectively captures the relationship between flight time and kinetic energy. The function used for this calibration is shown in equation 5.2,

$$E(x) = a e^{-bx} + c, \qquad a > 0,\ b > 0 \tag{5.2}$$

where x is the TOF sample value, E(x) is the calibrated kinetic energy, and a,b, and c are the

fit parameters that depend on the dynamic range, the decay rate, and the offset or baseline.

For this dataset, the negative-exponential calibration yields better correlation and more stable interpolation than the quadratic polynomial fit alternative. Because the calibration provides interpolated values, the improved fit accuracy directly increases the accuracy of the mapped energies. Residuals are computed pointwise as the difference between the estimated kinetic energy and the prediction of the calibration function. The quadratic and cubic fits exhibit larger, structured residuals. In contrast, the negative-exponential model leaves small, randomly distributed residuals, indicating that the negative-exponential calibration is best suited for this dataset.

Following the time-to-energy conversion, the resulting spectrum is corrected for the nonlinear transformation by scaling the intensity values. This is achieved by dividing the spectral intensity at each point by the calibration function's differential (i.e., the derivative) as shown in Equation 5.3.

Let $I_x(x)$ be the intensity of the spectrum in the TOF domain, then the scaled intensity of the calibrated spectrum I_E

$$I_E(E)\,\mathrm{d}E = I_x(x)\,\mathrm{d}x \quad \Rightarrow \quad I_E = \frac{I_x(x)}{\left|\frac{\mathrm{d}E}{\mathrm{d}x}\right|} = \frac{I_x(x)}{ab\,e^{-bx}} = \frac{I_x(x)}{b\,[E(x)-c]} \tag{5.3}$$

This correction is essential to compensate for the non-uniform stretching introduced by the nonlinear (often quadratic) nature of the TOF-to-energy mapping. Without this scaling, the area under spectral peaks, an important quantity for quantitative analysis, can be distorted, particularly when comparing features across a broad energy range. This approach ensures an accurate representation of the spectrum, preserving the physical relevance of integrated quantities such as peak areas.

The importance of this calibration lies in its ability to accurately extract physical information from measured TOF data. Without such a mapping, interpreting energy-resolved electron spectra, especially in ultrafast dynamics studies, would be imprecise. Figure 5.6 (a) shows that the resulting calibration function exhibits an excellent correlation between the TOF values and the assigned kinetic energies. This function is subsequently applied to the average spectrum, as shown in Figure 5.6 (b), enabling a fully energy-calibrated representation of the photoelectron spectrum. The significant contributions shown in Figure 5.6 are the L shell photoionization peaks (L^{-1}), which are the fast and weak spectral features around 985 eV-940 eV. The peaks under the notation DCH represent the hypersatellites of the K^{-2} state, and the sharp and narrow peak around 800 eV corresponds to the Auger decay of the K^{-1} state.

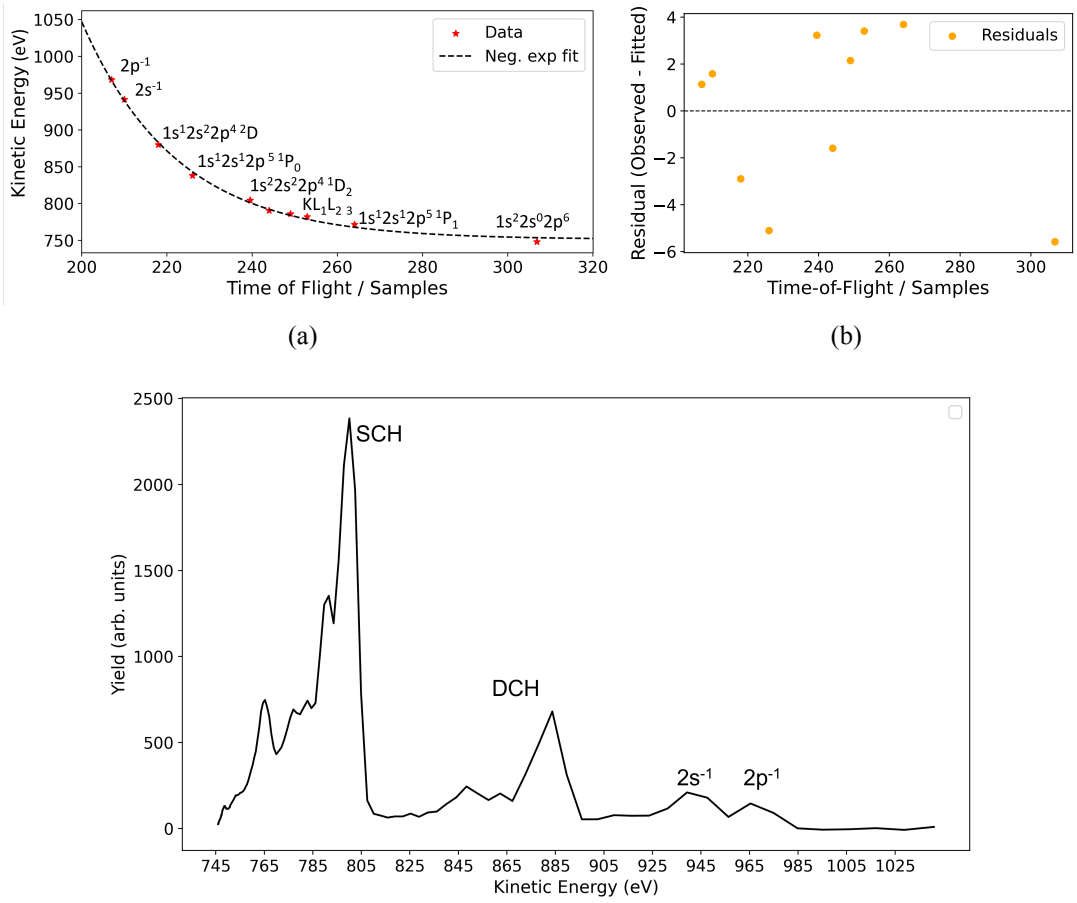

Figure 5.6: (a) Shows the ADC trace calibration from time-of-flight to kinetic energy. The photoelectrons and Auger electrons marked in red are based on the literature. The residual of the fit function is shown in (b). (c) Shows the energy-calibrated spectrum of Figure 5.4 with kinetic energy on the x-axis and the relative electron yield on the y-axis without the intensity scaling.

5.4.2 Pulse-energy-based correlation with X-ray gas monitor detector (XGMD)

An X-ray gas monitor detector (XGMD) is installed upstream of the experimental end station to provide real-time measurements of the FEL pulse energy and photon beam position [74]. These detectors operate on the principle of photoionization of rare-gas targets, similar to the gas monitor detector (GMD) used at FLASH [167,168]. The XGMD functions at considerably lower gas pressures on the order of 10^{-6} to 10^{-4} mbar, which helps suppress the generation of secondary electrons, improving signal clarity and temporal resolution.

During operation, photoionization of the rare gas generates electrons and ions, which are extracted in opposite directions by a uniform electric field. These ion and electron signals are detected in pulse mode, allowing shot-to-shot measurement of the FEL pulse energy. However, the photoionization cross-section decreases significantly at higher photon energies, especially for heavy rare gases like xenon [169], posing challenges for use in hard X-ray regimes. Traditional ionization chambers are unsuitable for such high-intensity, fast-repetition-rate applications due to space-charge effects, as accumulated electrons or ions can distort the local electric field, degrading temporal resolution. To overcome these limitations, the XGMD, a modified and improved version of the GMD, is used at Eu-XFEL [74]. It offers high detection efficiency across a broad photon energy range, from vacuum ultraviolet (VUV) to hard X-rays, with a temporal resolution below 200 ns [33].

Figure 5.7 (a) presents the pulse energy measurements from the XGMD for a typical data run. The data shown were acquired from the tunnel-installed XGMD and include 9047 trains, each comprising 15 individual shots, for a total of 135,705 data points. The blue scatter points represent the pulse energy of individual shots, while the black dotted line indicates the average pulse energy across the run. The pulse energy spans a wide range from 0 to 500 μJ, reflecting significant shot-to-shot fluctuations arising from the special operation mode used in this experiment, which are considerably lower during normal operation. To assess how these fluctuations impact the electron yield from the target in the experimental end station, we correlate the XGMD-measured pulse energy with the total electron signal on a single-shot basis. Figure 5.7 (b) illustrates this correlation in a scatter plot, where each dark point represents the sum of the electron signal within a defined region of interest versus the corresponding FEL pulse energy for a given shot. For comparison, a background grey scatter plot is included, showing a one-shot-shifted array that highlights the absence of correlation when the true pairing between pulse energy and signal is absent.

This type of pulse energy–based correlation analysis is crucial for evaluating data quality

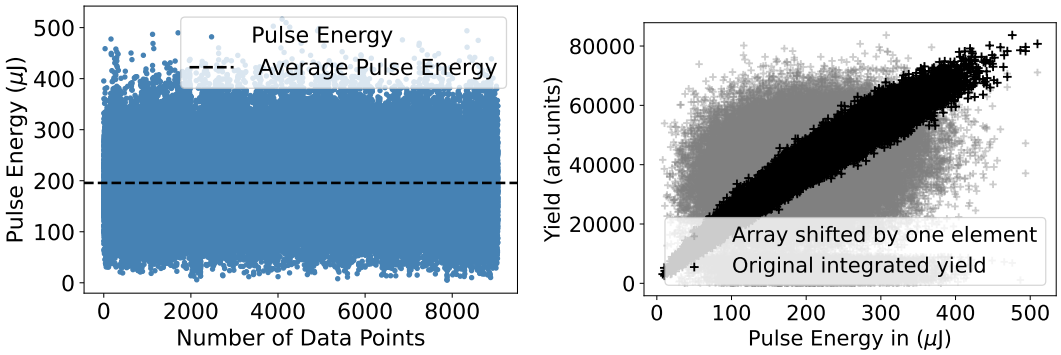

(a) (b)

Figure 5.7: (a) Distribution of pulse energy values for all non-streaked shots.The black dotted line represents the average pulse energy, while the blue scatter points indicate the pulse energy of individual shots, clearly illustrating the shot-to-shot fluctuations. (b) Correlation between the integrated electron yield per trace and the corresponding pulse energy (black scatter points). The grey background points show the result of a one-element-shifted array, illustrating the absence of correlation.

in studies of nonlinear X-ray–matter interactions. Since nonlinear processes, such as DCH formation, depend strongly on the intensity of the X-ray pulse, variations in pulse energy directly affect the likelihood and yield of such events. Establishing a reliable correlation between the measured pulse energy and the resulting electron signal confirms the process's sensitivity to intensity. It ensures that the dataset is suitable for interpreting nonlinear behavior through the dependence on the yields of intensity and multiphoton processes. Moreover, this correlation is an important validation step for identifying and filtering out low-quality or noise-dominated shots that could skew the analysis of ultrafast electron dynamics.

Figure 5.8. provides a detailed overview of how the TOF spectrum evolves as a function of pulse energy. The top panel displays a histogram of the FEL pulse energy values recorded by the XGMD during the experimental run. This distribution highlights the broad range of pulse energies sampled in the dataset, with noticeable clustering within specific energy intervals. To analyze how the spectral features vary with pulse energy, the dataset was binned according to the histogram and averaged within each bin.

The bottom panel of the figure shows the resulting average electron spectra corresponding to each pulse energy bin. This representation allows for a direct comparison of how the intensity and shape of the spectral features evolve with increasing pulse energy. Notably, any nonlinear enhancement in features, such as those associated with DCH formation, can be tracked through these averaged spectra. This approach enables the identification of pulse en-

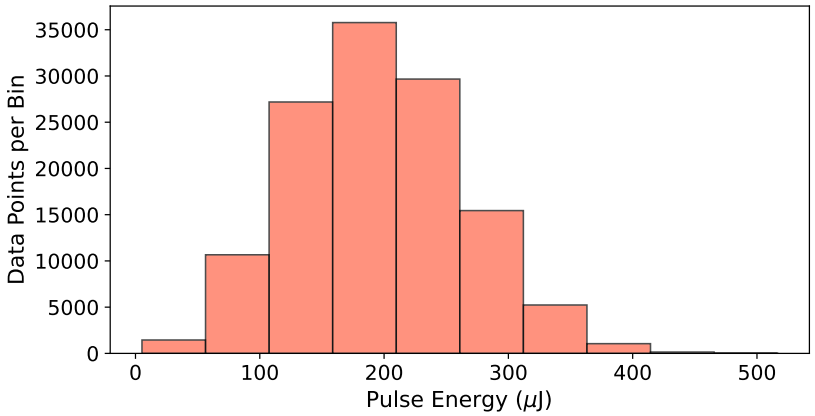

(a)

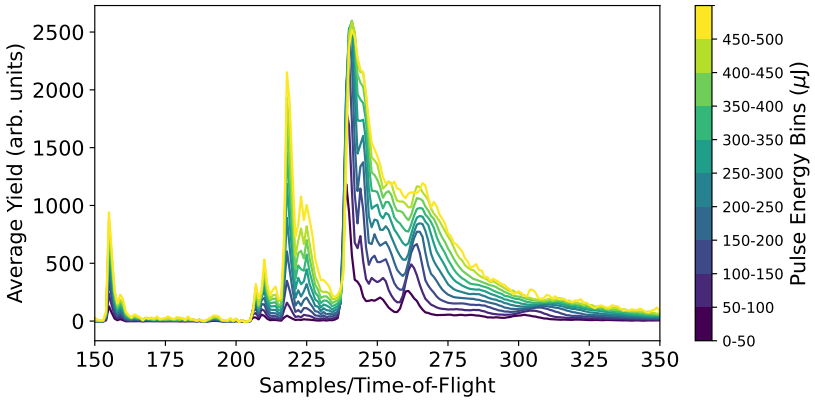

(b)

Figure 5.8: XFEL pulse energy dependent signal yield. (a) Shows the binning of the total pulse energy range. Each bin is 50 μJ wide, covering the range from 0 μJ - 500 μJ. The average spectrum corresponding to each pulse energy bin is shown in (b).

ergy regimes where specific ionization pathways become more pronounced, thereby offering a deeper understanding of the intensity-dependent dynamics in strong-field X-ray interactions. This pulse energy–based correlation analysis primarily serves as a validation step to ensure the consistency and integrity of the dataset. The observed increase in electron yield with rising pulse energy confirms that the spectral features, particularly those associated with multi-photon processes like DCH formation, respond as expected to intensity variations. Intensity-dependent characterization of single-shot spectra is discussed in the following section.

5.5 Intensity-Dependent Single-Shot DCH Characterization

Nonlinear light–matter interactions in the X-ray regime represent a frontier in ultrafast science, enabled by the advent of high-intensity, femtosecond and attosecond pulses produced by XFELs [97,170]. Among these interactions, the formation of DCH states is of particular interest, as it requires the photoabsorption of two high-energy photons within a timescale shorter than the intrinsic core-hole lifetime. This inherently nonlinear process, which is inaccessible with conventional light sources, is highly sensitive to both pulse intensity and temporal structure [171]. Studying DCH formation offers unique insight into inner-shell electron dynamics, electron correlation, and the evolution of highly excited atomic or molecular systems on femtosecond timescales. This section focuses on the intensity-dependent, single-shot characterization of DCH formation in neon, leveraging the capabilities of the Eu-XFEL to reveal signatures of nonlinear ionization under high intensity conditions.

The Auger electrons emitted from a DCH state serve as a clear signature of hollow-atom formation, ie, a completely empty 1s shell [172]. Such states occur only when the photoionization rate is comparable to or exceeds the SCH Auger decay rate, typically within a few femtoseconds [172] [17]. The formation of a DCH state is susceptible to the photon flux and, thus, indirectly to the temporal duration and individual pulse energies of the ionizing X-ray pulse.

Figure 5.9 shows a comparison of the averaged spectrum and a single-shot spectrum corresponding to DCH formation in gaseous neon, measured at a photon energy of 990 eV with a retardation voltage of -740 V. The spectrum in purple represents the average of over 67,000 unstreaked shots, contrasting with single-shot spectra that capture the transient behavior of neon under the influence of a single intense FEL pulse. A detector at an angle of 67.8 °is used to monitor the DCH signal, benefiting from reduced background noise from photoelectrons due to the linear polarization of the incoming XFEL pulses. The enhanced signal around the DCH region demonstrates the potential of this method for capturing ultrafast, short-lived phenomena even on a single-shot level. It is assumed that the Auger electrons emitted by the ionization of an inner-shell electron result in an isotropic angular distribution, which makes it very convenient to choose any detector for characterizing the DCH states independent of the detection angle [173, 174].

This work demonstrates single-shot characterization of the DCH process, which has not been previously shown with this level of detail. The tight X-ray focus ($< 2\ \mu$m) combined with pulse energies of up to several hundred microjoules results in peak intensities exceeding 10^{18}

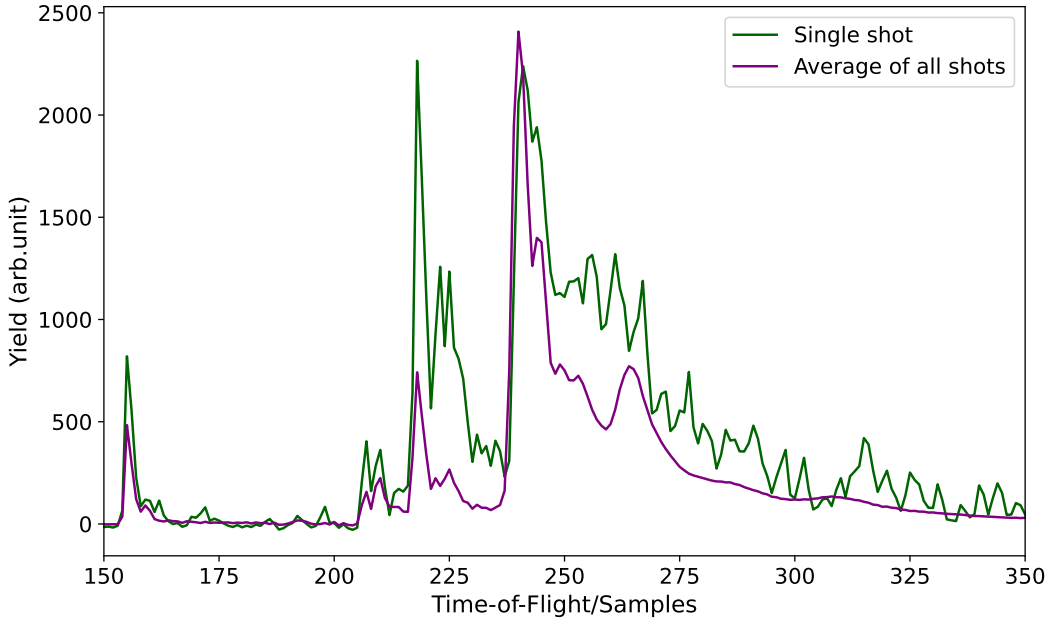

Figure 5.9: Comparison of a particularly strong single-shot spectrum with the average of all non-streaked shots for neon at a photon energy of 990 eV. A high-intensity X-ray pulse is capable of demonstrating a statistically robust DCH state in a single shot.

W/cm^2. For the estimation, an average pulse energy of 200 µJ and an average pulse duration of 2 fs were assumed, consistent with streaking measurements indicating that 80% of the pulses had durations below 2.5 fs [88]. It should be noted that higher pulse energies and shorter durations are also observed, leading to even higher instantaneous peak intensities. These conditions are sufficient to reach the nonlinear ionization regime where sequential absorption of two photons from the same FEL pulse leads to DCH formation. Capturing this process on a single-shot basis not only provides insight into the dynamic evolution of the core-ionized system but also allows for direct, pulse-resolved access to the transient electronic structure of neon. This capability of pulse-resolved characterization of nonlinear photoabsorption is especially important at XFELs, given the stochastic nature of SASE pulses. Each pulse carries different spectral and temporal characteristics, which in turn influence the associated ionization and decay pathways. Correlating the electron yield with the pulse energy on a per-shot basis reveals how individual XFEL pulses can lead to markedly different DCH yields. Such single-shot resolution enables a deeper understanding of nonlinear X-ray–matter interactions in a pulse-resolved manner. It lays the groundwork for future FEL-pump FEL-probe experiments, where individual pulse characteristics play a crucial role in the observed dynamics.

While averaged spectra provide a helpful overview, they often obscure the variability and

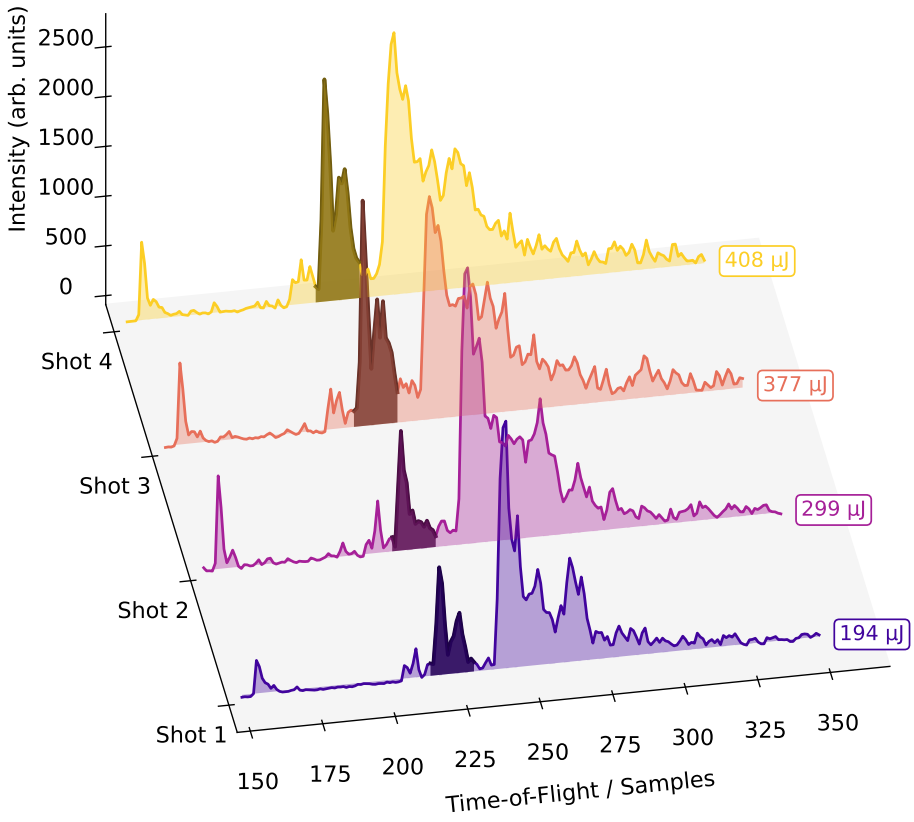

Figure 5.10: Time-of-flight spectra from four individual FEL shots, recorded for hollow-core neon at a photon energy of 990 eV. Each spectrum corresponds to a single FEL pulse with a distinct pulse energy. The variation in spectral intensity of the DCH signal across the shots highlights the nonlinear dependence of DCH formation on FEL pulse energy. The less transparent region in each plot represents the DCH contributions.

richness of individual events. In contrast, high-statistics single-shot spectra, combined with pulse characterization, allow for a more detailed reconstruction of the physical processes involved. The observed increase in DCH signal with pulse energy and its eventual similarity to the SCH yield indicate that at higher intensities, a significant fraction of neon atoms undergo double ionization within the core-shell. While the formation of DCH states is primarily governed by the photon flux or intensity rather than directly by the pulse duration, pulse duration still plays an indirect role. A sufficiently intense photon field is required to absorb a

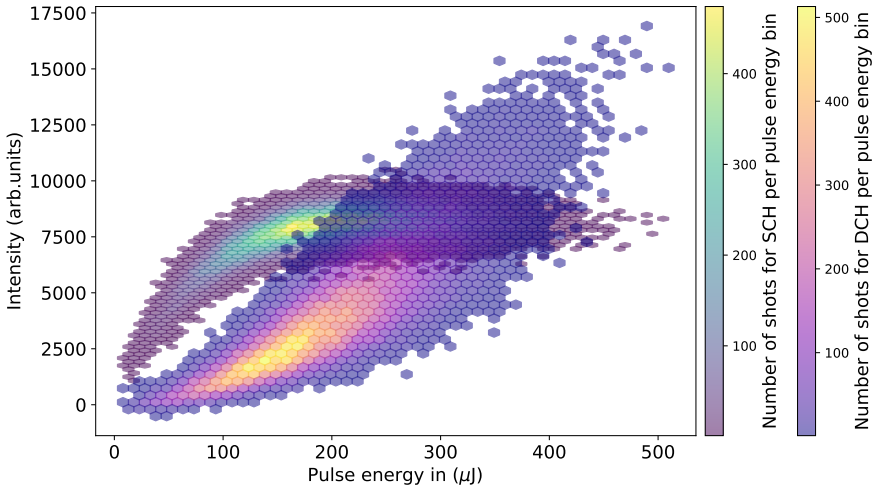

(a)

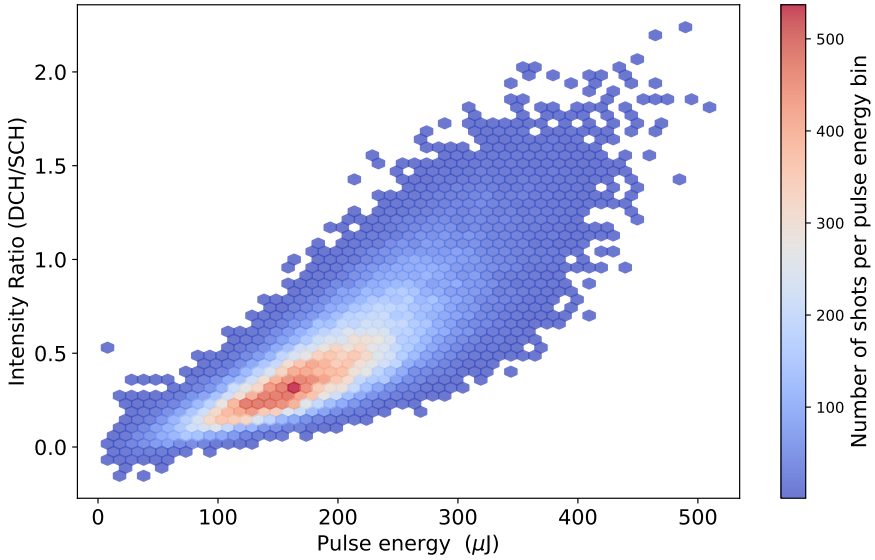

(b)

Figure 5.11: Pulse energy dependence of the Auger decay process. The intensity plot depicts the yield of DCH formation relative to SCH formation as a function of pulse energy (in μJ), shown in (a). The increasing DCH-to-SCH ratio in (b) indicates a positive trend, that most atoms undergo the hollow-core state.

second photon within the Auger decay window of the SCH state (typically <2.4 fs for neon). Although DCH states can, in principle, be produced using longer pulses provided that the intensity is high enough, the intensity for a given pulse energy increases as the pulse duration decreases. Therefore, knowing the pulse energy, observing efficient DCH formation can serve as an indirect indication that the FEL pulses are relatively short, since shorter pulses

naturally yield higher peak intensities at the same energy. Figure 5.10 shows a successive increase in the DCH formation signal in a single-shot with the pulse energy. Each spectrum shown represents a sequential ionization event induced by a single XFEL pulse at different pulse energy settings. This graph compares the reproducibility and robustness of the single-shot characterization of the DCH state at various pulse energy levels.

Figure 5.11 shows the ratio of DCH to SCH yields as a function of pulse energy, for all the non-streaked shots, further supporting this interpretation and highlighting the role of intensity in driving nonlinear ionization processes.

Notably, the dataset exhibits saturation of the SCH signal at higher pulse energies, as illustrated in Figure 5.11. As pulse energy rises, the DCH yield continues to increase, while the SCH yield plateaus, indicating a fundamental relationship between the dynamics controlling the two processes. This saturation likely results from the onset of effective sequential ionization; the likelihood of a second photon being absorbed within the lifetime of the SCH state increases as the X-ray intensity rises. Consequently, the system transitions quickly from the SCH state to the DCH state before the first core hole can undergo Auger decay. This depletes the SCH population essentially and clarifies why its yield no longer scales with pulse energy in the same manner as the DCH signal. Stated differently, at high intensities, the saturation of the SCH state serves as an indirect indication of DCH dominance. This transition also highlights the competition between ultrafast Auger decay and nonlinear photon absorption, an important characteristic of inner-shell electron dynamics under extreme field conditions.

Furthermore, these observations indicate that the experimental regime accessed in this work is consistent with high-intensity, few-femtosecond conditions where such dynamics can be resolved, highlighting the efficiency of DCH creation as a nonlinear process. The observed saturation could potentially indicate a regime in which almost all atoms that can be singly ionized are instead driven directly to the DCH state, thereby avoiding the SCH decay channel, which becomes a transient intermediate rather than a stable observable state. These results are strongly correlated with the observations in Section 5.6, where the enhancement of the DCH signal, along with pulse duration estimation, is explored in detail. An estimate of the pulse duration for every alternate pulse was obtained using the streaking technique. This result supports the observation that, at high pulse energies, the majority of the target undergoes sequential ionization, likely due to the short timescale of the incoming X-ray pulse. The concentration of high energy within a small pulse area makes the intensity regime suitable for nonlinear sequential photoabsorption.

5.6 Pulse Duration Dependence on the DCH Formation

The X-ray pulse duration retrieval measurements obtained from the angular streaking method (Section 4.1) provide shot-to-shot information about the pulse duration [88]. This section presents a qualitative correlation between the measured pulse duration and the yield of DCH states. The pulse-duration characterization employing angular streaking was primarily performed by L. Funke et al. [88]. The author of this thesis was closely involved in the experimental campaign, and with the contributor's permission, I have incorporated selected datasets into this section of the thesis. Where relevant, these measurements substantiate and complement the conclusions I draw from my independent analyses. Additional experimental details and a comprehensive discussion of the angular-streaking methodology will appear in the forthcoming dissertation of L. Funke.

The experiment used a dual-measurement scheme, where 12 TOF spectrometers were dedicated to reconstructing the ionizing pulse at a low retardation voltage of -80 V. In contrast, the remaining four detectors were used to monitor charge rearrangements in transient neon atoms with a relatively high retardation of -780 V applied, since the kinetic energy of Auger electrons is high. Requirement for observing double-ionized neon is the sequential absorption of a second photon with sufficient energy ($h\nu = 990$ eV) within the decay lifetime of the singly ionized K-shell electron. The pulse duration measurements, performed in parallel, yield the FWHM of the reconstructed X-ray pulse. Based on these values, a study is conducted on the yield of the DCH state at different estimated durations of XFEL pulses.

The observation of the DCH state, which arises from a nonlinear ionization process, serves as an indirect yet clear indicator of the high intensity of the ionizing X-ray beam. Figure 5.12 compares the DCH Auger TOF spectrum recorded with (a) and without (b) the presence of the streaking laser.The streaked spectrum exhibits a shift in flight time that depends on the streaking phase, as previously described in Section 4.1. Only shots with pulse energy within the range of 200 ± 30 μJ were selected to ensure statistical reliability and minimise fluctuations in photon flux. These shots were further filtered based on the streaking laser phase to isolate the effects of a specific field direction.

The X-ray beam used in this experiment is tightly focused to a diameter of less than 2 μm and has a pulse duration of less than 4 fs, resulting in peak intensities exceeding 10^{17} W/cm^2. The streaking phase is determined from the center-of-mass of the reconstructed XFEL pulse, which allows the selection of a specific direction of the streaking field [88].

Out of 73176 total streaked shots, only 1578 shots satisfied the filtering criteria based

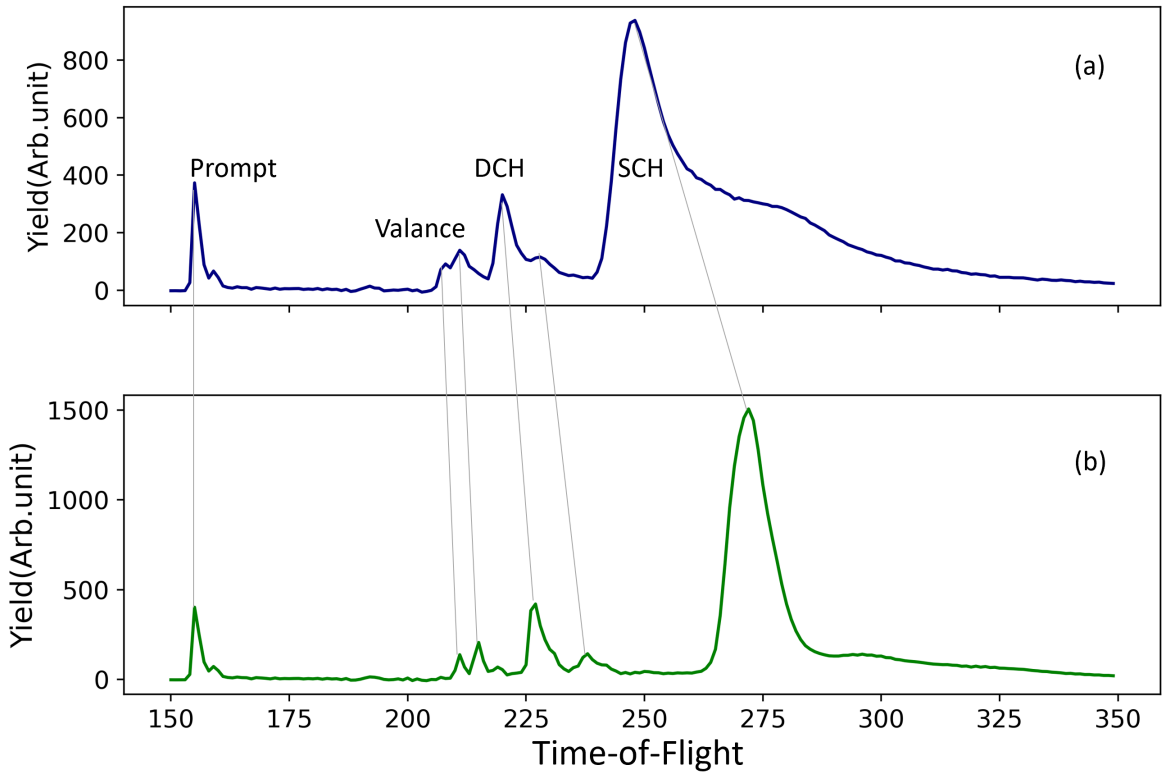

Figure 5.12: Comparison of streaked and non-streaked spectra in the time-of-flight domain. The top panel (a) displays the average spectrum of all shots acquired at a carefully selected streaking phase, chosen to produce a positive streaking shift, an effective shift of the spectral features toward higher kinetic energies (shorter TOF values). The bottom panel (b) shows the corresponding non-streaked average spectrum, recorded without the influence of the streaking field. A clear shift of the spectral peaks toward shorter TOF values is observed in the streaked spectrum, highlighting the effect of the streaking field. Vertical lines mark the peak positions in both spectra to visually emphasize this energy shift.

on pulse energy and the streaking phase. Figure 5.13 presents the variation in DCH yield as a function of pulse duration at two different streaking phase settings. The streaked DCH spectrum corresponding to an upshift and downshift of energy is shown in the top and bottom panels, respectively. This intensity-dependent increase in DCH yield is a cross-validation for the pulse duration analysis. The peak intensity remained relatively constant since the pulse energy window was narrow. Under these conditions, an increase in DCH yield can be attributed primarily to shorter pulse durations. The mechanism involves sequential photon absorption: the first photon creates a SCH state with a decay lifetime of approximately 2.4 fs. A higher intensity achieved through shorter, more intense pulses increases the likelihood that a second photon is absorbed before the SCH state decays, thus forming a DCH state.

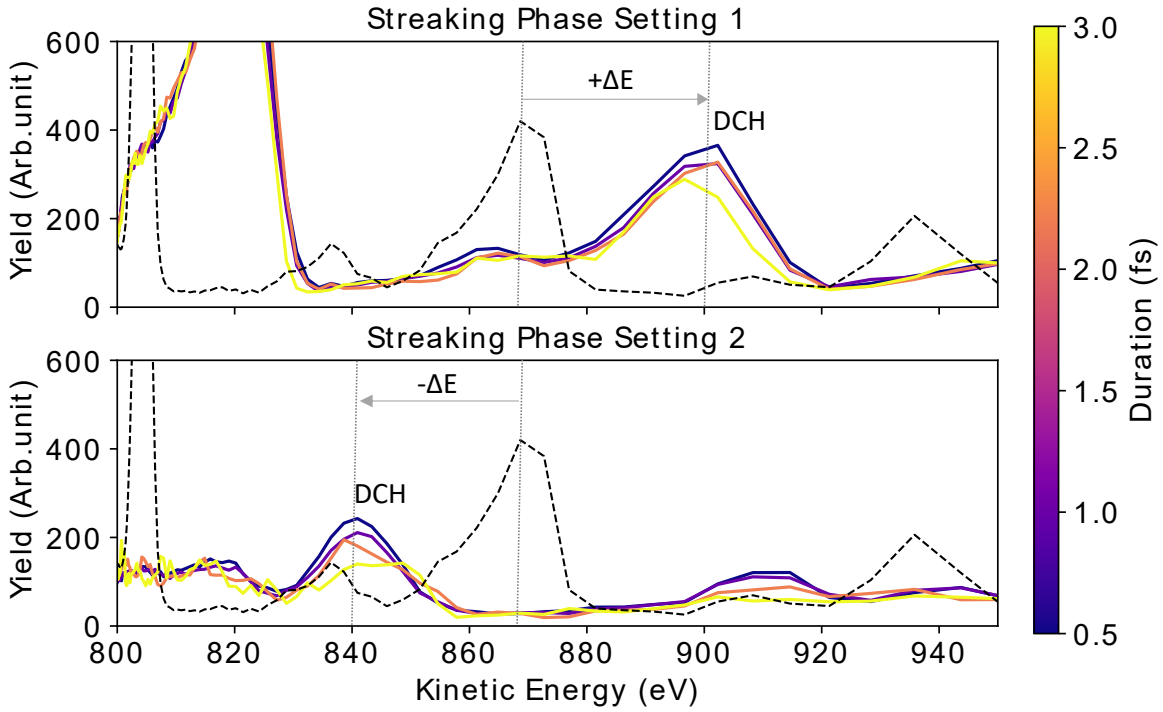

Figure 5.13: Pulse duration dependent comparison of DCH yield. The DCH yield is sorted according to the pulse durations estimated from the reconstructed X-ray pulses. The top and bottom panels display intensity plots of DCH formation for two different streaking phases. In the top panel, a positive streaking shift of the DCH spectral peak is observed, corresponding to one streaking field direction, while the bottom panel shows a negative shift, indicating the opposite streaking direction. The black dotted line represents the spectrum recorded without the presence of the streaking field (unstreaked spectrum), serving as a baseline for comparison. The streaking phase is carefully selected to show the shift of the peaks to shorter TOF. Image reproduced based on [88].

The observed increase in DCH yield with decreasing pulse duration has significant implications for characterizing ultrafast nonlinear processes in atoms. Most notably, the enhancement of the DCH signal due to the high photon flux, which in turn could be a result of the short pulse, since the pulse energy is kept in a narrow range. Although DCH spectroscopy is also possible with longer pulse durations, with sufficient photon flux, the observations shown here are particularly important because they provide experimental validation that the individual X-ray shots can reach the temporal regime required for inducing sequential core ionization within a single atom. Such conditions are challenging to confirm directly and often rely on pulse diagnostics that are not intrinsically tied to the ionization dynamics.

Furthermore, this correlation between increased DCH yield within a specific pulse-energy window provides indirect validation of the pulse-duration measurements obtained via angular-streaking diagnostics. The streaking method provides an independent, shot-resolved estimate of the X-ray pulse duration. The observation that only shots with streaking-determined durations shorter than the SCH lifetime yield significantly enhanced DCH signals confirms that the retrieved pulse durations are physically meaningful and consistent with the dynamics of sequential ionization. In this way, the DCH yield not only reflects the underlying nonlinear interaction but also acts as an indirect benchmark for the accuracy of the temporal metrology employed in the experiment. This insight strengthens the utility of DCH formation not only as a probe of electronic relaxation dynamics but also as a powerful validation tool for nonlinear regime accessed in FEL-based experiments, paving the way for time-domain studies of inner-shell interactions at their fundamental limits.

5.7 Spectral Sorting of Single-Shot Resonant DCH Decays

The smooth tunability, ultrashort pulse duration, and high repetition rate of the Eu-XFEL provide an excellent platform for characterizing DCH resonances in neon, despite the relatively broad spectral bandwidth in SASE operation. The experiment was performed with a special mode, where the majority of the shots had durations shorter than the lifetime of the SCH state, ie, 2.4 fs. The previous section explored the dependence of DCH formation yield on pulse energy, highlighting a high probability of second-photon absorption. Utilizing the tunability of the X-ray pulse, it is possible to excite the second core electron into a resonant state selectively. This section focuses on mapping these resonant Auger decay as a function of photon energy. However, the relatively large bandwidth of the X-ray pulse ≈ 9 eV poses a challenge, as it exceeds the energy separation between many resonant states. Additionally, the limited energy resolution of the TOF spectrometer used in our experiment further constrains the ability to resolve closely spaced resonances from the current data. In principle, the energy resolution can be improved by applying a high retardation voltage. However, in this work, a lower retardation voltage (-780 V) is used to cover a broad energy range (over 80 eV) while maintaining a flat transmission for the angular streaking measurements performed in parallel.

The conventional approach to characterizing resonant states involves scanning the photon energy in steps of a few eV. Figure 5.14 presents a photon energy scan of the DCH states from 970 eV to 1020 eV, using a step size of 10 eV. A distinct feature corresponding to DCH formation emerges around 990 eV and becomes more pronounced with increasing photon energy. The resonant mapping reported by T. Mazza et al. [17] for the transient neon state offers valuable insight into the multiple possible transitions of the second core electron as a function of photon energy.

The combined effects of the ultra-short pulse duration and stochastic SASE generation result in a large spectral bandwidth, limiting the ability to resolve the resonant structure near 990 eV and to distinguish discrete resonant states, even with fine photon-energy scanning. Additionally, the detector's resolution is crucial in resolving distinct spectral features. Due to the lack of effective fine-step photon energy scans, an alternative approach was implemented: sorting the resonances based on the intrinsic bandwidth of the X-ray pulses for a given undulator setting. This method enables partial reconstruction of the resonance profile despite the limited energy resolution and detailed scan.

Sorting the resonance structures from the bandwidth of X-ray pulses can be challenging, so an additional diagnostic tool is employed. The photoelectron spectrometer (PES), which

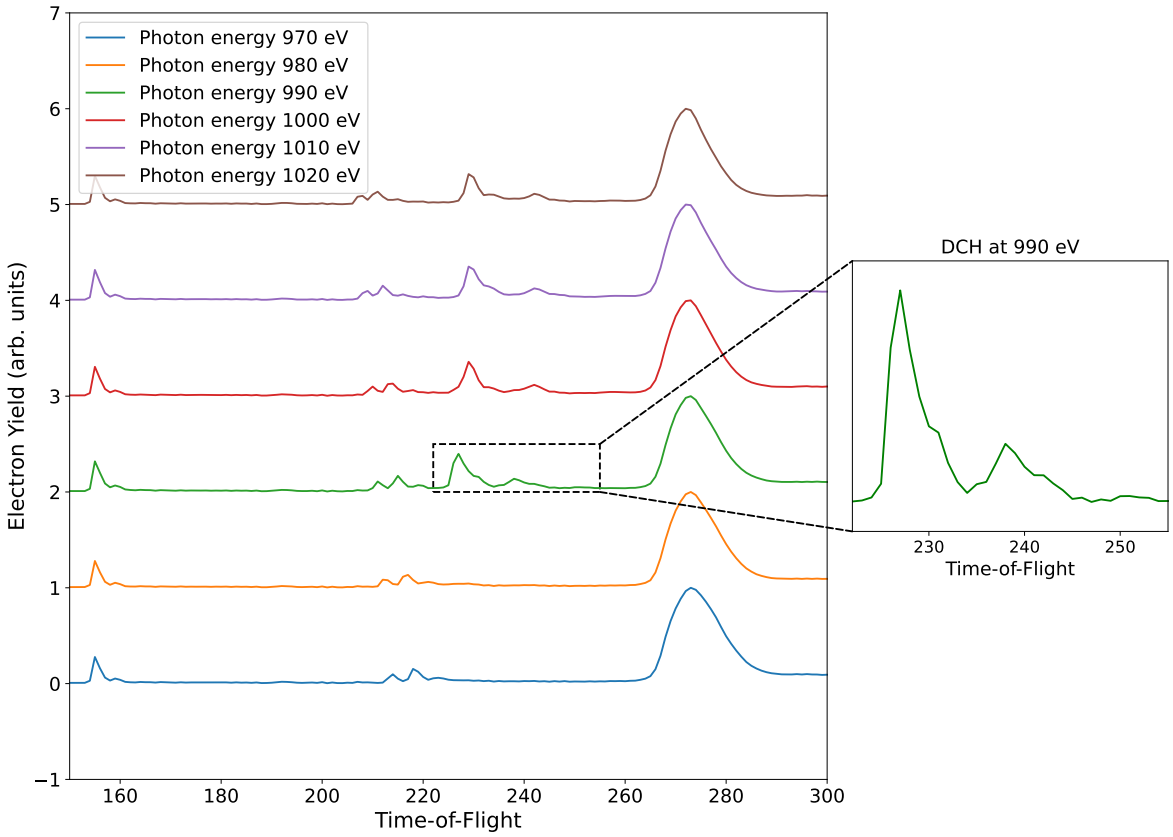

Figure 5.14: Photon energy scan from 970 eV to 1020 eV in steps of 10 eV. The dotted rectangle highlights the emergence of the DCH feature around 990 eV. The green inset shows a magnified view of this region, emphasizing the appearance of the DCH signal.

is having a functioning similar to the apparatus that introduced earlier in section 3.2, is used for this purpose. An angle-resolving PES is installed a few meters upstream of the current experimental setup, allowing independent diagnostics of individual shots. This spectrometer is capable of providing photon energy and bandwidth information on a single-shot scale. The PES spectrometer installed in the tunnel is a non-invasive diagnostic tool that provides single-shot information on both the spectral distribution and polarization of the XFEL pulses [76]. The schematic of the PES spectrometer is shown in Figure 5.15.

This angle-resolving spectrometer setup uses low-density rare-gas targets to generate photoelectron spectra, which are instrumental for characterizing the spectral properties of the ionizing XFEL pulse. In this study, neon is used as the target gas in the PES chamber. Each XFEL pulse produces a corresponding TOF spectrum, reflecting the intensity distribution of the emitted photoelectrons. When properly calibrated to the kinetic energy domain, the TOF spectra can be used to extract information about the photon energy of the incident pulse.

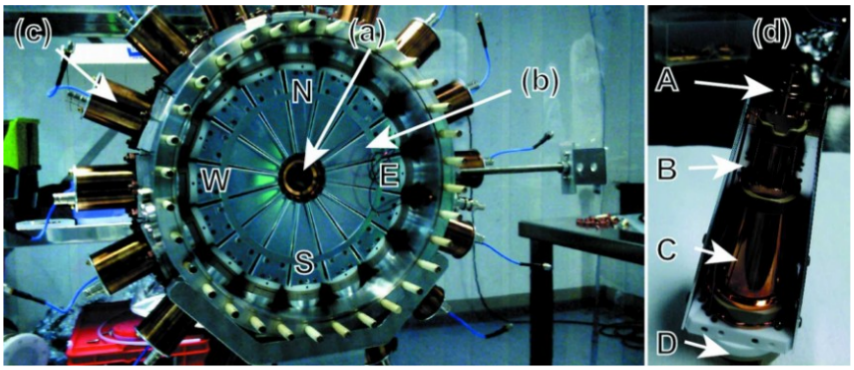

Figure 5.15: PES spectrometer installed in the tunnel, used for measuring the single-shot spectral distribution and polarization of XFEL pulses. The setup consists of an array of 16 TOF spectrometers. An individual TOF spectrometer is shown on the right, with different sections of the drift tube labelled A–D. Image taken from [76] .

Figure 5.16 (a) and (c) show single-shot TOF spectra from representative shots within a pulse train. Due to the uneven distribution of the photoelectron peak around a central value, a Gaussian fit is applied near the expected peak region. The Gaussian fits are shown as orange dotted lines. The peak (maximum) of each Gaussian fit is used to determine the central TOF value corresponding to each single shot, shown in (a) and (c). The distribution of central TOF values from individual shots is presented as a histogram in Figure 5.16 (e). The corresponding energy-calibrated spectra are shown in (b) and (d) alongside the histogram of the kinetic energy distribution in (f).

The kinetic energy extracted from each single-shot spectrum can be directly used to estimate the photon energy of the corresponding FEL pulse based on Equation 2.2. By sorting these photon energy values, one can analyze the distribution of shots for specific photon energies within the range of SASE spectra at the set undulator value. In this analysis, the photon energy is divided into eight bins, allowing for a comparative study of spectral DCH features across different energy regimes due to the SASE energy jitter. Figure 5.17 shows the averaged DCH spectra of shots for three exemplary bins with photon energies directly at (990 eV), lower, and higher than the nominal setpoint, after additional sorting for a multipeak behaviour in the single-shot DCH spectrum. Inset (a) compares the main spectral feature for two photon energies (982 eV and 1000 eV), reproduced based on literature [17]. The red solid line rep-

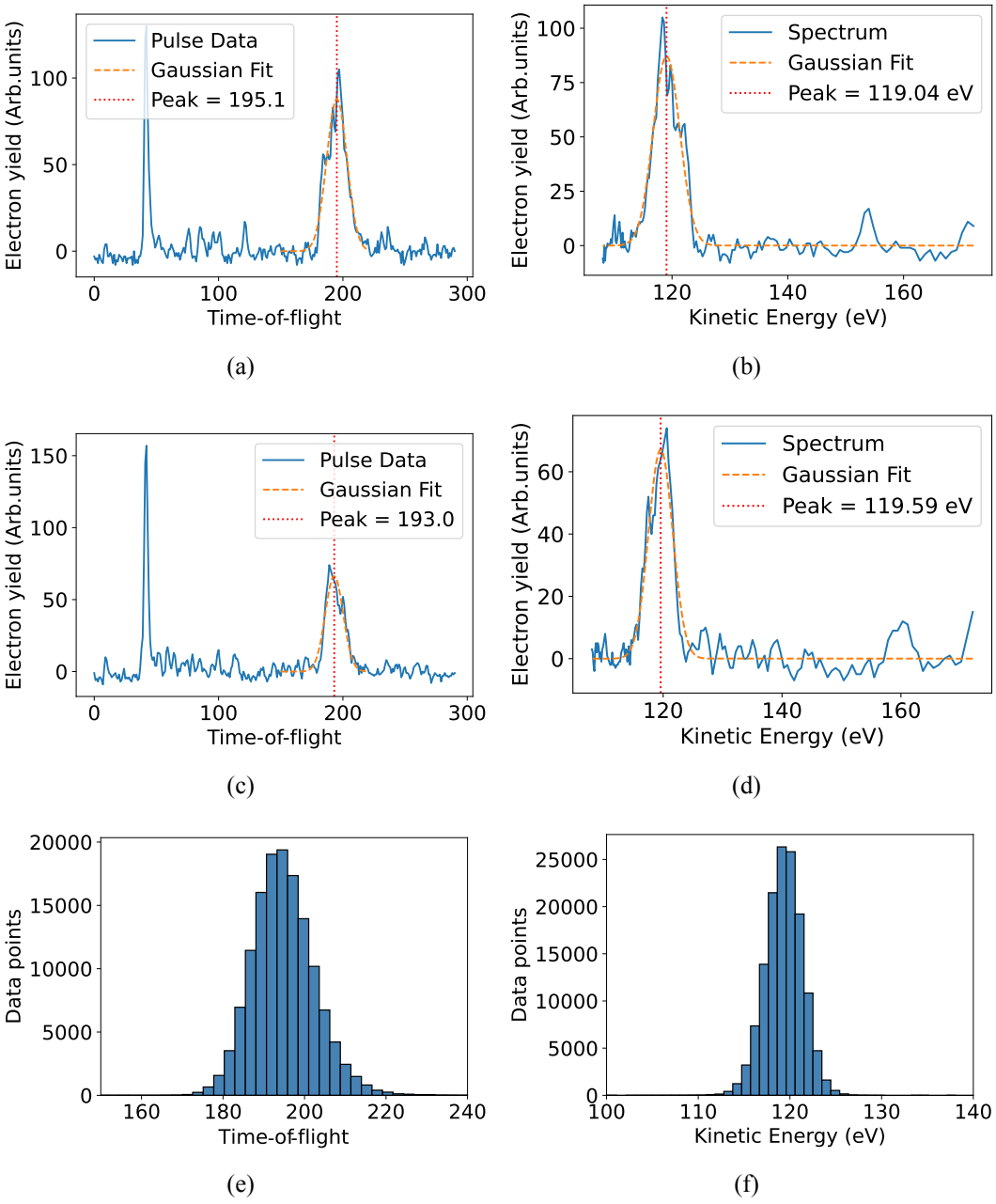

Figure 5.16: PES spectra in the TOF and energy domain. (a) and (c) are the two single-shot spectra in TOF, and the corresponding energy-calibrated spectra are shown in (b) and (d). Plots (e) and (f) show the distributions of time of flight and kinetic energy over the whole data run, respectively.

resents the Gaussian fit corresponding to the resonant excitation of the second core electron into the 3p state at 982 eV, while the orange line indicates the DCH decay channel associated

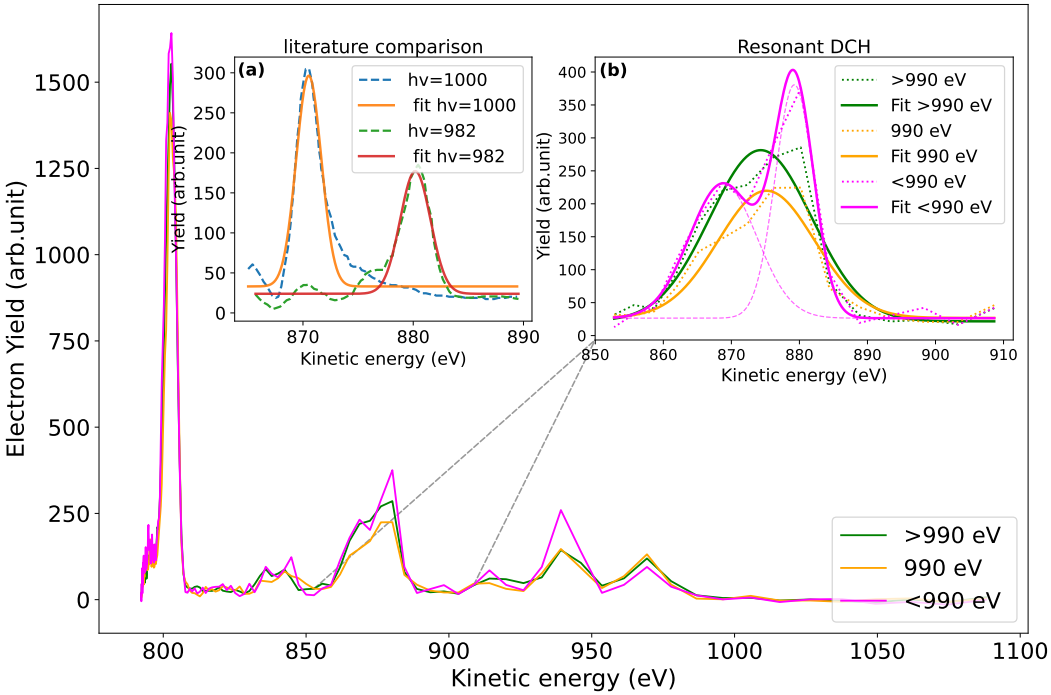

Figure 5.17: DCH spectra obtained with photon energy binning within the XFEL bandwidth using PES. The bins correspond to the central value (990 eV), the lower limit (< 990 eV), and the upper limit (> 990 eV) relative to the photon energy setpoint. Inset (a) compares the main spectral feature for two photon energies (982 eV and 1000 eV), reproduced based on literature [17]. The red solid line represents the Gaussian fit corresponding to the resonant excitation of the second core electron into the 3p state at 982 eV, while the orange line indicates the DCH decay channel associated with the K^{-2} state at a photon energy of 1000 eV. Inset (b) presents a zoomed view of the experimental spectra, highlighting the emergence of the DCH decay channel (magenta) following resonant excitation of a core-shell electron into the 3p state. The Gaussian fits corresponding to the other photon energy bins reveal broader, less-resolved spectral features.

with the K^{-2} state at a photon energy of 1000 eV. Inset (b) presents a zoomed view of the experimental spectra, highlighting the emergence of the DCH decay channel (magenta) following resonant excitation of a core-shell electron into the 3p state around a kinetic energy of 880 eV. The Gaussian fits corresponding to the other photon energy bins reveal broader, less-resolved spectral features. While the overall spectral features remain broad, largely due to the limited resolving power of the TOF spectrometer, under the given experimental conditions, there is a subtle indication of resonant excitation of the core electron into the 3p state in the bin corresponding to $h\nu < 990$ eV. However, for shots with photon energies above this value, the resonant contribution is less distinguishable, likely due to the overlap with broader background features corresponding to the K^{-2} Auger transition or reduced resonance probability at higher energies. This sorting scheme enables selecting pulses that are well aligned to the resonant photon energy and exhibits a characteristic feature corresponding to the resonant Auger DCH decay non-invasively.

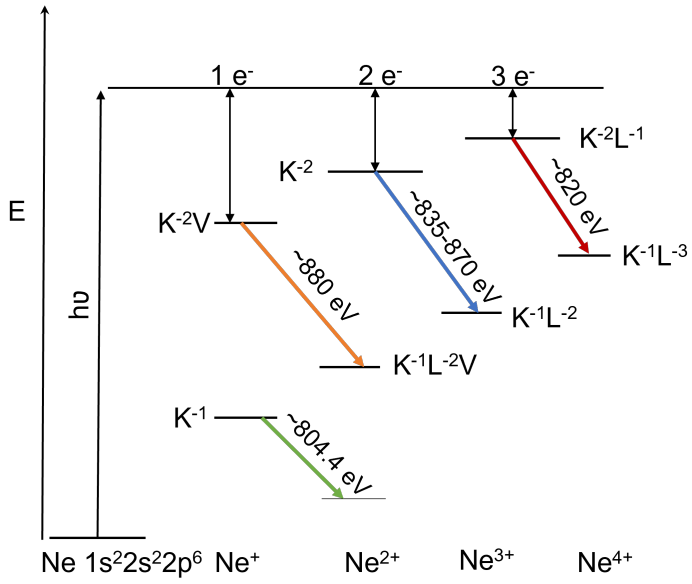

Figure 5.18: Schematic sketch of the Auger processes follow to K^{-1}, K^{-2}, $K^{-2}V$, and $K^{-2}L^{-1}$ ionization. The channel $K^{-1} \rightarrow 2p^{-2}$ is indicated in green, the $K^{-2} \rightarrow K^{-1}L^{-2}$ Auger transition in blue, $K^{-2}V \rightarrow K^{-1}L^{-2}V$ in orange and $K^{-2}L^{-1} \rightarrow K^{-1}L^{-3}$ in red. Recreated based on [165, 166].

The Auger decay of the DCH states is a complex process with multiple relaxation channels. A strong effort is required to disentangle and assign these channels from previous experimental work and theoretical predictions. The decay channel identifications were guided by the high-resolution neon hypersatellite Auger spectra reported by G. Goldsztejn et al. and the

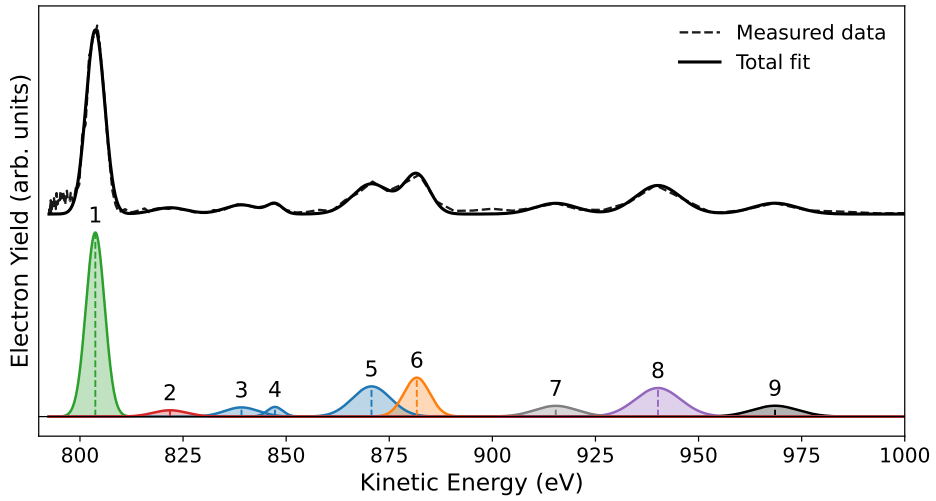

Figure 5.19: Electron spectrum of neon at 990 eV photon energy, where the hypersatellite Auger features are observed alongside photoelectron contributions. The dashed line represents the average of three single-shot data, and the black line is the result of the fitting. Four distinct contributions are evident, as indicated by the different color peaks at the bottom of the figure. The orange [6] peak corresponds to the hyper satellites of $K^{-2}V$ state, blue [3,4,5] peaks correspond to the hypersatellite of K^{-2} states, purple and black [8,9] peaks correspond to the valence ionization of 2s and 2p. The red [2] peak is a hypersatellite of $K^{-2}L^{-1}$ and the strongest peak in green [1] is the $1s^{-1} \rightarrow 2p^{-2}$ Auger transition.

resonance mapping of core-ionized neon atom by T. Mazza et al. [17, 165, 166]. This part primarily focuses on the analysis of the hypersatellite Auger spectrum of the neon atom, excited by 990 eV X-rays via sequential photon absorption.

A schematic picture of possible decay channels following the photoionization of neon within a kinetic energy range is shown in Figure 5.18. The different categories of intermediate states are distinguished by line width, position, and line shape [166]. The assignments made in this section for each of the decay channels are based on the literature [165, 166]. These includes mainly the K^{-1}, K^{-2}, $K^{-2}V$ and $K^{-2}L^{-1}$ where K^{-1} stands for the core-shell ionization and the $K^{-2}V$ state represents the double ionization of the core-shell with one of the electrons being promoted to one of the excited valence states (V = excited state).

Figure 5.19 shows an overview spectrum of the DCH hypersatellite Auger decay of neon together with the $1s^{-1} \rightarrow 2p^{-2}$ SCH Auger decay and direct photoelectrons from the valence ionized states $2p^{-1}$ and $2s^{-1}$. The different contributions from the decay channels of K^{-2}, $K^{-2}V$ and $K^{-2}L^{-1}$ are overlapped in the spectrum. Multiple individual fits are performed within the expected kinetic energy range to distinguish each of these states. They are shown in different colors for each state, along with a corresponding number. The spectral fitting was

Peak	Kinetic energy (eV)	Hole type	Assignment	Reference (eV)
1	803.7	K^{-1}	$1s^{-1} \rightarrow 2p^{-2}$	804.4
2	821.8	$K^{-2}L^{-1}$	$1s^{-2}2p^{-1} \rightarrow 1s^{-1}2s^{-1}2p^{-2}$	819.1
3	839.1	K^{-2}	$1s^{-2} \rightarrow 1s^{-1}2s^{-1}2p^{-1}{}^1P^0({}^2P^0)$	838.4
4	847.3	K^{-2}	$1s^{-2} \rightarrow 1s^{-1}2s^{-1}2p^{-1}{}^3P^0({}^2P^0)$	844.4
5	870.7	K^{-2}	$1s^{-2} \rightarrow 1s^{-1}2p^{-2}({}^2D)$	870.4
6	881.6	$K^{-2}V$	$1s^{-2}3p^1 \rightarrow 1s^{-1}2p^{-2}({}^2D)3p^1$	880.6

Table 5.1: Overview of the observed Auger transitions, including the assignment. The measured value of kinetic energy is compared with the values of reference [165]. The peak numbers are marked in Figure 5.19.

performed using a Gaussian peak model, where the tail after the valence ionization peak was taken as the effective baseline. Regions of interest (ROIs) and approximate peak positions were manually defined to provide initial parameters for the fitting routine. A least-squares minimization was then applied to optimize the peak amplitudes, positions, and widths. After the fit, the residual spectrum was calculated as the difference between the experimental data and the reconstructed fit. The residuals were found to be small and symmetrically distributed around zero, indicating that the fitting procedure accurately reproduced the measured spectrum and validating the reliability of the extracted peak parameters.

Peak	Kinetic energy (eV)	Assignment	Reference (eV)
7	915.7	$2s^{-1} \rightarrow 2s^{-2}$	916.6
8	940.3	$2s^2 \rightarrow 2s^{-1}$	941.5
9	969.1	$2p^6 \rightarrow 2p^{-5}$	968.3

Table 5.2: Overview of the observed photoelectron transitions, including the assignment. The measured value of kinetic energy is compared with the values of reference [117] for a photon energy of 990 eV. The peak numbers are marked in Figure 5.19.

The Auger decays of different intermediate states are described as follows, the $K^{-2} \rightarrow K^{-1}L^{-2}$ in blue (peaks 3,4,5), $K^{-2}V \rightarrow K^{-1}L^{-2}V$ in orange (peak 6), $K^{-2}L^{-1} \rightarrow K^{-1}L^{-3}$ in red (peak 2), valence photoionization of nuetral neon atom $2s^{-1}$ and $2p^{-1}$ in purple and black (peak 8,9), respectively, and the $1s^{-1} \rightarrow 2p^{-2}$ in green (peak 1). Peak 7, in light grey, corresponds to the ionization of the 2s electron from a Ne^+ ion. Table 5.1 gives more information about the individual Auger transition assignments and the kinetic energies of each of these states, along with the possible final state. Previous synchrotron measurements where the DCH states is achieved with a direct double ionization of core-shell at a photon energy of 2.3 keV, determined the kinetic energies of the two closely overlapping resonant states,

$1s^{-2}3p^1$ and $1s^{-2}3s^1$, to be 880.5 eV and 881.5 eV, respectively [166]. The measurements reported here were acquired at the Eu-XFEL using a TOF spectrometer with moderate energy resolution settings, which does not permit these states to be resolved individually. Instead, they appear as a single broadened peak. Following T. Mazza et al. [17], who mapped the resonant states in core-ionized neon with a high-resolution TOF spectrometer at the Eu-XFEL, and given the close similarity of the experimental conditions, we assign the peak at 881.6 eV to the $1s^{-2}3p^1$ state.

Table 5.2 provides an overview of the photoelectron peaks from neutral and singly ionized target atoms. The peak assignments are based on the measured kinetic energy values and the relative intensities of the individual features. The spectral contribution associated with the $2s^{-1}$ state exhibits nearly twice the yield compared to the $2p^{-1}$ state, since the photoabsorption cross-section of the 2s orbital is higher than that of the 2p orbital at this photon energy [117].

The spectra shown in Figure 5.19 represent the average of three single-shot spectra. Although this reduces statistical accuracy, it is nevertheless highly useful for pulse-resolved studies of transient atomic and molecular systems. The method of sorting single-shot spectra using an independent spectroscopic tool, which offers a higher degree of correlation, is particularly remarkable.

5.8 Reconstructed Spectral Correlation with PES

The angular streaking setup described in Section 5.2 enables single-shot retrieval of the X-ray pulse duration for all streaked events. When using the extracted pulse duration to interpret and validate physical phenomena, such as DCH formation, the reliability and robustness of the reconstruction method become essential. This section evaluates the consistency and credibility of the spectral reconstruction obtained through angular streaking. To support this analysis, correlation measurements are performed using the PES installed in the tunnel, providing an independent diagnostic reference.

A direct correlation between the photoelectron spectra from the PES and the reconstructed pulse characteristics is not always straightforward or intuitive. However, since both the photoelectron spectra and the reconstructed XFEL pulse originate from the same X-ray pulse, even though they are observed through different diagnostics and at different times, an intrinsic connection must exist between them. Understanding this relationship is crucial for validating the spectral reconstruction and gaining a deeper insight into the characterization of the temporal and spectral properties of the XFEL pulse using this method.

Multiple machine settings were employed during the measurement campaign to assess the robustness and applicability of the pulse reconstruction scheme across varying experimental conditions. One such configuration was the short-pulse scheme, in which the majority of the generated XFEL pulses had durations of less than one femtosecond. The detailed machine parameters used to achieve these ultrashort pulses are beyond the scope of this discussion and will not be elaborated upon here. The photon energy set value for this particular data run is 990 eV. The dataset used for reconstruction comprises 9147 pulse trains, each containing 15 shots. Among these, only the even-numbered shots were subjected to streaking and subsequent reconstruction. These even-numbered shots are selectively used to correlate with the PES measurements, assessing consistency between the two diagnostics.

The correlation measurement is performed following a series of preprocessing steps applied to the full dataset. This includes selecting an appropriate pulse energy window and filtering based on the strength of the streaking kick. The pulse energy values in the dataset range from 0 μJ to 420 μJ. A window between 120 μJ and 170 μJ is chosen, as selecting a single fixed value doesn't give enough statistics. This range ensures that the pulse energy is sufficiently high to observe meaningful streaking effects while also retaining a statistically significant number of shots for analysis.

The second level of sorting is based on the streaking kick, which serves as a critical qual-

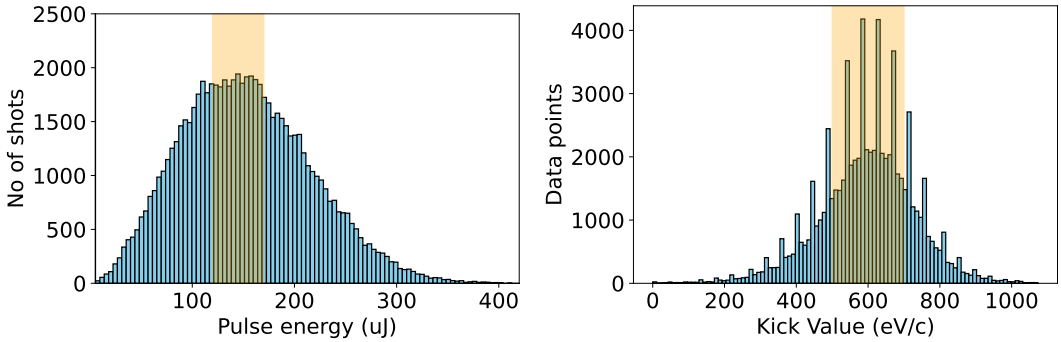

Figure 5.20: Sorting of pulses by applying thresholds on pulse energy and the streaking kick. The highlighted regions in the two plots indicate the selected ranges used for filtering shots, which are represented in orange.

ity criterion for determining the strength and reliability of the streaking effect. The streaking kick refers to the momentum transfer imparted to the photoelectrons by the circularly polarized laser field. It is directly related to the vector potential of the streaking pulse at the moment of ionization. A well-defined and sufficiently strong streaking kick is essential for accurately reconstructing the temporal profile of the X-ray pulse. A streaking kick window of 500 eV/c – 700 eV/c is selected for this analysis. This range ensures that the streaking effect is strong enough to produce a precise angular modulation in the photoelectron spectrum while avoiding extremely high values that may introduce nonlinearities or reduce resolution. Only those shots falling within this defined kick range are considered for the correlation with PES measurements, ensuring consistency and reliability in the reconstructed pulse characteristics. Figure 5.20 shows the sorting of the pulse energy region and the desired kick for this particular analysis.

In addition to the sorting procedures described above, a consistency check was performed by analyzing the pulse energy dependence of the signals from both diagnostic detectors, the PES spectrometer, and the angular streaking setup. The electron yield from both detecting systems exhibited similar trends as a function of pulse energy, confirming that the corresponding measurements are linked to the same physical events. To further validate this, the unique identification numbers assigned to each XFEL pulse train, known as train IDs, were cross-checked. Matching train IDs between the two diagnostics tools ensures that the selected shots being compared indeed originate from the same pulse trains. This verification step is essential for establishing the integrity of the correlation analysis between the two independent measurement systems.

The reconstructed XFEL pulse is derived from the spectrogram of each streaked shot, and

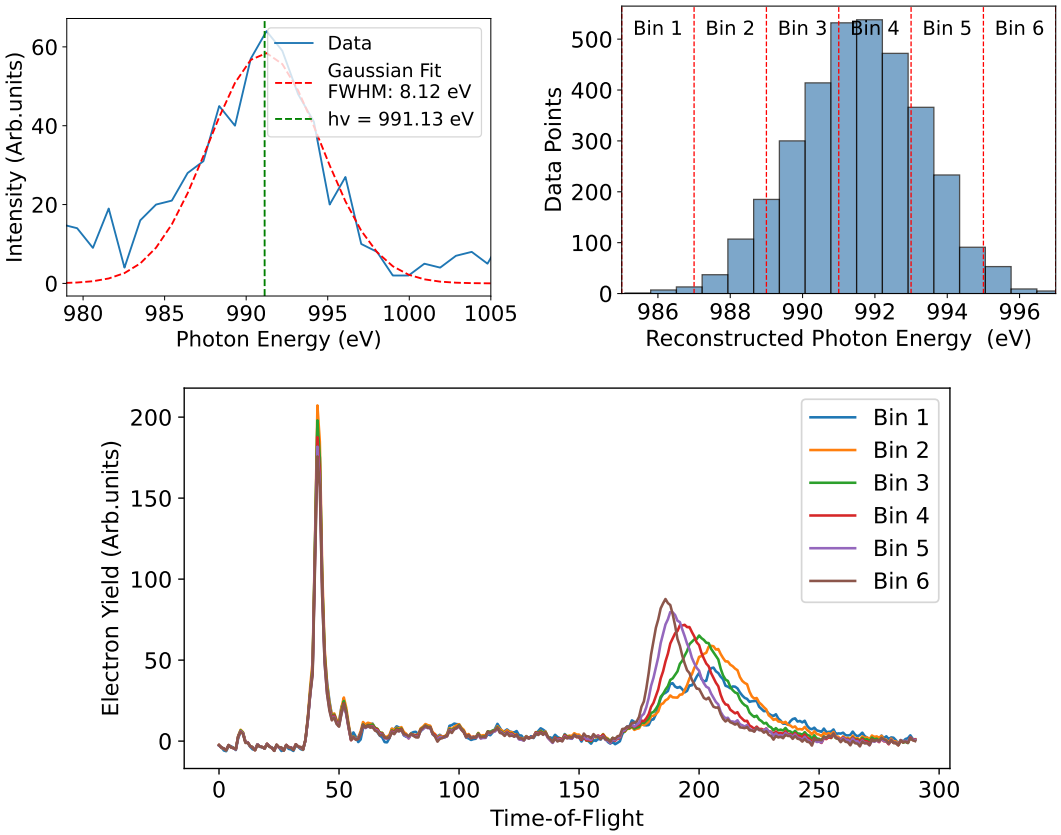

(a)

Figure 5.21: Correlation of the reconstructed FEL spectra with the PES spectrometer. (a) Reconstructed X-ray spectrum obtained from the streaking analysis, with the central photon energy determined from the peak of a Gaussian fit. (b) Photon energy distribution of the valid reconstructed shots. (c) Corresponding average photoelectron spectra in TOF from the PES, grouped according to each photon energy bin.

an example spectrum for a selected shot is shown in Figure 5.21 (a). Each reconstructed spectrum exhibits the characteristic spiky intensity structure, a distinct feature of SASE-FEL pulses. The central photon energy obtained from both methods is compared to determine if there is a meaningful correlation between the pulse reconstruction and the PES measurement.

For this purpose, a Gaussian fit is applied to the reconstructed XFEL spectrum, as illustrated by the red dashed line in Figure 5.21 (a). The center of this Gaussian fit estimates the central photon energy for that particular shot. Since the typical bandwidth of the XFEL pulse is not expected to exceed 10 eV, an additional quality filter is applied. If the FWHM of the Gaussian fit exceeds 10 eV, the shot is excluded from further analysis. This ensures that only physically reasonable reconstructions with spectral widths consistent with known XFEL pa-

rameters are considered. This filtering step, combined with the earlier sorting criteria, helps retain a statistically significant and reliable set of shots for a robust correlation between the reconstructed spectra and the PES data.

Figure 5.21 (b) presents the distribution of photon energies obtained from the reconstructed XFEL spectra as a histogram. This histogram represents the central photon energy values extracted from individual shots using Gaussian fits to the reconstructed spectra, as described earlier. Since the photoelectron spectra are highly sensitive to the photon energy of the incident X-ray pulses, a corresponding analysis is performed on the PES spectra. To explore this sensitivity, the PES data are grouped into different photon energy bins based on the values obtained from the reconstruction. By comparing the PES spectra across these bins, one can examine how variations in photon energy influence the photoelectron signal. This binning approach enables a more general correlation between the reconstructed XFEL pulse characteristics and the PES response through averaging. The previous section, 5.6, discussed the photon energy estimate from the PES. Figure 5.21 (c) shows the shift in the TOF spectrum of PES corresponding to each bandwidth bin.

This shift in the average photoelectron spectra across the photon energy bins, estimated from the reconstruction, helps verify that the analysis scheme is functioning correctly. However, one can compare the photon energies of selected individual shots from both methods to establish a more direct and quantitative correlation measure. Figure 5.22 (a) presents the correlation plot of these individual shots, with error margins included. An overall correlation coefficient of 0.59 is obtained, which serves as a quantitative indicator of the method's robustness.

This analysis is primarily conducted on a data run where the pulse durations range from 0.74 fs to 6 fs, with 80% of the shots having durations below 2.5 fs. For comparison, a separate data run acquired in "long pulse" mode is used, where the estimated pulse durations span from 0.74 fs to 10 fs and are more evenly distributed. Figure 5.22 (c) shows the correlation between the reconstructed spectral center and the corresponding PES photon energy for a data run with longer and more spiky XFEL spectra. An overall correlation of 0.34 is observed for the "long pulse" mode due to the lower statistics after sorting and a highly spiky individual reconstructed spectrum. Checking this correlation across different pulse duration settings enables a meaningful comparison between reconstruction robustness in different pulse modes.

Figure 5.23 presents the results of a detailed analysis of how pulse duration affects the correlation in the reconstructed spectrum to PES. The photon energy correlation is evaluated across different pulse duration bins. This illustrates how the correlation coefficient varies with the estimated pulse duration. Multiple schemes are considered to compare the performance

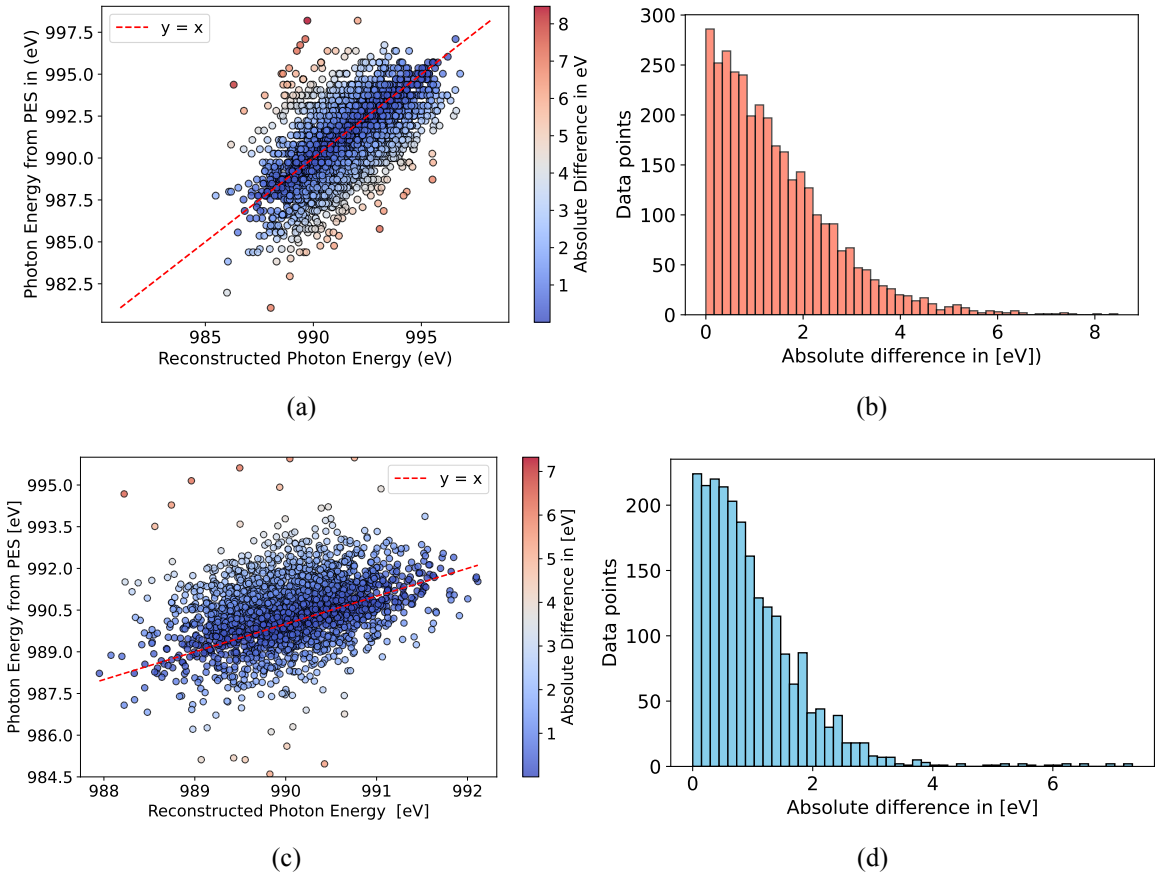

Figure 5.22: The reconstructed spectral correlation with the PES. (a) Shows the one-to-one correlation of the photon energy estimated from the reconstructed spectrum to the PES photon energy on the single-shot scale for a short pulse mode, where the individual pulse duration of the XFEL shots is not more than 4 fs. The red dotted line shows the linear correlation; the absolute deviation from this line is plotted in (b). The correlation and absolute deviation for a data run with comparatively longer X-ray pulses, estimated to have a duration of up to 10 fs, are shown in (c) and (d).

of different central photon energy estimation methods, including the centroid, Gaussian fit, median, and a centroid-based Gaussian fit. While these schemes yield slightly different correlation values, the overall correlation remains strong and comparable across all methods. The relatively low correlation observed at longer pulse durations is due to the limited number of shots with sufficient pulse energy and to the streaking kick, which follows a Gaussian envelope for the spectral components.

One of the primary challenges in this analysis lies in accurately estimating the photon energy from the reconstructed X-ray pulses, primarily due to their inherently spiky spectral structure. Among the various methods tested, fitting a single Gaussian envelope across the spectrum proved to be the most efficient and robust approach. This method yields more reliable results for spectra with a dominant single peak than those with multiple spiky features. The short pulse mode predominantly produces spectra with a Gaussian-like intensity envelope over the spectral bandwidth, facilitating more straightforward photon energy estimation and enabling stronger correlation with external measurements. In contrast, long pulse mode typically results in non-Gaussian envelopes, making it more challenging to determine a representative central photon energy. Nevertheless, the absolute deviation from linear correlation in photon energy estimation remains mostly within 2 eV, which is acceptable considering the inherent uncertainties in energy calibration. These findings provide an important valida-

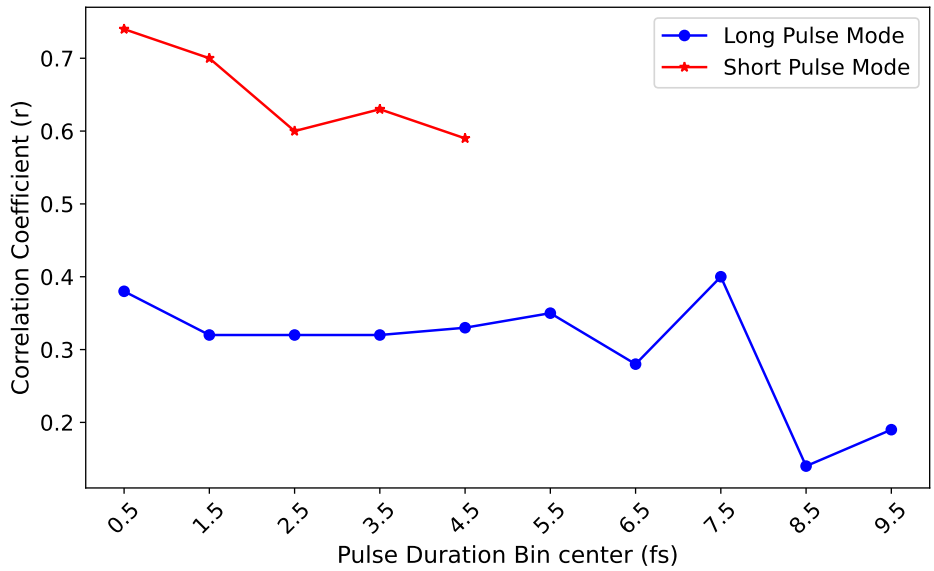

Figure 5.23: Reconstructed spectral correlation of XFEL with PES as a function of pulse duration. The correlation is high (≈ 0.7) for the short pulse mode. The correlation coefficient is ≈ 0.32 for the longer pulse mode, and gets even weaker within this mode, when the pulses are long.

tion step for the spectral reconstruction method based on angular streaking, which has not been previously cross-checked in this manner. By correlating the reconstructed central photon energy with independent PES measurements, this analysis offers a practical benchmark for evaluating the robustness and reliability of the reconstruction scheme. While the method does not provide direct information about the detailed spectral structure, such as the number or shape of spikes in a SASE pulse, it proves to be an effective tool for assessing the accuracy of the reconstructed central photon energy. This, in turn, allows for filtering and selecting shots with physically meaningful spectral profiles, which is critical when using reconstructed spectra for further quantitative analysis. The approach demonstrated here can thus serve as a quality control criterion in future experiments that utilize angular streaking for spectral-temporal diagnostics. It shows that even with the inherent noise and variability of single-shot SASE spectra, a consistent correlation with an independent diagnostic confirms the method's reliability, especially in identifying and utilizing FEL pulses with clean, interpretable spectral shapes.

Chapter 6

Conclusion

In my thesis, I have investigated the phenomenon of photoabsorption in neon by high-intensity X-ray radiation pulses of ultrashort duration. The experiments were made feasible by the instrument capabilities present at X-ray free-electron lasers, together with novel techniques for the single-shot detection and characterization of the FEL attosecond X-ray pulses and the generated electron emission patterns in the target. In addition to designing and constructing new components for these detectors, I set up an entirely new array of such detectors in the form of a highly versatile angle-resolved electron spectrometer. In addition, we implemented this spectrometer as an instrument at the European XFEL. We demonstrated its applicability in a multitude of measurements, including X-ray pulse spectral and temporal features, X-ray polarization patterns, and ultrafast electron excitation, ionization, and relaxation processes in gaseous neon.

This work lays the groundwork for a comprehensive investigation of intensity-dependent nonlinear photoabsorption and subsequent relaxation dynamics in gaseous neon atoms using XFELs. These fourth-generation light sources, characterized by their ability to produce intense, ultrashort pulses, provide unprecedented access to ultrafast electron dynamics. The Eu-XFEL at Schenefeld, with its high peak brilliance and wide wavelength tunability, generates pulses shorter than a few femtoseconds. These capabilities uniquely position it to investigate previously inaccessible regimes of nonlinear photoabsorption and core-shell electron interactions.

A fundamental limiting factor of SASE-based XFEL sources, however, lies in the stochastic nature of individual pulses. Each pulse differs significantly in both spectral content and temporal structure, necessitating robust diagnostic methods that can resolve single-pulse characteristics. Given the high cost and limited availability of FEL beamtime, it becomes imper-

ative to maximize information retrieval from each shot. This thesis addresses that need by presenting a detailed single-shot characterization, specifically targeting nonlinear phenomena such as DCH formation in neon.

The first major result is the demonstration of intensity-dependent, single-shot DCH characterization in neon atoms. Leveraging the focused X-ray beam ($\approx 2\mu$m) and high pulse energies (up to hundreds of microjoules), we achieved peak intensities exceeding 10^{17} W/cm^2. These conditions are sufficient to drive sequential two-photon absorption processes, leading to the formation of DCH states. Importantly, this was achieved and resolved on a single-shot basis, providing direct insight into the transient evolution of highly excited atomic configurations. The observed correlation between electron yield and pulse energy on a per-shot basis highlights the role of pulse intensity in governing nonlinear ionization pathways.

The observed increase in DCH signal with pulse energy, eventually reaching levels comparable to SCH yields, implies that a substantial fraction of atoms undergo DCH formation under high-intensity conditions. Single-shot spectra, in contrast to averaged spectra, reveal a rich variability and provide access to ultrafast processes that would otherwise remain obscured.

The second key outcome of this work is the validation of the spectral reconstruction from angular streaking. By correlating reconstructed photon energies with independent data from a photoelectron spectrometer, we confirmed the robustness of this technique. Although the method does not account for fine spectral features, such as the SASE spike structure, it effectively tracks the central photon energy of each pulse. This is essential for filtering and selecting meaningful shots for quantitative analysis. The ability to cross-validate reconstructed spectra with physical observables enhances confidence in using angular streaking as a spectral-temporal diagnostic tool.

Another key observation is the sorting of resonant states based on the bandwidth binning of XFEL pulses. The broad spectral components associated with the ultrashort special mode of operation made it challenging to clearly resolve the resonant states. However, by sorting the shots according to bandwidth bins using the PES, distinct resonant states become evident. Furthermore, the pulse duration–dependent analysis of the enhanced DCH yield at a fixed pulse energy window indicates an increase in photon flux, thereby supporting the independently estimated pulse duration measurements.

In conclusion, this thesis presents a successful characterization of individual XFEL pulses and the single-shot observation of ultrafast, highly transient states in neon. An angle-resolving spectrometer assembly, developed as part of this work, has been developed, commissioned, and installed at the Eu-XFEL for providing pulse diagnostics during the user beamtimes.

These contributions collectively enhance our ability to probe and understand nonlinear X-ray matter interactions, thereby facilitating future time-resolved studies that require precise control and measurement of ultrashort light pulses. The methodologies developed here set the foundation for future pump-probe experiments using FEL, enabling real-time tracking of electron dynamics in atoms and molecules with unparalleled temporal resolution. Looking ahead, work is ongoing to utilize machine learning tools to help estimate pulse duration in real-time. These tools could support the current diagnostic methods and make it faster to reconstruct pulses. Although still under development, this approach shows promise for enhancing experimental control and maximizing the use of beam time at XFEL facilities.

Bibliography

[1] T. H. Maiman. Stimulated optical radiation in ruby. *Nature*, 187:493–494, 1960.

[2] F. Krausz and M. Ivanov. Attosecond physics. *Reviews of Modern Physics*, 81:163, 2009.

[3] T. Brabec and F. Krausz. Intense few-cycle laser fields: Frontiers of nonlinear optics. *Reviews of Modern Physics*, 72:545, 2000.

[4] E. Goulielmakis et al. Real-time observation of valence electron motion. *Nature*, 466:739–743, 2010.

[5] L. S. Cederbaum, J. Zobeley, and F. Tarantelli. Interatomic coulombic decay: A new decay mechanism for excited atoms in clusters. *Physical Review Letters*, 79:4778, 1997.

[6] T. Morishita et al. Theory of attosecond transient absorption spectroscopy of atoms. *Physical Review A*, 77:053414, 2008.

[7] P. Emma et al. First lasing and operation of an ångstrom-wavelength free-electron laser. *Nature Photonics*, 4:641–647, 2010.

[8] J. Andruszkow et al. First observation of self-amplified spontaneous emission in a free-electron laser at 109 nm wavelength. *Physical Review Letters*, 85:3825–3829, 2000.

[9] M. Altarelli, R. Brinkmann, and M. Chergui. The european x-ray free-electron laser. technical design report, Jul 2007.

[10] P. Emma et al. First lasing and operation of an ångstrom-wavelength free-electron laser. *Nature Photonics*, 4:641–647, 2010.

[11] T. Ishikawa et al. Sacla: The compact xfel facility in japan. *Nature Photonics*, 6:540–544, 2012.

[12] C. Pellegrini and J. Stöhr. X-ray free-electron lasers—principles, properties and applications. *Nuclear Instruments and Methods in Physics Research Section A: Accelerators, Spectrometers, Detectors and Associated Equipment*, 500(1):33–40, 2003. NIMA Vol. 500.

[13] M. Altarelli et al. The european x-ray free-electron laser technical design report. *DESY Report*, 2007.

[14] W. Helml. *Development & Characterization of Sources for high-energy, high-intensity coherent Radiation*. PhD thesis, Technische Universität München, 2012.

[15] J. Itatani et al. Attosecond streak camera. *Physical Review Letters*, 88:173903, 2002.

[16] A. L. Cavalieri et al. Attosecond spectroscopy in condensed matter. *Nature*, 449:1029–1032, 2007.

[17] T. Mazza, M. Ilchen, M. D. Kiselev, E. V. Gryzlova, T. M. Baumann, R. Boll, A. De Fanis, P. Grychtol, J. Montaño, V. Music, Y. Ovcharenko, N. Rennhack, D. E. Rivas, Ph. Schmidt, R. Wagner, P. Ziolkowski, N. Berrah, B. Erk, P. Johnsson, C. Küstner-Wetekam, L. Marder, M. Martins, C. Ott, S. Pathak, T. Pfeifer, D. Rolles, O. Zatsarinny, A. N. Grum-Grzhimailo, and M. Meyer. Mapping resonance structures in transient core-ionized atoms. *Phys. Rev. X*, 10(4):041056, Dec 2020.

[18] N. Bohr. On the constitution of atoms and molecules. *Philosophical Magazine*, 26:1–25, 1913.

[19] E. Schrödinger. An undulatory theory of the mechanics of atoms and molecules. *Physical Review*, 28:1049–1070, 1926.

[20] W. Pauli. Zur quantenmechanik des magnetischen elektrons. *Zeitschrift für Physik*, 31:765, 1925.

[21] R. Belford. General chemistry i: The shapes of atomic orbitals. https://chem.libretexts.org/Courses/University_of_Arkansas_Little_Rock/Chem_1402:_General_Chemistry_1_(Belford)/Text/6:_The_Structure_of_Atoms/6.6:_The_Shapes_of_Atomic_Orbitals, n.d. Accessed: July 7, 2023.

[22] T. E. Brown, H. E. LeMay, B. E. Bursten, C. J. Murphy, and P. M. Woodward. *Chemistry: The Central Science*. Pearson, 14 edition, 2020.

[23] F. Hund. The interelectronic repulsion and the spin multiplet structure. *Zeitschrift für Physik*, 40:742–748, 1927.

[24] A. Einstein. Über einen die erzeugung und verwandlung des lichtes betreffenden heuristischen gesichtspunkt. *Annalen der Physik*, 322:132–148, 1905.

[25] M. Planck. Über irreversible strahlungsvorgänge. *Sitzungsberichte der Preußischen Akademie der Wissenschaften*, 5:480–497, 1899.

[26] X-ray data booklet. https://xdb.lbl.gov/, 2009. Center for X-ray Optics and Advanced Light Source, Lawrence Berkeley National Laboratory; updated October 2009.

[27] A. Thompson et al. *X-ray Data Booklet*. Lawrence Berkeley National Laboratory, University of California Berkeley, Berkeley, CA, 2009.

[28] W. Decking et al. A mhz-repetition-rate hard x-ray free-electron laser driven by a superconducting linear accelerator. *Nature Photonics*, 14:391–397, 2020.

[29] L. Meitner. The β radiation spectrum of ux_1 and its interpretation. *Zeitschrift für Physik*, 17:54–66, 1923.

[30] P. Auger. Sur les rayons β secondaires produits dans un gaz par des rayons x. *Comptes Rendus Hebdomadaires des Séances de l'Académie des Sciences*, 177:169–171, 1923.

[31] M. O. Krause and J. H. Oliver. Natural widths of atomic k and l levels, kα x-ray lines and several kll auger lines. *Journal of Physical and Chemical Reference Data*, 8:329–338, 1979.

[32] M. O. Krause. Atomic radiative and radiationless yields for k and l shells. *Journal of Physical and Chemical Reference Data*, 8:307–327, 1979.

[33] V. Music. *Towards the investigation of ultrafast dynamics in chiral systems using free-electron lasers*. Dissertation for the degree of doctor of natural sciences - dr. rer. nat., University of Kassel, Germany, 2023.

[34] J. H. Eberly, J. Javanainen, and K. Rzążewski. Above-threshold ionization. *Physics Reports*, 204:331–383, 1991.

[35] A. G. Kochur and V. A. Popov. Shake up and shake off probabilities for l-, m-, and n-electrons in atoms with z=3 to 60. *Radiation Physics and Chemistry*, 75:1525–1528, 2006.

[36] T. A. Carlson, C. W. Nestor, T. C. Tucker, and F. B. Malik. Calculation of electron shake-off for elements from $z = 2$ to 92 with the use of self-consistent-field wave functions. *Physical Review*, 169:27–36, 1968.

[37] T. A. Carlson. *Photoelectron and Auger Spectroscopy*. Modern Analytical Chemistry. Springer, New York, 1975.

[38] D. Rolles, T. Möller, and U. Becker. Scattering and coherence phenomena in the photoionization of small molecules. 2005.

[39] M. Ilchen. *Coherence Effects in the Valence Photoionization of Small Molecules*. PhD thesis, Technische Universität Berlin, Fakultät II – Mathematik und Naturwissenschaften, 2012.

[40] E. Fermi. Quantum theory of radiation. *Reviews of Modern Physics*, 4:87–132, 1932.

[41] U. Becker and D.A. Shirley. Vuv and soft x-ray photoionization. In U. Becker and D.A. Shirley, editors, *VUV and Soft X-Ray Photoionization*, page 135. Plenum Press, New York, 1996.

[42] W. F. Chan, G. Cooper, X. Guo, G. R. Burton, and C. E. Brion. Absolute optical oscillator strengths for the electronic excitation of atoms at high resolution. iii. the photoabsorption of argon, krypton, and xenon. *Physical Review A*, 46:149–171, 1992.

[43] W. F. Chan, G. Cooper, X. Guo, and C. E. Brion. Absolute optical oscillator strengths for the electronic excitation of atoms at high resolution. ii. the photoabsorption of neon. *Physical Review A*, 45:1420–1433, 1992.

[44] J. Cooper and R. N. Zare. Angular distribution of photoelectrons. *The Journal of Chemical Physics*, 48:942–943, 1968.

[45] S. T. Manson and A. F. Starace. Photoelectron angular distributions: energy dependence for *s* subshells. *Reviews of Modern Physics*, 54:389–405, 1982.

[46] T. Hayaishi and P. Zimmerman. Vuv- and soft x-ray photoionization. In U. Becker and D. A. Shirley, editors, *VUV- and Soft X-ray Photoionization*. Plenum Press, New York, 1996.

[47] G. C. King and K.-H. Schartner. Vuv- and soft x-ray photoionization. In U. Becker and D. A. Shirley, editors, *VUV- and Soft X-ray Photoionization*. Plenum Press, New York, 1996.

[48] J. A. R. Samson. Many-body theory of atomic structure and photoionization. In T. N. Chang, editor, *Many-body Theory of Atomic Structure and Photoionization*. World Scientific, Singapore, 1993.

[49] O. Hemmers et al. Nondipole effects in the photoionization of xe $4d_{5/2}$ and $4d_{3/2}$: Evidence for quadrupole satellites. *Physical Review Letters*, 93:113001, 2004.

[50] O. Hemmers, R. Guillemin, E. P. Kanter, B. Krässig, D. W. Lindle, S. H. Southworth, R. Wehlitz, J. Baker, A. Hudson, M. Lotrakul, D. Rolles, W. C. Stolte, I. C. Tran, A. Wolska, S. W. Yu, M. Ya. Amusia, K. T. Cheng, L. V. Chernysheva, W. R. Johnson, and S. T. Manson. Dramatic nondipole effects in low-energy photoionization: Experimental and theoretical study of xe 5s. *Physical Review Letters*, 91:053002, 2003.

[51] B. McNeil and N. Thompson. X-ray free-electron lasers. *Nature Photonics*, 4:814–821, 2010.

[52] C. Pellegrini, A. Marinelli, and S. Reiche. The physics of x-ray free-electron lasers. *Rev. Mod. Phys.*, 88(1):015006, Mar 2016.

[53] L. Young et al. Roadmap of ultrafast x-ray atomic and molecular physics. *Journal of Physics B: Atomic, Molecular and Optical Physics*, 51:032003, 2018.

[54] M. Ilchen, E. Allaria, P. Rebernik Ribivc, H. D. Nuhn, A. A. Lutman, E. Schneidmiller, M. Tischer, M. Yurkov, M. Calvi, E. Prat, S. Reiche, T. Schmidt, G. A. Geloni, S. Karabekyan, J. Yan, S. Serkez, Z. Gao, B. Deng, C. Feng, H. Deng, W. Helml, L. Funke, M. Larsson, V. Zhaunerchyk, M. Meyer, T. Mazza, T. Jahnke, R. Doerner, F. Calegari, O. Smirnova, C. Vozzi, G. De Ninno, J. Waetzel, J. Berakdar, S. Bari, L. Schwob, J. R. Rouxel, S. Mukamel, K. Bartschat, K. R. Hamilton, L. Argenti, N. Douguet, N. M. Novikovskiy, P. V. Demekhin, and P. Walter. Opportunities for gas-phase science at short-wavelength free-electron lasers with undulator-based polarization control. 2023.

[55] W. Zinth, A. Laubereau, and W. Kaiser. The long journey to the laser and its rapid development after 1960. *European Physical Journal H*, 36:153–181, Sep 2011.

[56] T. H. Maiman. Stimulated optical radiation in ruby. *Nature*, 187:493–494, 1960.

[57] S. Suckewer, C. H. Skinner, H. Milchberg, C. Keane, and D. Voorhees. Amplification of stimulated soft x-ray emission in a confined plasma column. *Phys. Rev. Lett.*, 55:1753–1756, Oct 1985.

[58] C. Pellegrini. The history of x-ray free-electron lasers. *The European Physical Journal H*, 37, 10 2012.

[59] C. Pellegrini and Sven Reiche. The development of x-ray free-electron lasers. *Selected Topics in Quantum Electronics, IEEE Journal of*, 10:1393 – 1404, 12 2004.

[60] T. Shaftan. Synchrotron radiation (lecture 2). Brookhaven National Laboratory.

[61] A. M. Kondratenko and E. L. Saldin. Generating of coherent radiation by a relativistic electron beam in an undulator. 1980.

[62] R. Bonifacio, C. Pellegrini, and L. M. Narducci. Collective instabilities and high-gain regime in a free electron laser. *Optics Communications*, 50(6):373–378, 1984.

[63] J. B. Murphy, C. Pellegrini, and R. Bonifacio. Collective instability of a free electron laser including space charge and harmonics. *Optics Communications*, 53(3):197–202, 1985.

[64] J. M. J. Madey. Stimulated emission of bremsstrahlung in a periodic magnetic field. *Journal of Applied Physics*, 42:1906–1913, 1971.

[65] W. Ackermann et al. Operation of a free-electron laser from the extreme ultraviolet to the water window. *Nature Photonics*, 1:336–342, 2007.

[66] J Feldhaus. Flash—the first soft x-ray free electron laser (fel) user facility. *Journal of Physics B: Atomic, Molecular and Optical Physics*, 43(19):194002, sep 2010.

[67] T. Ishikawa et al. A compact x-ray free-electron laser emitting in the sub-ångström region. *Nature Photonics*, 6:540–544, 2012.

[68] E. Allaria et al. Highly coherent and stable pulses from the fermi seeded free-electron laser in the extreme ultraviolet. *Nature Photonics*, 6:699–704, 2012.

[69] C. J. Milne et al. Swissfel: The swiss x-ray free electron laser. *Applied Sciences*, 7:720, 2017.

[70] H.-S. Kang et al. Machine performance of pal-xfel. *Journal of the Korean Physical Society*, 73:235–237, 2018.

[71] I. Robinson, G. Grübel, and S. Mochrie. Focus on x-ray beams with high coherence. *New Journal of Physics*, 12:035002, Mar 2010.

[72] D. Alesini et al. The sparc/x sase-fel projects. *Laser and Particle Beams*, 22(3):341–350, 2004.

[73] Y. Hwu and G. Margaritondo. Synchrotron radiation and x-ray free-electron lasers (x-fels) explained to all users, active and potential. *Journal of Synchrotron Radiation*, 28:1014–1029, 2021.

[74] A. A. Sorokin, Y. Bican, S. Bonfigt, M. Brachmanski, M. Braune, U. F. Jastrow, A. Gottwald, H. Kaser, M. Richter, and K. Tiedtke. An x-ray gas monitor for free-electron lasers. *Journal of Synchrotron Radiation*, 2020.

[75] M. Viti, M. Kristin Czwalinna, H. Dinter, Ch. Gerth, K. Przygoda, Radosław Rybaniec, and Holger Schlarb. Recent upgrades of the bunch arrival time monitors at flash and european xfel. 2017.

[76] J. Laksman, J. Buck, L. Glaser, M. Planas, F. Dietrich, J. Liu, T. Maltezopoulos, F. Scholz, J. Seltmann, G. Hartmann, M. Ilchen, W. Freund, N. Kujala, J. Viefhaus, and J. Grünert. Commissioning of a photoelectron spectrometer for soft x-ray photon diagnostics at the european xfel. *Journal of Synchrotron Radiation*, 26:1010–1016, 2019.

[77] P. Tzallas, E. Skantzakis, L. A. A. Nikolopoulos, G. D. Tsakiris, and D. Charalambidis. Extreme-ultraviolet pump-probe studies of one femtosecond scale electron dynamics. *Nature Physics*, 7(10):781–784, 2011.

[78] B. Erk et al. Imaging charge transfer in iodomethane upon x-ray photoabsorption. *Science*, 345(6194):288–291, 2014.

[79] F. Allum et al. A localized view on molecular dissociation via electron-ion partial covariance. *Communications Chemistry*, 5(1):42, 2022.

[80] C. Bostedt et al. Linac coherent light source: The first five years. *Reviews of Modern Physics*, 88(1):015007, 2016.

[81] S. Schulz et al. Femtosecond all-optical synchronization of an x-ray free-electron laser. *Nature Communications*, 6:5938, 2015.

[82] C. Sydlo, F. Zummack, J. Müller, M. Felber, T. Lamb, T. Kozak, Ch. Gerth, and H. Schlarb. Femtosecond optical synchronization system for the european xfel. 2017.

[83] T. Lamb et al. Large-scale optical synchronization system of the european xfel with femtosecond precision. In *10th International Particle Accelerator Conference*, page THPRB018, 2019.

[84] T. J. A. Wolf et al. Probing ultrafast $\pi\pi^*$/nπ^* internal conversion in organic chromophores via k-edge resonant absorption. *Nature Communications*, 8:29, 2017.

[85] H. N. Chapman and et al. Femtosecond x-ray protein nanocrystallography. *Nature*, 470:73–77, 2011.

[86] L. Galli, S.-K. Son, M. Klinge, S. Bajt, A. Barty, R. D. Bean, C. Betzel, K. R. Beyerlein, C. Caleman, R. B. Doak, M. Duszenko, H. Fleckenstein, C. Gati, B. Hunt, R. A. Kirian, M. Liang, M. H. Nanao, K. Nass, D. Oberthür, L. Redecke, R. L. Shoeman, F. Stellato, C. H. Yoon, T. A. White, O. M. Yefanov, J. C. H. Spence, and H. N. Chapman. Electronic damage in s atoms in a native protein crystal induced by an intense x-ray free-electron laser pulse. *Structural Dynamics*, 2(4):041703, 2015.

[87] D. Ratner, J. P. Cryan, T. J. Lane, S. Li, and G. Stupakov. Pump-probe ghost imaging with sase fels. *Phys. Rev. X*, 9(1):011045, Mar 2019.

[88] L. Funke, M. Ilchen, K. Dingel, T. Mazza, T. Mullins, T. Otto, D. E. Rivas, S. Savio, S. Serkez, P. Walter, N. Wieland, L. Wülfing, S. Bari, R. Boll, M. Braune, F. Calegari, A. De Fanis, W. Decking, A. Duensing, S. Düsterer, F. Egun, A. Ehresmann, B. Erk, D. E. Ferreira de Lima, A. Galler, G. Geloni, J. Grünert, M. Guetg, P. Grychtol, A. Hans, A. Held, R. Hindriksson, T. Jahnke, J. Laksman, M. Larsson, J. Liu, J. P. Marangos, L. Marder, D. Meier, M. Meyer, N. Mirian, C. Ott, C. Passow, T. Pfeifer, P. Rupprecht, A. Schletter, P. Schmidt, F. Scholz, S. Schott, E. Schneidmiller, B. Sick, K. Tiedtke, S. Usenko, V. Wanie, M. Wurzer, M. Yurkov, V. Zhaunerchyk, and W. Helml. Capturing nonlinear electron dynamics with fully characterised attosecond x-ray pulses. *arXiv preprint arXiv:2408.03858*, 2024.

[89] H. P. Freund and P. G. O'Shea. Two-color operation in high-gain free-electron lasers. *Phys. Rev. Lett.*, 84(13):2861–2864, Mar 2000.

[90] E. Schneidmiller, I. Bermúdez Macias, M. Beye, M. Braune, M. Czwalinna, S. Düsterer, B. Faatz, R. Ivanov, U. Jastrow, M. Kuhlmann, J. Rönsch-Schulenburg, S. Schreiber, A. Sorokin, K. Tiedtke, M. Yurkov, and J. Zemella. Two-color operation of a soft x-ray fel with alternation of undulator tunes. *Applied Sciences*, 13:67, Dec 2022.

[91] A. A. Lutman, R. Coffee, Y. Ding, Z. Huang, J. Krzywinski, T. Maxwell, M. Messerschmidt, and H.-D. Nuhn. Experimental demonstration of femtosecond two-color x-ray free-electron lasers. *Phys. Rev. Lett.*, 110:134801, Mar 2013.

[92] E. Allaria, F. Bencivenga, R. Borghes, and et al. Two-colour pump–probe experiments with a twin-pulse-seed extreme ultraviolet free-electron laser. *Nature Communications*, 4:2476, 2013.

[93] L. Young, E. Kanter, B. Krässig, et al. Femtosecond electronic response of atoms to ultra-intense x-rays. *Nature*, 466:56–61, 2010.

[94] J.T. Costello S. Düsterer L. Fang J. Feldhaus H. Fukuzawa M. Hoener Y.H. Jiang P. Johnsson E.T. Kennedy M. Meyer R. Moshammer P. Radcliffe M. Richter A. Rouzée A. Rudenko A.A. Sorokin K. Tiedtke K. Ueda J. Ullrich N. Berrah, J. Bozek and M.J.J. Vrakking. Non-linear processes in the interaction of atoms and molecules with intense euv and x-ray fields from sase free electron lasers (fels). *Journal of Modern Optics*, 57(12):1015–1040, 2010.

[95] A. Rudenko, L. Inhester, K. Hanasaki, X. Li, S. J. Robatjazi, B. Erk, R. Boll, K. Toyota, Y. Hao, O. Vendrell, C. Bomme, E. Savelyev, B. Rudek, L. Foucar, S. H. Southworth, C. S. Lehmann, B. Kraessig, T. Marchenko, M. Simon, K. Ueda, K. R. Ferguson, M. Bucher, T. Gorkhover, S. Carron, R. Alonso-Mori, J. E. Koglin, J. Correa, G. J. Williams, S. Boutet, L. Young, C. Bostedt, S.-K. Son, R. Santra, and D. Rolles. Femtosecond response of polyatomic molecules to ultra-intense hard x-rays. *Nature*, 546:129–132, 2017.

[96] E.L. Saldin, E.A. Schneidmiller, and M.V. Yurkov. Scheme for attophysics experiments at a x-ray sase fel. *Optics Communications*, 212(4–6):377–390, November 2002.

[97] L. Young, K. Ueda, M. Gühr, P. H. Bucksbaum, M. Simon, S. Mukamel, N. Rohringer, K. C. Prince, C. Masciovecchio, M. Meyer, A. Rudenko, D. Rolles, C. Bostedt, M. Fuchs, D. A. Reis, R. Santra, H. Kapteyn, M. Murnane, H. Ibrahim, F. Légaré, M. Vrakking, M. Isinger, D. Kroon, M. Gisselbrecht, A. L'Huillier, H. J. Wörner, and S. R. Leone. Roadmap of ultrafast x-ray atomic and molecular physics. *Journal of Physics B: Atomic, Molecular and Optical Physics*, 51:032003, 2018.

[98] D. Rolles. Time-resolved experiments on gas-phase atoms and molecules with xuv and x-ray free-electron lasers. *Advances in Physics: X*, 8(1):2132182, 2023.

[99] M. Larsson. Nobel symposium on free electron laser research. *Applied Sciences*, 7:408, 2017.

[100] R. Püttner, G. Goldsztejn, D. Céolin, J.-P. Rueff, T. Moreno, R. Kushawaha, T. Marchenko, R. Guillemin, L. Journel, D. Lindle, M. N. Piancastelli, and M. Simon. Direct observation of double-core-hole shake-up states in photoemission. *Physical Review Letters*, 114:093001, 2015.

[101] B. Erk, R. Boll, S. Trippel, D. Anielski, L. Foucar, B. Rudek, S. W. Epp, R. N. Coffee, S. Carron, S. Schorb, K. R. Ferguson, M. Swiggers, J. D. Bozek, M. Simon, T. Marchenko, J. Küpper, I. Schlichting, J. Ullrich, C. Bostedt, D. Rolles, and A. Rudenko. Imaging charge transfer in iodomethane upon x-ray photoabsorption. *Science*, 345:288–291, 2014.

[102] V. Richardson et al. Two-photon inner-shell ionization in the extreme ultraviolet. *Physical Review Letters*, 105:013001, 2010.

[103] Y. H. Jiang, A. Rudenko, O. Herrwerth, L. Foucar, M. Kurka, K. U. Kühnel, M. Lezius, M. F. Kling, J. van Tilborg, A. Belkacem, K. Ueda, S. Düsterer, R. Treusch, C. D. Schröter, R. Moshammer, and J. Ullrich. Ultrafast extreme ultraviolet induced isomerization of acetylene cations. *Physical Review Letters*, 105:263002, 2010.

[104] H. Stapelfeldt, E. Constant, and P. B. Corkum. Wave packet structure and dynamics measured by coulomb explosion. *Physical Review Letters*, 74:3780–3783, 1995.

[105] F. Légaré, K. F. Lee, I. V. Litvinyuk, P. W. Dooley, S. S. Wesolowski, P. R. Bunker, P. Dombi, F. Krausz, A. D. Bandrauk, D. M. Villeneuve, and P. B. Corkum. Laser coulomb-explosion imaging of small molecules. *Physical Review A*, 71:013415, 2005.

[106] F. Allum, M. Burt, K. Amini, R. Boll, H. Köckert, P. K. Olshin, S. Bari, C. Bomme, F. Brausse, B. K. Cunha de Miranda, S. Düsterer, B. Erk, M. Géléoc, R. Géneaux, A. S. Gentleman, G. Goldsztejn, R. Guillemin, D. M. P. Holland, I. Ismail, P. Johnsson, L. Journel, J. Küpper, J. Lahl, J. W. L. Lee, S. Maclot, S. R. Mackenzie, B. Manschwetus, A. S. Mereshchenko, R. Mason, J. Palaudoux, M. N. Piancastelli, F. Penent, D. Rompotis, A. Rouzée, T. Ruchon, A. Rudenko, E. Savelyev, M. Simon, N. Schirmel, H. Stapelfeldt, S. Techert, O. Travnikova, S. Trippel, J. G. Underwood, C. Vallance, J. Wiese, F. Ziaee, M. Brouard, T. Marchenko, and D. Rolles. Coulomb explosion imaging of ch_3i and ch_2cli photodissociation dynamics. *The Journal of Chemical Physics*, 149:204313, 2018.

[107] R. Boll, J. M. Schäfer, B. Richard, K. Fehre, G. Kastirke, Z. Jurek, M. S. Schöffler, M. M. Abdullah, N. Anders, T. M. Baumann, S. Eckart, B. Erk, A. De Fanis, R. Dörner, S. Grundmann, P. Grychtol, A. Hartung, M. Hofmann, M. Ilchen, L. Inhester, C. Janke, R. Jin, M. Kircher, and K. Kubicek et al. X-ray multiphoton-induced coulomb explosion images complex single molecules. *Nature Physics*, 18:423–428, 2022.

[108] D. W. Lindle and O. A. Hemmers. Time-of-flight photoelectron spectroscopy of atoms and molecules. *Journal of Alloys and Compounds*, 328:27–34, 2001.

[109] P. S. Kirchmann, L. Rettig, D. Nandi, U. Lipowski, M. Wolf, and U. Bovensiepen. A time-of-flight spectrometer for angle-resolved detection of low energy electrons in two dimensions. *Applied Physics A*, 91:211–217, 2008.

[110] H. Zhang, T. Pincelli, C. Jozwiak, T. Kondo, R. Ernstorfer, T. Sato, and S. Zhou. Angle-resolved photoemission spectroscopy. *Nature Reviews Methods Primers*, 2:49, 2022.

[111] N. Hartmann, G. Hartmann, R. Heider, M. S. Wagner, M. Ilchen, J. Buck, A. Lindahl, C. Benko, J. Grünert, J. Krzywiński, J. Liu, A. A. Lutman, A. Marinelli, T. J. Maxwell, A. A. Miahnahri, S. Moeller, M. Planas, J. S. Robinson, A. K. Kazansky, N. M. Kabachnik, J. Viefhaus, T. Feurer, R. Kienberger, R. N. Coffee, and W. Helml. Attosecond time–energy structure of x-ray free-electron laser pulses. *Nature Photonics*, 12:215–220, 2018.

[112] E. Allaria et al. Control of the polarization of a vacuum-ultraviolet, high-gain, free-electron laser. *Phys. Rev. X*, 4(4):041040, 2014.

[113] J. Viefhaus, F. Scholz, S. Deinert, L. Glaser, M. Ilchen, J. Seltmann, P. Walter, and F. Siewert. The variable polarization xuv beamline p04 at petra iii: Optics, mechanics and their performance. *Nuclear Instruments and Methods in Physics Research Section A: Accelerators, Spectrometers, Detectors and Associated Equipment*, 710:151–154, 2013.

[114] Scientific Instrument Services, Inc. SIMION Simulation Software Package, Version 8.1, 2011. Accessed: [Insert access date if applicable].

[115] E. Angelico, T. Seiss, B. Adams, A. Elagin, H. Frisch, and E. Spieglan. Capacitively coupled pickup in mcp-based photodetectors using a conductive metallic anode. page 1099, 2017.

[116] J. W. Nilsson and S. A. Riedel. *Electric Circuits*. Pearson, 11th edition, 2020.

[117] VUO: Virtual Unified Office. https://vuo.elettra.trieste.it. Accessed: 2025-08-06.

[118] A. De Fanis, M. Ilchen, A. Achner, T. M. Baumann, R. Boll, J. Buck, C. Danilevsky, S. Esenov, B. Erk, P. Grychtol, G. Hartmann, J. Liu, T. Mazza, J. Montaño, V. Music, Y. Ovcharenko, N. Rennhack, D. Rivas, D. Rolles, P. Schmidt, H. Sotoudi Namin, F. Scholz, J. Viefhaus, P. Walter, P. Ziółkowski, H. Zhang, and M. Meyer. High-resolution electron time-of-flight spectrometers for angle-resolved measurements at the sqs instrument at the european xfel. *Journal of Synchrotron Radiation*, 29:755–764, 2022.

[119] M. Hentschel, R. Kienberger, C. Spielmann, G. A. Reider, N. Milosevic, T. Brabec, P. Corkum, U. Heinzmann, M. Drescher, and F. Krausz. Attosecond metrology. *Nature*, 414:509–513, 2001.

[120] P. Eckle et al. Attosecond ionization and tunneling delay time measurements in helium. *Science*, 322:1525–1529, 2008.

[121] M. Schultze, M. Fiess, N. Karpowicz, J. Gagnon, M. Korbman, M. Hofstetter, S. Neppl, A. L. Cavalieri, Y. Komninos, T. Mercouris, C. A. Nicolaides, R. Pazourek, S. Nagele, J. Feist, J. Burgdörfer, A. M. Azzeer, R. Ernstorfer, R. Kienberger, U. Kleineberg, E. Goulielmakis, F. Krausz, and V. S. Yakovlev. Delay in photoemission. *Science*, 328:1658–1662, 2010.

[122] S. Baker, J. S. Robinson, C. A. Haworth, H. Teng, R. A. Smith, C. C. Chirilă, M. Lein, J. W. G. Tisch, and J. P. Marangos. Probing proton dynamics in molecules on an attosecond time scale. *Science*, 312(5772):424–427, 2006.

[123] P. M. Kraus et al. Measurement and laser control of attosecond charge migration in ionized iodoacetylene. *Science*, 350:790–795, 2015.

[124] M. Schultze et al. Controlling dielectrics with the electric field of light. *Nature*, 493:75–78, 2014.

[125] I. P. Christov, M. M. Murnane, and H. C. Kapteyn. High-harmonic generation of attosecond pulses in the "single-cycle" regime. *Physical Review Letters*, 78:1251–1254, 1997.

[126] M. Drescher, M. Hentschel, R. Kienberger, M. Uiberacker, V. S. Yakovlev, A. Scrinzi, T. Westerwalbesloh, U. Kleineberg, U. Heinzmann, and F. Krausz. Time-resolved atomic inner-shell spectroscopy. *Nature*, 419:803–807, 2002.

[127] M. Uiberacker, T. Uphues, M. Schultze, A. J. Verhoef, V. S. Yakovlev, M. F. Kling, J. Rauschenberger, N. M. Kabachnik, H. Schröder, M. Lezius, K. L. Kompa, H. M. Müller, M. J. J. Vrakking, S. Hendel, U. Kleineberg, U. Heinzmann, M. Drescher, and F. Krausz. Attosecond real-time observation of electron tunnelling in atoms. *Nature*, 446:627–632, 2007.

[128] M. Schultze, M. Fiess, N. Karpowicz, J. Gagnon, M. Korbman, M. Hofstetter, S. Neppl, A. L. Cavalieri, Y. Komninos, T. Mercouris, C. A. Nicolaides, R. Pazourek, S. Nagele, J. Feist, J. Burgdörfer, A. M. Azzeer, R. Ernstorfer, R. Kienberger, U. Kleineberg, E. Goulielmakis, F. Krausz, and V. S. Yakovlev. Delay in photoemission. *Science*, 328:1658–1662, 2010.

[129] K. Klünder, J. M. Dahlström, M. Gisselbrecht, T. Fordell, M. Swoboda, D. Guénot, P. Johnsson, J. Caillat, J. Mauritsson, A. Maquet, R. Taïeb, and A. L'Huillier. Probing single-photon ionization on the attosecond time scale. *Physical Review Letters*, 106:143002, 2010.

[130] P. M. Kraus, B. Mignolet, D. R. Baykusheva, A. B. Rupenyan, Ľ. Horný, E. F. Penka, G. Grassi, O. I. Tolstikhin, J. Schneider, F. Jensen, L. B. Madsen, A. D. Bandrauk, F. Remacle, and H. J. Wörner. Measurement and laser control of attosecond charge migration in ionized iodoacetylene. *Science*, 350:790–795, 2015.

[131] A. Picón, C. Lehmann, and C. Bostedt et al. Hetero-site-specific x-ray pump-probe spectroscopy for femtosecond intramolecular dynamics. *Nature Communications*, 7:11652, 2016.

[132] Y. Ding, C. Behrens, P. Emma, J. Frisch, Z. Huang, H. Loos, P. Krejcik, and M.-H. Wang. Femtosecond x-ray pulse temporal characterization in free-electron lasers using a transverse deflector. *Physical Review Special Topics - Accelerators and Beams*, 14, 2011.

[133] W. Helml, A. R. Maier, and W. Schweinberger et al. Measuring the temporal structure of few-femtosecond free-electron laser x-ray pulses directly in the time domain. *Nature Photonics*, 8:950–957, 2014.

[134] J. Itatani, F. Quéré, G. L. Yudin, M. Yu. Ivanov, F. Krausz, and P. B. Corkum. Attosecond streak camera. *Physical Review Letters*, 88:173903, 2002.

[135] R. Kienberger, E. Goulielmakis, M. Uiberacker, et al. Atomic transient recorder. *Nature*, 427:817–821, 2004.

[136] S. Düsterer, P. Radcliffe, C. Bostedt, J. Bozek, A. L. Cavalieri, R. Coffee, J. T. Costello, D. Cubaynes, L. F. DiMauro, and Y. Ding. Femtosecond x-ray pulse length characterization at the linac coherent light source free-electron laser. *New Journal of Physics*, 13:093024, 2011.

[137] V. S. Yakovlev, J. Gagnon, N. Karpowicz, and F. Krausz. Attosecond streaking enables the measurement of quantum phase. *Physical Review Letters*, 105(7):073001, 2010.

[138] X. Zhao, S. Li, T. Driver, V.-H. Hoang, A.-T. Le, J. P. Cryan, A. Marinelli, and C. D. Lin. Characterization of single-shot attosecond pulses with angular streaking photoelectron spectra. *Physical Review A*, 105:013111, 2022.

[139] W. Helml, I. Grgura, P. Juranić, S. Düsterer, T. Mazza, A. R. Maier, N. Hartmann, M. Ilchen, G. Hartmann, L. Patthey, C. Callegari, J. T. Costello, M. Meyer, R. N. Coffee, A. L. Cavalieri, and R. Kienberger. Ultrashort free-electron laser x-ray pulses. *Applied Sciences*, 7:915, 2017.

[140] K. Dingel, T. Otto, L. Marder, L. Funke, A. Held, S. Savio, A. Hans, G. Hartmann, D. Meier, J. Viefhaus, B. Sick, A. Ehresmann, M. Ilchen, and W. Helml. Artificial

intelligence for online characterization of ultrashort x-ray free-electron laser pulses. *Scientific Reports*, 12:17472, 2022.

[141] J. Stöhr and H. C. Siegmann. *Magnetism: From Fundamentals to Nanoscale Dynamics*, volume 152 of *Springer Series in Solid-State Sciences*. Springer, 2006.

[142] C. Lux, M. Wollenhaupt, T. Bolze, M. Li, C. Sarpe, and T. Baumert. Circular dichroism in the photoelectron angular distributions of camphor and fenchone from multiphoton ionization with femtosecond laser pulses. *Angewandte Chemie International Edition*, 51:5001–5005, 2012.

[143] A. H. Zewail. 4d ultrafast electron diffraction, crystallography, and microscopy. *Annual Review of Physical Chemistry*, 57:65–103, 2006.

[144] H. Freund and P. van der Slot. Variable polarization control in free-electron lasers. *arXiv preprint arXiv:2012.09341*, Dec 2020.

[145] Y. Ding and Z. Huang. Statistical analysis of crossed undulator for polarization control in a self-amplified spontaneous emission free electron laser. *Phys. Rev. ST Accel. Beams*, 11(3):030702, Mar 2008.

[146] H. Deng, T. Zhang, L. Feng, C. Feng, B. Liu, X. Wang, T. Lan, G. Wang, W. Zhang, X. Liu, J. Chen, M. Zhang, G. Lin, M. Zhang, D. Wang, and Z. Zhao. Polarization switching demonstration using crossed-planar undulators in a seeded free-electron laser. *Phys. Rev. ST Accel. Beams*, 17(2):020704, Feb 2014.

[147] A. B. Temnykh. Delta undulator for cornell energy recovery linac. *Phys. Rev. ST Accel. Beams*, 11(12):120702, Dec 2008.

[148] J. Bahrdt, W. Frentrup, A. Gaupp, M. Scheer, W. Gudat, G. Ingold, and S. Sasaki. Elliptically polarizing insertion devices at bessy ii. *Nucl. Instrum. Methods Phys. Res. A*, 467:21–29, 2001.

[149] H. P. Freund and P. J. M. van der Slot. Variable polarization control in free-electron lasers. *arXiv preprint arXiv:2012.09341*, 2020.

[150] J. Bahrdt, W. Frentrup, A. Gaupp, B. Kuske, A. Meseck, and M. Scheer. Undulators for the bessy sase-fel project. *AIP Conference Proceedings*, 705(1):377–380, May 2004.

[151] M. Tischer et al. Title of the paper. In *Journal of Physics: Conference Series*, volume 2380, page 012017, 2022.

[152] M. Calvi, C. Camenzuli, E. Prat, and T. Schmidt. Transverse gradient in apple-type undulators. *Journal of Synchrotron Radiation*, 24(3):600–608, May 2017.

[153] M. Braune, G. Hartmann, M. Ilchen, A. Knie, T. Lischke, A. Reinköster, A. Meissner, S. Deinert, L. Glaser, O. Al-Dossary, A. Ehresmann, A. S. Kheifets, and J. Viefhaus. Electron angular distributions of noble gases in sequential two-photon double ionization. *Journal of Modern Optics*, 2015.

[154] A. Lutman, J. MacArthur, M. Ilchen, A. Lindahl, J. Buck, R. Coffee, G. Dakovski, L. Dammann, Y. Ding, H. Durr, L. Glaser, J. Gruenert, G. Hartmann, N. Hartmann, D. Higley, K. Hirsch, Y. Levashov, A. Marinelli, T. Maxwell, and H.-D. Nuhn. Polarization control in an x-ray free-electron laser. *Nature Photonics*, 10:468–472, 2016.

[155] S. Marotzke, D. Gupta, R. P. Wang, M. Pavelka, S. Dziarzhytski, C. von Korff Schmising, S. Jana, N. Thielemann-Kühn, T. Amrhein, M. Weinelt, I. Vaskivskyi, R. Knut, D. Engel, M. Braune, M. Ilchen, S. Savio, T. Otto, K. Tiedtke, V. Scheppe, J. Rönsch-Schulenberg, E. Schneidmiller, C. Schüßler-Langeheine, H. A. Dürr, M. Beye, G. Brenner, and N. Pontius. First experiments with ultrashort, circularly polarized soft x-ray pulses at flash2, 2025.

[156] P. Walter, A. Kamalov, A. Gatton, T. Driver, D. Bhogadi, J. C. Castagna, X. Cheng, H. Shi, R. Obaid, J. Cryan, W. Helml, M. Ilchen, and R. N. Coffee. Multi-resolution electron spectrometer array for future free-electron laser experiments. *Journal of Synchrotron Radiation*, 28(5):1364–1376, Sep 2021.

[157] L. Wuelfing. Private communication, 2024. December 2024.

[158] Kenji Tamasaku, Mitsuru Nagasono, Hiroshi Iwayama, Eiji Shigemasa, Yuichi Inubushi, Takashi Tanaka, Kensuke Tono, Tadashi Togashi, Takahiro Sato, Tetsuo Katayama, Takashi Kameshima, Takaki Hatsui, Makina Yabashi, and Tetsuya Ishikawa. Double core-hole creation by sequential attosecond photoionization. *Phys. Rev. Lett.*, 111:043001, 2013.

[159] J. Liu, Y. Li, Y. Hou, and et al. Transient responses of double core-holes generation in all-attosecond pump-probe spectroscopy. *Scientific Reports*, 14:1950, 2024.

[160] L. S. Cederbaum, F. Tarantelli, and A. Sgamellotti. On double vacancies in the core. *The Journal of Chemical Physics*, 85:6513–6523, 1986.

[161] T. Mazza, H. Zhang, M. Meyer, and DESY. Technical design report: Scientific instrument sqs. Technical Report XFEL.EU TR-2012-007, European XFEL, 2012.

[162] Hirokatsu Yumoto, Hidekazu Mimura, Tetsuya Koyama, Satoshi Matsuyama, Kensuke Tono, Yukio Inubushi, Tetsuo Togashi, Tomoya Sato, Hirokazu Kimura, Hiroshi Yokoyama, Jun Kim, Yuichi Sano, Yasuhiro Hachisu, Takashi Tanaka, Hiroshi Tanaka, Tetsuya Ishikawa, and Kazuto Yamauchi. Focusing of x-ray free-electron laser pulses with reflective optics. *Nature Photonics*, 7:43–47, 2013.

[163] H. Körber and W. Mehlhorn. Das k-auger-spektrum von neon. *Zeitschrift für Physik*, 191:217–230, 1966.

[164] M. O. Krause, F. A. Stevie, L. J. Lewis, T. A. Carlson, and W. E. Moddeman. Multiple excitation of neon by photon and electron impact. *Physics Letters A*, 31(2):81–82, 1970.

[165] G. Goldsztejn, R. Püttner, L. Journel, R. Guillemin, O. Travnikova, B. Cunha de Miranda, I. Ismail, S. Carniato, P. Selles, D. Céolin, A. F. Lago, R. Feifel, P. Lablanquie, F. Penent, M. N. Piancastelli, M. Simon, and T. Marchenko. Experimental and theoretical study of the double-core-hole hypersatellite auger spectrum of ne. *Physical Review A*, 96:012513, 2017.

[166] G. Goldsztejn, T. Marchenko, R. Püttner, L. Journel, R. Guillemin, S. Carniato, P. Selles, O. Travnikova, D. Céolin, A. F. Lago, R. Feifel, P. Lablanquie, M. N. Piancastelli, F. Penent, and M. Simon. Double-core-hole states in neon: Lifetime, post-collision interaction, and spectral assignment. *Physical Review Letters*, 117:133001, 2016.

[167] K. Tiedtke, J. Feldhaus, U. Hahn, U. Jastrow, T. Nunez, T. Tschentscher, S. V. Bobashev, A. A. Sorokin, J. B. Hastings, S. Möller, L. Cibik, A. Gottwald, A. Hoehl, U. Kroth, M. Krumrey, H. Schöppe, G. Ulm, and M. Richter. Gas detectors for x-ray lasers. *Journal of Applied Physics*, 103:094511, 2008.

[168] M. Richter, A. Gottwald, U. Kroth, A. A. Sorokin, S. V. Bobashev, L. A. Shmaenok, J. Feldhaus, Ch. Gerth, B. Steeg, K. Tiedtke, and R. Treusch. Measurement of gigawatt

radiation pulses from a vacuum and extreme ultraviolet free-electron laser. *Applied Physics Letters*, 83(14):2970–2972, 2003.

[169] B. L. Henke, E. M. Gullikson, and J. C. Davis. X-ray interactions: photoabsorption, scattering, transmission, and reflection at e = 50–30,000 ev, z = 1–92. *Atomic Data and Nuclear Data Tables*, 54(2):181–342, 1993.

[170] C. Pellegrini, A. Marinelli, and S. Reiche. The physics of x-ray free-electron lasers. *Reviews of Modern Physics*, 88:015006, 2016.

[171] N. Berrah, J. Bozek, J. T. Costello, S. Düsterer, L. Fang, J. Feldhaus, H. Fukuzawa, M. Hoener, Y. H. Jiang, P. Johnsson, E. T. Kennedy, M. Meyer, R. Moshammer, P. Radcliffe, M. Richter, A. Rouzée, A. Rudenko, A. A. Sorokin, K. Tiedtke, K. Ueda, J. Ullrich, and M. J. J. Vrakking. Non-linear processes in the interaction of atoms and molecules with intense euv and x-ray fields from sase free electron lasers (fels). *Journal of Modern Optics*, 57(12):1015–1040, 2010.

[172] L Young, Elliot Kanter, Bertold Krässig, Y Li, A March, Tim Pratt, R Santra, S Southworth, Nina Rohringer, Louis Dimauro, Gilles Doumy, Christoph Roedig, N. Berrah, Li Fang, M Hoener, P Bucksbaum, James Cryan, Shambhu Ghimire, J Glownia, and Marc Messerschmidt. Femtosecond electronic response of atoms to ultra-intense x-rays. *Nature*, 466:56–61, 07 2010.

[173] S. Flügge, W. Mehlhorn, and V. Schmidt. Angular distribution of auger electrons following photoionization. *Physical Review Letters*, 29:7–9, 1972.

[174] E. G. Berezhko, N. M. Kabachnik, and V. S. Rostovsky. Potential-barrier effects in inner-shell photoionisation and their influence on the anisotropy of x-rays and auger electrons. *Journal of Physics B: Atomic and Molecular Physics*, 11:1749, 1978.

Acknowledgement

It all began in 2017 when a newspaper headline caught my attention: the inauguration of the European XFEL, a groundbreaking X-ray FEL facility in Schenefeld, Germany. I was immediately intrigued and surprised at the feat of constructing an underground tunnel spanning approximately 3.4 km. At that moment, I couldn't help but wonder—how could someone like me ever become a part of such an endeavour? Fresh out of my Bachelor's degree, it felt like a distant dream.

Life took its course, and I moved on, completing my Master's in Photonics in 2020. Yet, despite setting aside my dream, life—and a higher power—had other plans for me. By sheer chance, I came across an opportunity to pursue a PhD in close collaboration with the European XFEL. This was during the pandemic when the world had come to a standstill, and most of us were confined to working from home. From my home in India, I took a leap of faith and applied for a position in Germany. Against all odds, I was offered the position, and that is where this incredible journey began.

As a saying from my homeland goes, "When you dream of something with all your heart, God will fulfil it—even if you forget about it." This truth resonates deeply with me, as I've experienced it firsthand. I want to express my heartfelt gratitude to the Almighty for His unwavering blessings throughout these years.

I want to express my heartfelt gratitude to Jun. Prof. Wolfram Helml, for your unwavering support and guidance throughout this journey. Despite being based in Dortmund and our rare in-person meetings, I never once felt unattended. I sincerely appreciate the freedom you provided, allowing me to learn and grow at my own pace.

I also had the immense privilege of working closely with Prof. Dr. Markus Ilchen at DESY, the European XFEL, and, later, CFEL. Your exceptional scientific career is truly inspiring, but what I admire even more are your human values. You have been the ideal supervisor one could ever hope for, always available, endlessly patient, and genuinely passionate about discussing the wonders of science. Your kindness and encouragement have left a lasting impression on me, and I am truly grateful. Thank you so much, Markus. The beautiful and respectful friendship between Wolfi and Markus has been a blessing throughout my journey. Your alignment and understanding made working with two supervisors a stress-free and harmonious experience. I am deeply grateful for your support, which created an environment that allowed me to thrive.

I would like to express my gratitude to my colleagues who collaborated with me and provided support during this trip, particularly Lars Funke, Lasse Wülfing, Niclas Wieland, and Thorsten Otto. I wish to retain fond memories of Valerija Music, as your kindness and friendliness significantly enhanced my initial experience in Hamburg. Even after you left from the group, your encouraging words and support have contributed to my personal growth. I wish to acknowledge the engineers and staff of FLASH and SQS who provided substantial support during the construction and installation of the detector. I would like to express my gratitude to Julitte Leroux and Julius Schwarz for their thoughtful feedback and invaluable writing support.

I would also like to thank my family and friends, especially my parents and sister Sandra, for your unwavering support and pride in my journey. You encouraged me to chase my dreams without any restrictions, and for that, I am eternally grateful. How you raised, educated, and trusted me to live on my own in a foreign country, where you knew no one, showed your love and faith in me. Thank you for always being by my side and for being my most significant source of strength and inspiration

Last but certainly not least, I want to express my deepest gratitude to my husband and best friend, Tony. You have stood by my side through all the ups and downs of this journey, always unwavering in your support. Your excitement and happiness for my PhD often matched or even exceeded my own, and I can only admire the selflessness and encouragement you have shown me every step of the way. Thank you for believing in me, lifting me up when I needed it most, and being my most significant source of strength.

I acknowledge the use of AI-based writing assistance tools, such as OpenAI's ChatGPT, Grammerly which were utilized for language editing, grammar correction, and stylistic improvements. All scientific content, analysis, and interpretations presented in this thesis are entirely my own.

Conference Contributions, Talks, and Publications

Collaborative Publications (Co-authored)

S. Marotzke, D. Gupta, R.-P. Wang, M. Pavelka, S. Dziarzhytski, C. von Korff Schmising, S. Jana, N. Thielemann-Kühn, T. Amrhein, M. Weinelt, I. Vaskivskyi, R. Knut, D. Engel, M. Braune, M. Ilchen, **S. Savio**, T. Otto, K. Tiedtke, V. Scheppe, J. Rönsch-Schulenberg, E. Schneidmiller, C. Schüßler-Langeheine, H. A. Dürr, M. Beye, G. Brenner, and N. Pontius: *First experiments with ultrashort, circularly polarized soft X-ray pulses at FLASH2*.

L. Funke*, M. Ilchen*, K. Dingel, T. Mazza, T. Mullins, T. Otto, D. E. Rivas, **S. Savio**, S. Serkez, P. Walter, N. Wieland, L. Wülfing, S. Bari, R. Boll, M. Braune, F. Calegari, A. De Fanis, W. Decking, A. Duensing, S. Düsterer, F. Egun, A. Ehresmann, B. Erk, D. E. F. de Lima, A. Galler, G. Geloni, M. Guetg, J. Grünert, P. Grychtol, A. Hans, A. Held, R. Hindriksson, T. Jahnke, J. Laksman, M. Larsson, J. Liu, J. P. Marangos, L. Marder, D. Meier, M. Meyer, N. Mirian, C. Ott, C. Passow, T. Pfeifer, P. Rupprecht, A. Schletter, P. Schmidt, F. Scholz, S. Schott, E. Schneidmiller, B. Sick, K. Tiedtke, S. Usenko, V. Wanie, M. Wurzer, M. Yurkov, V. Zhaunerchyk, and W. Helml: *Capturing Nonlinear Electron Dynamics with Fully Characterised Attosecond X-ray Pulses*.

Kristina Dingel*, Thorsten Otto*, Lutz Marder, Lars Funke, Arne Held, **Sara Savio**, Andreas Hans, Gregor Hartmann, David Meier, Jens Viefhaus, Bernhard Sick, Arno Ehresmann, Markus Ilchen, and Wolfram Helml: *Artificial intelligence for online characterization of ultrashort X-ray free-electron laser pulses*.

Conference Contributions and Talks

S. Savio: *Angular streaking TOF spectrometer for ultrafast pulse characterization*, DPG Spring Meeting SMuK 2023, Dresden, Germany.

S. Savio: *Ultrafast ionization dynamics study using single-shot electron spectroscopy*, DPG Spring Meeting SAMOP 2024, Freiburg, Germany.

S. Savio: *Ultrafast ionization dynamics study using single-shot electron spectroscopy*, DPG Spring Meeting SAMOP 2025, Bonn, Germany.